MAGNETIC RESONANCE IMAGING OF RETINAL PHYSIOLOGY AND ANATOMY IN MICE

A Dissertation
Presented to
The Academic Faculty

by

Eric R. Muir

In Partial Fulfillment
of the Requirements for the Degree
Doctor of Philosophy in the
Department of Biomedical Engineering

Georgia Institute of Technology

December 2010

MAGNETIC RESONANCE IMAGING OF RETINAL PHYSIOLOGY AND ANATOMY IN MICE

Approved by:

Dr. Timothy Q. Duong, Advisor
Research Imaging Institute
University of Texas Health Science Center San Antonio

Dr. Shella Keilholz
Department of Biomedical Engineering
Georgia Institute of Technology,
Emory University

Dr. Xiaoping Hu
Department of Biomedical Engineering
Georgia Institute of Technology,
Emory University

Dr. Marijn Brummer
Department of Biomedical Engineering
Georgia Institute of Technology,
Emory University

Dr. Machelle T. Pardue
Department of Ophthalmology
Emory University

Date Approved: November 2, 2010

ACKNOWLEDGEMENTS

I wish to thank my advisor Dr. Timothy Duong for supervision and guidance of my graduate studies and research; my thesis committee members Drs. Shella Keilholz, Xiaoping Hu, Marijn Brummer, and Machelle Pardue for their time and suggestions with my proposal and defense. In addition I would like to thank Xiaoping Hu for financial support through his institutional training grant, Machelle Pardue for her advisement on fellowship proposals, and Shella Keilholz for acting as a "co-advisor" at Georgia Tech after Dr. Duong moved to the UT Health Science Center.

I would also like to thank those who helped in the design and execution of experiments; Dr. Qiang Shen for much help showing how to operate the MR scanners, perform blood flow imaging, and in particular helping test and optimize arterial spin labeling and the cardiac arterial spin labeling method in mice; Dr. René Rentería for providing the diabetic Ins2^{Akita} mice and db/db mice as well as performing all visual tests on these mice; Bryan De La Garza, Guang Li, Dr. Yen Yu Ian Shih, and Will Lavery for helpful discussions and help setting up and organizing experiments; Bryan De La Garza and Dr. Machelle Pardue showing me how to acquire and analyze retinal histology; Drs. Govind Nair and Yingxia Li for their suggestions and help with the initial development of retinal imaging in mice; Drs. Swati Rane and Xiaodong Zhang for help with operation of MR scanners and image analysis; and Robbie Champion for help working with and getting mice for the early studies.

TABLE OF CONTENTS

LIST OF TABLES

LIST OF FIGURES

Page

LIST OF SYMBOLS AND ABBREVIATIONS

α	Labeling Efficiency in Arterial Spin Labeling
λ	Blood-Tissue Partition Coefficient of Water
δ	Arterial Transit Time of Blood
M_{NL}	The Non-Labeled Image in Arterial Spin Labeling
M_L	The Labeled Image in Arterial Spin Labeling
M_0	The Equilibrium Magnetization Signal
T_1	Longitudinal Relaxation Time
T_{1A}	Longitudinal Relaxation Time of Arterial Blood
T_2	Transverse Relaxation Time
ASL	Arterial Spin Labeling
BOLD	Blood Oxygenation Level Dependent
BF	Blood Flow
bSSFP	Balanced Steady-State Free Precession
CBF	Cerebral Blood Flow
chBF	Choroidal Blood Flow
cpd	Cycles Per Degree
DR	Diabetic Retinopathy
EPI	Echo Planar Imaging
ERG	Electroretinogram
FLASH	Fast Low Angle Shot
fMRI	Functional Magnetic Resonance Imaging
GCL	Ganglion Cell Layer
GRASE	Gradient and Spin Echo

INL	Inner Nuclear Layer
IPL	Inner Plexiform Layer
IS	Inner Segment
LD	Label Duration
MRI	Magnetic Resonance Imaging
OCT	Optical Coherence Tomography
ONL	Outer Nuclear Layer
OPL	Outer Plexiform Layer
OS	Outer Segment
$PaCO_2$	Partial Pressure of Arterial Carbon Dioxide
PaO_2	Partial Pressure of Arterial Oxygen
rBF	Retinal Blood Flow
RF	Radiofrequency
SD	Standard Deviation
SEM	Standard Error of the Mean
SNR	Signal to Noise Ratio
SPM	Statistical Parametric Mapping
STZ	Streptozotocin
TE	Echo Time
TR	Repetition Time
w	Post Label Delay

SUMMARY

MRI can provide anatomical, functional, and physiological images at relatively high spatial resolution, is non-invasive and does not have depth limitation. However, the application of MRI to study the retina is difficult due to the very small size of the retina. This thesis details the development of MRI methods to image blood flow (BF), anatomy, and function of the retina and choroid, and their application to two diseases of the retina: diabetic retinopathy and retinal degeneration.

A unique continuous arterial spin labeling technique was developed to image BF in mice and tested by imaging cerebral BF. This method was then applied to image layer-specific BF of the retina and choroid in mice and to acquire BF functional MRI of the retina and choroid in response to hypoxic challenge. Additionally blood oxygen level dependent functional MRI of the mouse retina and choroid in response to hypoxic challenge was obtained using a balanced steady state free precession sequence which provides fast acquisition, has high signal to noise ratio, and does not have geometric distortion or signal dropout artifacts.

In a mouse model of diabetic retinopathy, MRI detected reduced retinal BF in diabetic animals. Visual function in the diabetic mice, as determined by psychophysical tests, was also reduced. Finally, in a mouse model of retinal degeneration, BF and anatomical MRI detected reductions of retinal BF and the thickness of the retina. The studies detailed in this thesis demonstrate the feasibility of layer-specific MRI to study BF, anatomy, and function, in the mouse retina. Further, these methods were shown to provide a novel means of studying animal models of retinal disease *in vivo*.

CHAPTER 1

INTRODUCTION

MRI can provide anatomical, functional, and physiological images at relatively high spatial resolution and is non-invasive, does not have depth limitation, and provides excellent soft tissue contrast. MRI is widely used to study anatomy and physiology throughout the body due to these favorable properties. However, the application of MRI to study the retina is still difficult due to the very small size of the retina. The retina, which can be seen through the pupil, has thus traditionally been studied using optical techniques, some of which are limited to probing the retinal surface.

In many diseases affecting various organs, the blood flow (BF) supply is known to be affected, or even an underlying cause of disease. Changes in the vasculatures and BF which nourish the retina are known to be important factors in retinal diseases such as diabetic retinopathy (1-4), glaucoma (5), and retinal ischemia (6). There is also some evidence of vascular damage in retinal degeneration (7-10).

MRI has been used to image changes in cerebral BF in many different neurological diseases (11), such as stroke (12,13), brain tumor (14), Alzheimer's disease (15,16), and epilepsy (17). MRI can image BF using arterial spin labeling (ASL) as well as functional changes and anatomy in the same setting. The application of MRI to study BF of the retina and alterations of BF in disease is quite challenging due to the high resolution that is necessary.

This thesis describes the development of MRI methods to non-invasively image blood flow and anatomy of the retina and choroid in mice at high resolution and with layer-specificity. These methods are applied to mouse models of two diseases, diabetic retinopathy and retinal degeneration. The rest of this chapter provides background information on the retina, MRI techniques, and imaging the retina.

Chapter 2 describes the development of an MRI method to image quantitative BF in mice using continuous ASL, which provides excellent BF contrast. Continuous ASL using separate labeling and imaging coils in mice is difficult due to their small size which can result in saturation from the labeling coil, causing significant BF measurement errors. Two-coil continuous ASL was implemented in mice using a labeling coil placed at the heart, rather than the neck. This approach provides all the benefits of two-coil continuous ASL including, high labeling efficiency, ability for multi-slice acquisitions, and lack of magnetization transfer artifacts. This method was used to image basal cerebral BF (CBF) and CBF changes due to hypercapnia.

Chapter 3 describes the application of the cardiac ASL technique, described in Chapter 2, to image layer-specific BF of the retina and choroid in mice. High-resolution cardiac ASL was utilized to image quantitative, layer-specific retinal BF (rBF) and choroidal BF (chBF) in the mouse retina at $42 \times 42 \times 400\ \mu m^3$ resolution. This method was then applied to acquire layer-specific BF functional MRI (fMRI) of the retina and choroid using hypoxic challenge as a stimulation.

Chapter 4 describes the application of a balanced steady state free precession (bSSFP) sequence to perform fMRI of the mouse retina and choroid. Most functional MRI studies use echo planar imaging sequences (EPI), but these sequences are prone to susceptibility artifacts due to magnetic inhomogeneity. EPI of the retina is particularly prone to these artifacts because the region around the eye is very inhomogeneous. bSSFP sequences provide fast acquisition, have high SNR, and do not have geometric distortion or signal dropout artifacts associated with EPI. bSSFP imaging of the mouse retina and choroid was used to detect changes in blood oxygenation due to hypoxic challenge.

Chapter 5 describes the application of high-resolution ASL MRI to image quantitative, layer-specific BF of the retina and choroid in the Ins2^{Akita} mouse model of diabetic retinopathy. Further, the vision of the diabetic mice was studied using psychophysical tests to determine changes of visual acuity and contrast sensitivity in diabetic mice.

Chapter 6 describes the application of high-resolution MRI to anatomy and BF in the rd10 mouse model of retinal degeneration. MRI was utilized to image quantitative, layer-specific retinal and choroidal blood flow at different stages of degeneration. Anatomical MRI was also obtained to monitor changes in retinal and choroidal thickness over time.

Chapter 7 summarizes the studies described in this thesis.

1.1 Anatomy and Physiology of the Retina and Choroid

1.1.1 Retinal Anatomy and Function

The retina is a part of the central nervous system located at the back of the eye which converts light into nerve signals to produce vision (18). The retina consists of multiple structured anatomical layers (Figure 1.1). Starting from the outer layers of the retina and going towards the vitreous, anatomical layers of the retina are the retinal pigment epithelium, the inner and outer segments (IS and OS), outer nuclear layer (ONL), outer plexiform layer (OPL), inner nuclear layer (INL), inner plexiform layer (IPL), ganglion cell layer (GCL), and the nerve fiber layer (18). Behind the retinal pigment epithelium are the choroid and sclera. The retina and choroid together are only about 250 μm thick in rodents (9,19).

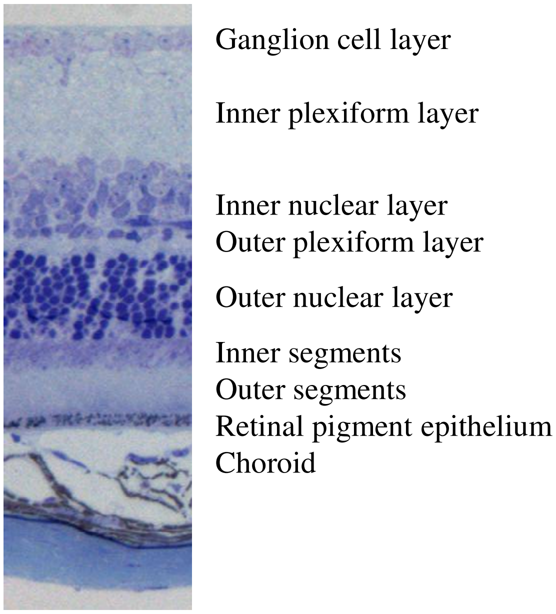

Figure 1.1: Histological section of a mouse retina and its anatomical layers. Histology was obtained from a normal mouse with toluidine blue staining.

The inner and outer segments consist of the rods and cones of the photoreceptors. The rods and cones are responsible for converting light to biochemical signals, through opsin proteins bound with retinal (20). Absorption of photons by retinal induces an isomerization, making the molecule able to activate transducin. The activated transducin then activates phosphodiesterase, which converts cyclic guanosine monophosphate (GMP) to GMP. Reduced cyclic GMP causes the closure of cyclic GMP gated cationic channels and hyperpolarization of the photoreceptor cell (20).

The outer nuclear layer is made up of the cell bodies of the photoreceptors. The outer plexiform layer consists of synapses between the photoreceptors and other types of neurons in the inner nuclear layer. The inner nuclear layer consists of the cell bodies of horizontal, bipolar, and amacrine cells, neurons of the retina. The inner plexiform layer is another synaptic layer, with connections between neurons of the inner nuclear layer and ganglion cells. The ganglion cell layer and nerve fiber layer primarily consist of the ganglion cells and their axons, neurons which transmit information from the retina to the optic nerve and brain (18). The retinal pigment epithelium is a thin layer of epithelial cells, which forms a barrier separating the neural retina from the choroid (18,21). The retinal pigment epithelium maintains the environment of the outer retina, supplying necessary molecules through active transport and removing waste products (18,21).

1.1.2 Retinal and Choroidal Blood Flow

The retina is nourished by two separate blood supplies, the retinal and choroidal circulations, located on either side of the retina (22,23). The retinal vessels are mainly localized on the inner surface of the retina, with arterioles and capillaries projected into the ganglion cell layer, inner plexiform layer, and inner nuclear layer. The choroidal vessels are located external to the neural retina in the choroid. The layers consisting of the photoreceptor cells (the outer nuclear layer and the inner and outer segments) and the outer plexiform layer are avascular, located in between the retinal and choroidal vascular layers (22). The retinal vessels mainly server the inner retina, while the choroidal vessels server the outer retina. The outer retina, which is avascular, receives oxygen mainly from the choroid by diffusion. Most of the oxygen of the inner retina comes from the retinal vasculature which has capillaries within the inner retina (22,24).

The two vasculatures are quite different from each other. The choroid has very high vascular density, with among the highest BF and blood volume of any tissue. Choroidal blood flow (chBF) is many times greater than retinal blood flow (rBF)

(22,23,25,26). The reported ranges of chBF are around 7-19 ml/g/min (7,22), and rBF is reported to be around 0.2-0.9 ml/g/min (27,28). For comparison, rBF is generally similar to cerebral blood flow (CBF), while chBF is substantially higher (22). The high chBF is usually believed to be necessary to maintain a large oxygen gradient between the choroid and outer retina to drive oxygen diffusion into the outer retina (22,29).

There is evidence that the two circulations may have different susceptibility to diseases and their deterioration may progress differently. For example, in a cat model of retinal degeneration, rBF is compromised whereas chBF is not significantly affected compared (7). In diabetic retinopathy, the choroidal and retinal blood vessels are anatomically abnormal and blood velocity decreases in retinal vessels in early phase in the streptozotocin-induced diabetic rat retina (1,30).

1.1.3 Control of Retinal and Choroidal Blood Flow

There are substantial differences in regulation of retinal and choroidal BF. The two vasculatures also respond differently to various physiological and blood flow regulating factors (22). The rBF is regulated locally by the metabolic needs of the tissue it perfuses. The chBF, which is separated from the outer retina - the tissue that it nourishes, is not regulated by the local metabolic of the outer retina. Increased oxygen causes decreased rBF (31,32), while having no effect on chBF (33,34). Hypoxia has also been found to cause rBF to increase (35). Hypercapnia causes both rBF and chBF to increase (32,33,36), and hypocapnia results in decreased retinal and choroidal BF (37).

The retinal and choroidal vessels may also be regulated differently to changes in their perfusion pressure (22). The retinal vasculature is consistently reported to autoregulate in response to changes in perfusion pressure, either dilating or constricting, to maintain BF (38,39). The choroid, however, is reported to lack autoregulation (36,40), but it is also reported to be autoregulated (41,42).

The choroid receives sympathetic and parasympathetic innervation, while the retinal vessels lack any direct nervous control (22,43). Stimulation of sympathetic nerves going to the eye causes vasoconstriction of choroidal vessels and reduces chBF, but does not affect rBF (22,43,44). Stimulation of parasympathetic nerves going to the eye increases chBF while not affecting rBF (22,45).

1.2 Magnetic Resonance Imaging

MRI uses a strong magnetic field to align the nuclear magnetization of nuclei (usually hydrogen protons), and then radiofrequency (RF) pulses are used to excite the nuclei (46). The excited nuclei produce an electromagnetic signal as they relax back to their equilibrium state, which is detected as the MR signal. Magnetic gradients are used to provide spatial information and to create an image. The MR signal is dependent on various tissue specific parameters, including proton density, longitudinal relaxation time (T_1), and transverse relaxation time (T_2). These MRI parameters vary depending on properties of the local tissue environment including water content, cellular structure, macromolecule content, and ion concentrations (46). The MR signal can be modified to produce images weighted by different parameters, such as blood oxygenation, blood flow, or blood volume.

1.2.1 Blood Oxygenation Level Dependent Functional MRI

Functional MRI can non-invasively image functional hemodynamic responses, based on changes in blood oxygenation. This technique is referred to as blood oxygenation level dependent (BOLD) fMRI (47). BOLD fMRI detects differences in MR signal intensity that arise from changes in oxygen saturation of hemoglobin. Deoxyhemoglobin is paramagnetic and thus introduces intravoxel magnetic field inhomogeneity, while oxyhemoglobin is diamagnetic. The magnetic susceptibility difference between the paramagnetic deoxyhemoglobin and the surrounding tissues will alter the MR signal, so susceptibility-sensitized MRI images are able to show changes in regional deoxyhemoglobin content (48). A local reduction in deoxyhemoglobin concentration will increase the BOLD signal, while an increase in deoxyhemoglobin will decrease the BOLD signal (48).

In the brain, when a specific region is activated due to stimulations, local blood flow increases to compensate for the increased metabolic activity and oxygen consumption in the region. Such blood flow increases will provide a boost in oxygen delivery in excess of the increased oxygen consumption associated with increased neural activities (49). Local oxygen saturation therefore increases and deoxyhemoglobin concentration decreases, causing an increase in the MR signal intensity.

BOLD fMRI techniques have been used to study neurovascular coupling in the brain using physiologic challenges, such as hyperoxia, hypercapnia, and breath hold (50-53). These stimuli modulate cerebral BF and oxygenation with little if any changes in neural activity and oxygen consumption. This provides valuable information regarding the integrity of neurovascular coupling, independent of changes in neural activity.

1.2.2 Blood Flow MRI and Arterial Spin Labeling

Two major MRI techniques have been developed to quantitatively image BF, dynamic susceptibility contrast in which an intravascular contrast agent is injected or arterial spin labeling (ASL) in which water in blood is magnetically labeled to provide endogenous contrast. The half-life of exogenous contrast agents in blood is relatively long. This prevents the acquisition of multiple repetitions for time series analysis or averages to improve the signal to noise ratio of the blood flow data. The half-life of labeled blood in ASL, however, is on the order of the T_1 of blood, which is about 2 s at 7 Tesla (54). Therefore ASL can be repeated rapidly, every few seconds, allowing for averaging and time series acquisition.

Two commonly used techniques for performing ASL are the continuous and pulsed methods (55-57). Continuous ASL uses a long RF pulse combined with magnetic gradients applied in the direction of flow to adiabatically invert moving spins as they flow past the labeling plane (58). In pulsed ASL, a short 180^o RF pulse is used to quickly invert blood within a large slab (59,60). Compared to pulsed ASL, continuous ASL generally provides better BF signal and contrast due to higher label efficiency (56,61). Continuous ASL however deposits more power into the subject and can be difficult to implement, limiting its use for human MRI.

Continuous arterial spin labeling can be performed using the same coil or separate coils for labeling and imaging. The latter approach yields improved BF signal-to-noise ratio (SNR) with minimal magnetization-transfer if the imaging coil is decoupled while the labeling coil is transmitting. The two coil approach also easily allows multi-slice imaging which is otherwise difficult due to magnetization transfer in the single coil approach (56,61).

Quantitative BF, in units of (ml of blood) / (g of tissue) / min, has been calculated from ASL MRI with a variety of strategies (62). Initially BF was calculated using modified Bloch equations to include the effect of inflowing spins in blood which have been inverted by ASL with a single compartment model (58). This model assumes that water is freely diffusible tracer between blood and tissue. Blood flow using this model can be calculated as (58,63)

$$BF = \frac{\lambda}{T_1} \cdot \frac{M_{NL} - M_L}{M_L + (2\alpha - 1) \cdot M_{NL}} \qquad \text{(Eq. 1.1)}$$

where BF is quantitative blood flow values, M_{NL} is the signal intensity of the non-labeled images and M_L is signal intensity of the labeled images. λ is the tissue-blood partition coefficient of water, which is the ratio of water concentration of tissue to blood and is often reported as (64)

$$\frac{ml\ water}{g\ tissue} \Bigg/ \frac{ml\ water}{ml\ blood} \qquad \text{(Eq. 1.2)}$$

λ has been measured by weighing wet and dry tissues to determine water content (64). Although λ varies from tissue to tissue, a whole brain average value of 0.9 is often used for quantification of CBF (64). Water content of various other tissues has been reported (65), including that of the neural retina (66). T_1 is the longitudinal relaxation time of the tissue which is about 1.7-2.0 s in the brain and the retina at 7 Tesla (67,68). α is the labeling efficiency which can be measured experimentally using images acquired without labeling of blood and with optimally labeled blood (69,70). The optimal labeling power occurs when the arterial signals reach plateau with increasing power. α can then be calculated as

$$\alpha = \frac{M_{NL} - M_L}{2 \cdot M_{NL}} \qquad \text{(Eq. 1.3)}$$

where the signal intensities M_{NL} and M_L are measured from a large artery in the image. Since the blood is being inverted, the sign of M_L should be made negative in the calculation to account for the fact that the value comes from the magnitude image. For perfect inversion, M_{NL} and M_L would be equal, giving a maximum value of $\alpha = 1$. For saturation of the blood signal, as opposed to inversion, M_L would equal 0 and α would be 0.5.

Other parameters that can affect quantification of BF include the transit time (δ), post labeling delay (w), and labeling duration (LD) (57). The transit time is the time needed for labeled blood to flow from the labeling site to the imaging site, and post labeling delay is a delay that is commonly inserted between the end of the labeling pulse and acquisition of images to allow labeled blood to flow out of large arteries and arterioles (57,71). These both introduce time during which labeled blood will undergo T_1 relaxation and can be compensated for in the BF calculation (62). For continuous ASL, the labeling duration should ideally be infinitely long, and the use of finite labeling pulses will cause BF to be underestimated. Finite labeling durations can be compensated for in the BF calculation as well (62,72). Including these other parameters, the BF can be calculated as (62,70,73)

$$BF = \frac{\lambda}{T_1} \cdot \frac{M_{NL} - M_L}{e^{-\delta / T_{1A}} \cdot e^{-(w-\delta)/T_1} \cdot (1 - e^{-LD/T_1}) \cdot 2\alpha \cdot M_{NL}} \qquad \text{(Eq. 1.4)}$$

where T_{1A} is the T_1 of arterial blood while T_1 is the T_1 of tissue and assuming $w > \delta$.

BF quantification with ASL is prone to other errors including incomplete water exchange and venous outflow effects (55,57,73,74). It has been shown in the brain at least, that water is not entirely a freely diffusible tracer, which introduces some error into the calculation using the single compartment model (73,75,76). The water-exchange effect on BF quantification is complex, depending on the difference between blood T_1

and tissue T_1, blood flow rate, the extent of water exchange, magnetic field strength, BF measurement techniques, and BF calculation models (73,74).

BF can be dynamically measured using ASL to determine BF changes in response to stimulations. Blood flow fMRI is more sensitive to BF in smaller vessels which better reflect local tissue perfusion and avoid contamination from large draining veins, which are prominent in typical BOLD fMRI (57). Moreover, BF fMRI is easier to interpret because it measures a single physiological parameter, in contrast to BOLD fMRI which is affected by multiple physiological parameters, such as blood flow, blood volume, and blood oxygenation. However, BF fMRI has lower temporal resolution and much lower SNR compared to BOLD fMRI (57,77).

1.3 Methods of Studying the Retina and Choroid

In humans, the retina and choroid have been studied almost exclusively using optical methods. Optical methods are mostly non-invasive and can provide anatomical, functional, or physiologic information. Most optical techniques have limited depth resolution, and the choroid is often not studied being too deep to be probed by many methods. In animals, methods that are highly invasive or terminal have been used to study anatomical and physiological parameters that could not be measured through optical techniques.

1.3.1 Optical Techniques

Optical coherence tomography (OCT) has relatively deep tissue penetration and provides depth resolution, unlike most other optical methods (78). OCT is mostly used for anatomical imaging, providing very high-resolution images (resolutions of a few μm) with many distinct retinal layers images (79). Recently OCT has been adapted to study blood velocity in vessels as small as capillaries (80,81). There are still some difficulties with blood velocity measurements such that only flow in the axial direction is detected (80).

Angiography using intravascular dyes is clinically used to assess hemodynamics of the retina and choroid (22,82). Measurement of various hemodynamic parameters can be made. The mean transit time of a vessel is found from the concentration-time curves of the dye bolus. The arteriovenous passage time can be measured as the time for the dye to pass from the arteries to veins (22,82). Additionally, the velocity of the dye moving through a vessel can be measured from the distance traveled by the dye in successive frames (82). Fluorescein angiography is commonly used to study the retinal vasculature (83). Indocyanine green, another dye, fluoresces at a wavelength that passes through the retinal pigment epithelium, so it is used for angiography of the choroidal vessels (84). Angiographic techniques are slightly invasive since they require intravascular injections of dye. Although quantitative measurements can be made, they are limited to large vessels such as arteries and arterioles. They also lack depth resolution, so distinguishing retinal and choroidal vessels when using indocyanine green can be somewhat difficult.

Laser Doppler velocimetry is used to measure the quantitative velocity of blood cells flowing through large vessels (82,85,86). Laser Doppler velocimetry detects the Doppler frequency shift of the light due to moving erythrocytes in the blood. A fundus image taken with some other device can be used to measure vessel diameter and estimate cross-sectional area of the vessel, and used in combination with laser Doppler velocimetry, the blood flow through the vessel can be calculated (82,86). Laser Doppler velocimetry can only be performed on large vessels on the inner surface of the retina and only provides measurements at discrete points.

Laser Doppler flowmetry is similar to Laser Doppler velocimetry, but the laser is directed at tissue, detecting moving erythrocytes in microvasculature perfusing the tissue (34,87). Laser Doppler flowmetry provides non-quantitative measures of tissue perfusion (87). Thus, laser Doppler flowmetry is often used to detect functional changes in BF due to stimulations. Due to the lack of depth resolution, the laser Doppler flowmetry signal will be some unknown combination of signals from the retina and choroid (87). Laser Doppler flowmetry is often performed at the fovea, which lack retinal vessels to report chBF (33,34).

Laser speckle imaging determines relative BF in a tissue based off fluctuations in interference patterns of scattered light due to moving red blood cells (88,89). Laser speckle imaging can provide relative BF images of the retinal surface, but is mostly used to study functional BF changes during stimulations due to difficulty in quantification (89). Laser speckle imaging lacks depth resolution, making separation of retinal and choroidal signals difficult.

1.3.2 Non-optical Techniques

The microsphere technique using intravascular injection of radioactively or fluorescently labeled microspheres has been used to study quantitative BF of the retina and choroid in animals (40,90). Intravascularly injected microspheres become embedded in capillary beds in proportion to the rate of BF to the tissue. Blood flow can be determined by measuring the amount of radiation, fluorescence, or counting the number of spheres in a tissue (40). Microspheres can only be used in terminal experiments, since the organ of interest must be removed for analysis. Also, functional studies are difficult using microspheres since multiple doses of differently labeled spheres must be injected before and after stimulation, but repeated doses of microspheres can change BF and animal physiology (35,37).

Blood flow and tissue oxygenation having been studied using electrodes inserted through the eye and into the retina and choroid. BF can be determined by measuring the clearance of hydrogen from the tissue (91,92). Oxygen tension in tissues can also be measured using microelectrodes (93,94). Electrode based measurements only measure local information at the location of the electrode. The exact location of the electrode tip cannot be known for certain. Local inhomogeneities of the tissue around the electrode can significantly affect the measurement. For example, the electrode being nearby an artery or arteriole will give much different readings than if there were nothing but tissue nearby (95).

1.4 Previous MRI Studies of the Retina and Choroid

Optical techniques require an unobstructed light path, so eye diseases such as vitreal hemorrhage and cataract may preclude the use of optical techniques. Optical techniques used to study blood flow and physiology are generally qualitative or the signals are measured from individual blood vessels which may not accurately reflect local tissue perfusion. Additionally, most optical techniques, aside from OCT, lack depth resolution, so distinguishing signals from the retina or choroid is difficult.

In recent years, high-resolution laminar-specific MRI of the retina and choroid has been used in animals. Methods to image anatomy, BF, and BOLD functional changes have been reported. MRI methods which can non-invasively image physiology and function of the retina and choroid without depth resolution could help to better understand how these two vascular layers are regulated in health and disease, improving understanding of pathophysiology *in vivo*.

1.4.1 Anatomical MRI of the Retina

Anatomical MRI has been used to image multiple layers of the retina and choroid. Using gradient echo and spin echo sequences, 3 retinal layers, including the choroid have been detected in cats (96) and rats (9), and 4 retinal layers have been detected in mice (19). Intraocular injection of the MRI contrast agent manganese chloride has been used to enhance anatomical layer contrast, providing images with 7 retinal layers, including the choroid (97). Finally, measurement of MRI parameters affecting anatomical image contrast, including T1, T2, and the apparent diffusion coefficient of water have been measured in cats (96), rats (68), and mice (19).

1.4.2 Functional MRI of the Retina

BOLD fMRI of the retina has been performed to visual and physiological stimulations. In both cats and rats, a positive BOLD signal has been detected in the retina in response to visual stimuli (98,99). These studies were performed at relatively low resolution, so the source of the response, the retinal or choroidal vasculature, could not be localized. BOLD fMRI in response to hypercapnia and hyperoxia has been performed in rats (9). Different responses could be detected on the inner and outer edges of the retina, likely corresponding to the retinal and choroidal vasculatures, respectively. However, the resolution was relatively low, making separation of the layers not entirely clear. Additionally, the BOLD changes in response to hypercapnia and hyperoxia were found to be attenuated in a rat model of retinal degeneration (9).

1.4.3 Blood Flow MRI of the Retina

Blood flow MRI and fMRI of the retina has been reported in rats using ASL (8,100). In these studies, the resolution was too low to distinguish retinal and choroidal BF. There was only a single BF layer of the combined retina and choroid. BF fMRI in response to hypercapnia and hyperoxia was also demonstrated in rats. BF of the combined retina/choroid was found to increase in response to hypercapnia and decrease in response to hyperoxia (100). BF MRI of a rat model of retinal degeneration found basal BF of the combined retina/choroid to be decreased (8). BF fMRI in response to hypercapnia and hyperoxia was also performed in the rat model of retinal degeneration. The magnitude change in quantitative BF was attenuated in the disease rats, but the percent BF change was not altered (8). BF of the combined retina/choroid has also been reported using MRI in humans, but at much lower resolution (101,102). The BF values reported in human so far are much lower than chBF reported in animals with invasive techniques. A likely reason for this is the low resolution ASL MRI used in humans results in substantial partial volume of the choroid and tissues with low BF, reducing the measured BF value.

CHAPTER 2

CONTINUOUS ARTERIAL SPIN LABELING IN MICE APPLIED TO CEREBRAL BLOOD FLOW

While continuous ASL using a separate neck labeling coil has been employed in rats (13,103), humans (69), and monkeys (70,104), its extension to mice had not yet been reported. Mice are widely used in biomedical research, and there exists many disease models available in mice, with new transgenic and knockout mouse models frequently created. As such, a method to accurately measure blood flow (BF) in mice *in vivo* with high resolution and good signal to noise ratio (SNR) could provide unique information about the underlying physiology or causes of numerous diseases, such as stroke (13), Alzheimer's disease (15,16,105), or diabetic retinopathy (1,30,106).

A possible reason for the absence of continuous ASL in mice is due to their small size which results in proximity of the labeling coil and imaging brain coil, separated by only about 1 cm from center to center. This causes significant saturation of the brain signal by the neck coil, causing significant CBF measurement errors. This occurs even when the coils are actively decoupled, coil sizes are minimized, and inter-coil distance is maximized. BF imaging in mice using other MRI techniques is sparse and only a few CBF studies using the single-coil ASL method (107-111) and the dynamic susceptibility contrast method (112,113) have been reported. These previous studies seem to suffer from limitations of these techniques, such as single slice acquisitions, low labeling efficiency, or low BF contrast and SNR.

To overcome the above limitations, two-coil continuous ASL was implemented in mice using a labeling coil placed at the heart, rather than the neck. The separation of the labeling coil and imaging slices is large enough (about 2 cm for the brain) to avoid saturation of brain tissue by the labeling coil. This approach provides all the benefits of two-coil continuous ASL, including high labeling efficiency, ability for multi-slice acquisitions, and lack of magnetization transfer artifacts. Cardiac ASL was used to image basal CBF and CBF changes due to hypercapnia.

2.1 Methods

Animal preparations: Mice (C57BL/6, 6-10 weeks, n = 5) were imaged under 1.2% isoflurane and spontaneous breathing conditions. Under baseline, 30% O_2 with balance nitrogen was supplied to the mice. Animals were placed in an animal holder with ear and tooth bars. Respiration rate (80-130 breaths/min) and rectal temperature (37 ± 0.5^{o} C) were monitored and maintained within normal physiological ranges.

MRI methods: MRI studies were performed on a 7 Tesla, 30 cm magnet and a 150 G/cm BGA6S gradient insert (Bruker, Billerica, Massachusetts). A custom-made, circular surface coil (diameter = 1.1 cm) with active decoupling was placed on top of the head. A circular labeling coil (diameter = 0.8 cm), built into the holder, was placed at the heart position for cardiac ASL. The two coils were positioned parallel to each other and were separated by about 2 cm from center to center.

BF MRI was acquired using ASL with a gradient-echo EPI sequence. Paired images, one with and one without labeling, were acquired in an interleaved fashion. The cardiac ASL employed a 2.1 s square radiofrequency pulse to the labeling coil in the presence of 2.0 G/cm gradient and a post labeling delay of 1.4 ms. The sign of the frequency offset was switched for non-labeled images. Other MRI parameters were: field of view = 12.8x12.8 mm^2, matrix = 64x64 (single-shot EPI) or 128x128 (four-shot EPI), slice thickness = 1 mm, 9 slices, TR = 2.6 s per segment, and TE = 10 ms.

Labeling efficiency was measured at the distal internal carotid arteries at the base of the frontal lobe using a fast low angle shot (FLASH) acquisition. Sequence parameter were: field of view = 11x8 mm^2 or 11x11 mm^2, matrix = 128x128, slice thickness = 1 mm, TE = 4.57 ms, 1 slice, labeling duration = 300 ms, 5-7 variable powers for the labeling pulse, and TR = 313 ms. The short TR was used to saturate static brain signal for better delineation of the blood vessels while steady-state labeling could still be achieved in large arteries.

Hypercapnic challenge: Hypercapnic challenge used premixed gas of 5% CO_2 with 30% O_2 and balance N_2. The baseline consisted of 30% O_2 with balance N_2. Each trial consisted of a 6 or 7 min scan, with baseline conditions during the first half of the trial and hypercapnia during the second half. A 10 min break was given between trials for the animals to return to normal physiologic conditions. Two to four repeated measurements for each gas condition were typically made.

Data analysis: Image analysis was done using Matlab (MathWorks Inc, Natick, MA) and STIMULATE software (University of Minnesota). Basal CBF data were derived from measurements under baseline conditions. Blood flow images, in units of ml/g/min, were calculated pixel-by-pixel using Eq. 1.1. The water tissue-blood partition coefficient λ was taken to be 0.9 (64). Whole brain average T_1 at 7 T was taken to be 1.7 s (67). A value of 0.73 was used for the labeling efficiency α, as measured for cardiac

ASL. The labeling efficiency was calculated from Eq. 1.3 using the arrayed labeling power data.

To analyze BF fMRI changes to hypercapnia, the CBF time-course was calculated using pair wise subtraction of consecutive non-labeled and labeled images. The percent change in CBF between baseline and hypercapnia was then calculated.

2.2 Results

2.2.1 Basal Cerebral Blood Flow

The schematic of the cardiac ASL setup is shown in Figure 2.1. Quantitative CBF analysis employed regions of interest, including the whole brain, frontal cortex, sensory-motor cortex, corpus callosum, hippocampus, caudate putamen, thalamus, inferior colliculus, superior colliculus, pons, and cerebellum. Labeling efficiency was measured to be 0.73 ± 0.06 (n = 5), measured at the distal internal carotid arteries at the base of frontal lobe.

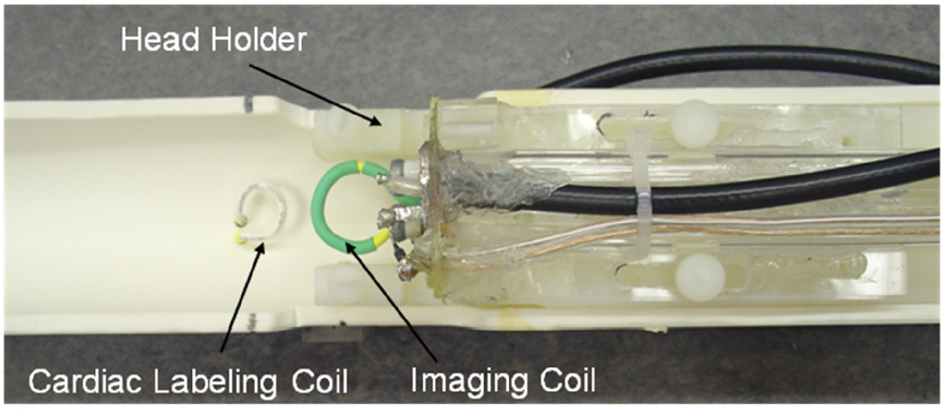

Figure 2.1: Set-up for cardiac ASL to image CBF in mice, showing the imaging and labeling coils, as well as the animal holder. The two coils are separated by about 2 cm, center-to-center. Adapted from Muir et al., Magn Reson Med 2008, (114).

Quantitative CBF images at 200x200 μm^2 and 100x100 μm^2, shown in Figure 2.2, have heterogeneous blood flow contrast as expected. CBF is lower in the corpus callosum (white matter) compared to gray matter. CBF in the cerebellum and brain stem could be imaged, in contrast to two-coil ASL CBF in rats where the cerebellum and brain stem are often not reported due to saturation artifacts by the neck labeling coil. The whole-brain CBF was 1.07 ± 0.08 ml/g/min (mean ± SD, n = 5). Regional CBF values at 100x100 μm^2, obtained from different regions of interest (shown in Figure 2 C) are summarized in Table 2.1.

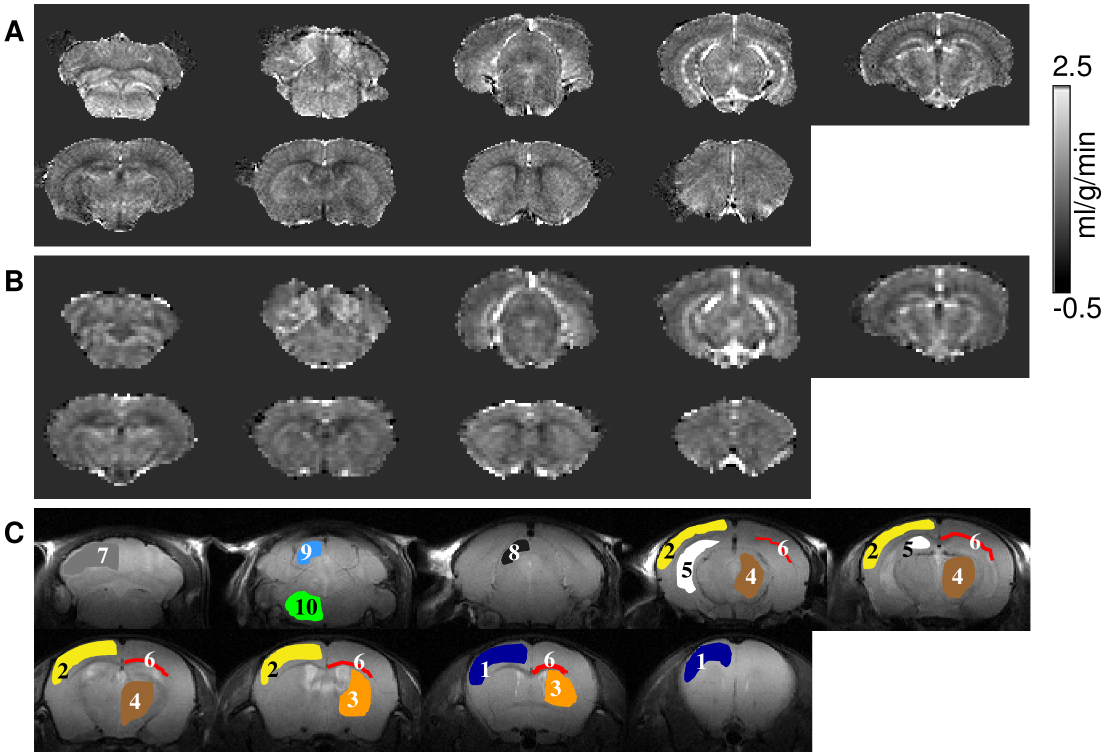

Figure 2.2: Quantitative CBF maps (in ml/g/min) from a normal mouse at (A) 100x100x1000 μm^3 and (B) 200x200x1000 μm^3. Slices go from posterior to anterior. (C) The regions of interest used for regional CBF analysis overlaid on T_2 weighted anatomical images. 1. frontal cortex, 2. sensory-motor cortex, 3. caudate putamen, 4. thalamus, 5. hippocampus, 6. corpus callosum, 7. cerebellum, 8. superior colliculus, 9. inferior colliculus, 10. pons. Adapted from Muir et al., Magn Reson Med 2008, (114).

Table 2.1: Regional CBF in mice from 100x100x1000 µm^3 images (mean ± SD, n = 5). Adapted from Muir et al., Magn Reson Med 2008, (114).

Region of Interest	**CBF (ml/g/min)**
Whole brain	1.07 ± 0.08
1. Frontal cortex	1.00 ± 0.14
2. Sensory-motor cortex	0.92 ± 0.14
3. Caudate putamen	1.08 ± 0.06
4. Thalamus	1.18 ± 0.08
5. Hippocampus	1.28 ± 0.08
6. Corpus callosum	0.53 ± 0.10
7. Cerebellum	1.08 ± 0.15
8. Superior colliculus	1.18 ± 0.15
9. Inferior colliculus	1.51 ± 0.42
10. Pons	1.40 ± 0.21

2.2.2 Cerebral Blood Flow Changes During Hypercapnia

The CBF fMRI time course during hypercapnic challenge from a single measurement in one animal is shown in Figure 2.3. The group-averaged hypercapnia-induced CBF percent change was 33 ± 16 % (mean ± SD, n = 5).

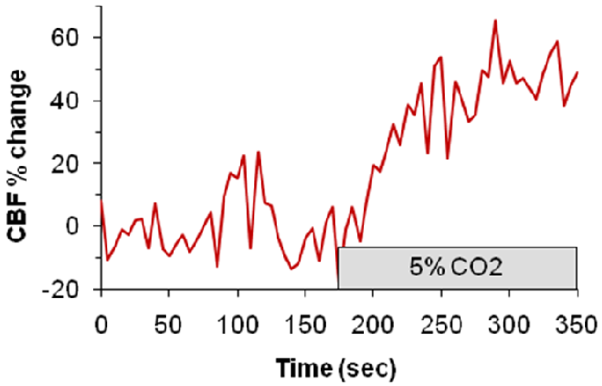

Figure 2.3: Time-course of CBF percent change due to hypercapnia from a single mouse. Five percent CO_2 was switched on half way through the trial as shown by the gray bar. Adapted from Muir et al., Magn Reson Med 2008, (114).

2.3 Discussion

Cardiac ASL provides a practical approach to image quantitative CBF and physiologically evoked CBF changes in mice with the high sensitivity of continuous ASL. This technique overcomes existing limitations and offers the following advantages: 1) Multi-slice, quantitative, high-resolution CBF images and CBF fMRI can be obtained with high sensitivity without magnetization-transfer effect. 2) The distance between the heart and the brain in mice avoids saturation of the brain signal by the label coil. 3) CBF of the cerebellum and brain stem can be imaged in contrast to two-coil ASL in rats where the cerebellum and brain stem are often not reported due to saturation artifacts by the neck labeling coil. Moreover, BF MRI in other body parts within reasonable transit time, such as the kidneys and liver, might be possible. With a neck coil labeling which labels only the carotid arteries, this would not be possible. Cardiac ASL MRI has the potential to broaden BF MRI utility in mice and other similar size species.

2.3.1 Cardiac Arterial Spin Labeling Applied to Cerebral Blood Flow

Labeling efficiency: Labeling efficiency was measured to be 0.73 ± 0.06, consistent with many published data, with reported values of about 0.7 at 1.5 and 3 Tesla (69,115,116), 0.75 at 4.7 Tesla (117), and 0.8 at 9.4 Tesla (118). The labeling efficiency for cardiac ASL in mice was measured at imaging planes positioned at the brain, as opposed to the carotid arteries in the neck. Thus, the labeling efficiency measurement includes the T_1 relaxation of the blood due to the transit time. Assuming transit time is relatively constant between animals, this avoids the need for measuring transit time, which is difficult to do.

In initial measurements of labeling efficiency in the carotid arteries under the cerebellum, the labeling efficiency was fairly low, about 0.63. Labeling efficiency was measured at three different slice positions in the posterior-anterior axis, ranging from the carotid arteries under the cerebellum to the distal internal carotid arteries under the frontal lobe (covering about a 7 mm range). Labeling efficiencies increased from 0.63 at the carotid arteries under the cerebellum to 0.73 at the distal internal carotid arteries in the center and anterior slices. This indicated that at higher labeling powers, some saturation was present in the posterior due to the cardiac labeling coil. Labeling efficiency thus had to be measured at the distal internal carotid arteries, which had no noticeable saturation effects from the cardiac labeling coil.

Blood flow calculation: Quantitative CBF measurement by MRI is susceptible to errors. The main sources of errors include magnetization-transfer (119,120), transit-time (121,122) and water-exchange effect (74,123). Magnetization-transfer effect was not an issue for continuous ASL herein because a separate labeling coil with active decoupling of the imaging coil was used. Although transit time was not explicitly taken into account in the calculation of CBF herein, the measurement of labeling efficiency at the brain should account for T_1 relaxation of labeled blood during the transit to the imaging slices. Additionally, transit time has been shown to have minimal effects on quantification of CBF in rats because of the small distances and short transit times (124). Because of the multi-slice acquisition, different image slices may have slightly different transit time, but again this should be minimal due to the small size of rodents and rapid EPI acquisition. The single compartment model used in CBF calculation assumes that all blood water exchanges into the tissue, which is not true. Water-exchange effect is generally more significant in white matter than in gray matter because of its larger T_1 difference from blood T_1 (74). It has been shown that water-exchange effects and venous outflow are at least partly compensated by the presence of labeled blood in the capillary space (74). Comparison of different CBF quantification models, including those accounting for water exchange across the blood-brain barrier, indicates that CBF values obtained using different models were overall similar although there are some distinct differences (62).

Quantitative CBF in mice: The group-average whole-brain CBF in mice was 1.07 ± 0.08 ml/g/min under 1.2% isoflurane. This is consistent with CBF values in rats, which ranged from 0.76 to 1.1 ml/g/min (52,125), that were obtained using continuous ASL MRI with a separate neck coil obtained under essentially identical experimental conditions. Quantitative CBF in mice has also been reported using destructive techniques, predominantly iodoantipyrine autoradiography. CBF from these methods was 0.99-1.59 ml/g/min under 1.0% halothane (126), 0.5-1.0 ml/g/min under equithesin anesthesia (127). These values are similar to the cardiac ASL measurements in mice.

However, CBF values from cardiac ASL in mice are lower compared to single-coil ASL techniques in mice, with values of 1.7-2.8 ml/g/min under 2% isoflurane (108) and 1.5-2.0 ml/g/min under 1% halothane (107). These single-coil approaches imaged one slice at comparatively lower spatial resolution. It is important to note that isoflurane is a known vasodilator. Previous studies have shown that rat CBF under 1% isoflurane anesthesia was substantially higher than under awake conditions in the same animals (128) and under α-chloralose in separate animals (129). Moreover, increasing isoflurane from 1% to 2% has been reported to increase CBF from 0.87 ± 0.27 to 1.31 ± 0.30 ml/g/min in the same animals (130). Halothane has been reported to be have a stronger vasodilatory effect than isoflurane in humans (131) and rats (132). The discrepancy between cardiac ASL and single-coil ASL techniques could be due to methods, including CBF model equation, and anesthetics.

2.3.2 Cerebral Blood Flow Changes During Hypercapnia

The CBF percent change was found to be 33 ± 16 % during hypercapnia. Using pulsed ASL in isoflurane-anesthetized mice, carbogen (95% O_2 and 5% CO_2) has been found to increase CBF by 14-30%, compared to 100% O_2 (133). Hypercapnia-induced CBF changes in mice, as measured by laser speckle flowmetry, have been reported to increase 40-55% under α-chloralose (134), 15% under 1% isoflurane (134), and 60-75% under urethane/α-chloralose (135). In rats, hypercapnia-induced CBF increase has been reported as 60%, using MRI (52) and under essentially identical experimental conditions as used herein for mice. The hypercapnia-induced CBF increase from cardiac ASL is higher than measurements made in mice with laser speckle flowmetry made under isoflurane but lower than in rats under isoflurane with MRI. Comparison to measurements made under different anesthetics is difficult since isoflurane is known to reduce vascular responses (134).

2.4 Conclusions

The cardiac ASL method provides a practical approach to image whole-brain CBF in mice *in vivo* with excellent BF contrast and SNR. Previous reports of CBF in mice acquired with MRI were limited to a single slice due to the use of a single coil, but the two-coil cardiac ASL method could provide whole-brain CBF, including the cerebellum and brain stem. Signal-to-noise ratio, spatiotemporal resolution, multi-slice and fMRI capability of cardiac ASL MRI compare favorably with existing approaches for mice. This approach could provide a valuable tool to study numerous brain disease and transgenic models available in small animals, including stroke and Alzheimer’s disease.

CHAPTER 3

LAYER-SPECIFIC BLOOD FLOW OF THE MOUSE RETINA AND CHOROID

The retina is nourished by two distinct circulations, the retinal vessels within the inner retina and the choroid vessels behind the neural retina. The outer nuclear layer and the inner and outer segments of the photoreceptors in between are avascular (22). There are substantial differences in basal blood flow (BF) and regulation of BF between the two blood supplies (22,25,26,34,35,37), so it is important to be able to distinguish the two vasculatures in studying BF to the retina. This requires that any technique used has no depth limitation and high resolution. BF imaging with ASL MRI is quantitative, not-depth limited, and is non-invasive. However, ASL is limited by low SNR and low resolution, so its application to layer-specific BF imaging of the retina and choroid is challenging.

The continuous ASL technique with cardiac labeling proved capable of imaging cerebral BF (CBF) in mice with good SNR and BF contrast in relatively short time (114). Thus, this technique was promising for BF studies of the mouse retina. High-resolution cardiac ASL was utilized to image quantitative, layer-specific retinal BF (rBF) and choroidal BF (chBF) in the mouse retina at 42x42x400 μm^3 resolution. Basal BF in the retina and choroid was measured under two anesthetic regimens – isoflurane, a vasodilatory anesthetic (136), and ketamine/xylazine, a vasoconstrictive anesthetic cocktail (137,138) – to test the sensitivity of ASL MRI to detect differences in BF. This method was then applied to acquire layer-specific BF fMRI of the retina and choroid using hypoxic challenge as a stimulation.

3.1 Basal Blood Flow of the Retina and Choroid

3.1.1 Methods

Animal preparation: Experiments were performed on C57BL/6 mice (4 female, 3 male, 5-11 weeks old, 17-28 g, $n = 7$). Animals were anesthetized with isoflurane, put into a head holder with ear and tooth bars, and placed in an animal holder with a circulating warm water pad. An intraperitoneal line was placed in the animal to administer drugs during MRI without moving the animal. Imaging was performed first under 1.1% isoflurane and spontaneous breathing conditions. In the same animals, anesthesia was subsequently switched to ketamine - xylazine (100 mg/kg - 10 mg/kg, intraperitoneal) and isoflurane was discontinued. MRI was repeated 10 min after switching of the anesthetics. Air and oxygen were mixed to provide 30% O_2 to the animals during imaging under both anesthetics. MRI under isoflurane was performed first in all mice because its half-life is much shorter compared to ketamine/xylazine, allowing the two anesthetics to be studied on the same animals in the same setting within reasonable time, thereby reducing inter-subject variation.

Respiration rate was monitored and was ~115 breaths/min under isoflurane and ~95 breaths/min under ketamine/xylazine. Rectal temperature was monitored and maintained at 37 ± 0.5° C. Mice were prepared in a lit room before being transferred to the MRI room, in which lights were turned off. Lighting conditions were not changed during the duration of imaging. Additionally, some mice (n = 4) were euthanized in the scanner after in vivo experiments with sodium pentobarbital (250 mg/kg, intraperitoneal) and BF imaging repeated a few minutes after respiration ceased.

MRI methods: MRI studies were performed on a 7 Tesla, 30 cm horizontal magnet and a 150 G/cm BGA6S gradient insert (Bruker, Billerica, Massachusetts). For imaging, a small circular surface eye coil with active decoupling (diameter = 6 mm) was placed over the left eye. A circular labeling coil (diameter = 8 mm) was placed at the heart position for a cardiac ASL technique (114). The two coils were separated by about 2.3 cm from center to center.

BF MRI was acquired using two-coil continuous ASL with an echo planar imaging (EPI) sequence. Paired images, one with and one without labeling, were acquired in an interleaved fashion. ASL employed a 2.94 s square radio frequency pulse to the labeling coil in the presence of 2.0 G/cm gradient along the flow direction with a post label delay of 10 ms. The sign of the frequency offset was switched for non-labeled images.

Images were acquired in a coronal orientation with a single slice passing through the retina at the optic nerve head, with the slice angled perpendicular to the retina. Two-segment, gradient-echo EPI was used with field of view = 6.0x6.0 mm^2, matrix = 144x144 (42x42 μm^2 resolution), a single 0.4 mm slice, TR = 3.0 s per segment, and TE = 13 ms. For each scan, seventy-five pairs of images were typically acquired in time-series (to be averaged off line) with a total acquisition time of 15 min.

Data analysis: Image analysis was done using codes written in Matlab (Math-Works, Natick, MA), STIMULATE software (University of Minnesota), and Statistical Parametric Mapping 5 (SPM5) software. Images were zero-padded to 256x256 (nominal resolution of 23x23 μm^2) before Fourier transform into imaging space. All images from each scan were acquired as time series, aligned using the spatial realignment function in SPM5 and averaged off line.

BF images of the eye, in units of ml/g/min, were calculated pixel-by-pixel using Eq. 1.1. λ, the water tissue-blood partition coefficient, was taken to be 0.9, the same as the brain (64). λ, a difficult measurement, has not been reported for the retina or choroid. The retina and choroid T_1 at 7 Tesla was taken to be 1.8 s (68) which is similar to brain T_1. A value of 0.7 was used for α, the labeling efficiency, as was previously measured in the distal internal carotid arteries at the base of the frontal lobe (see Chapter 2) (114).

BF intensity profiles across the retinal thickness were obtained from BF images by radially projecting lines perpendicular to the retina (9,139) with profiles obtained at 4x spatial interpolation. Figure 3.1 demonstrates the steps in the profile analysis of the retina. BF profiles were averaged along the length of the retina. Measurements of peak values and layer thicknesses – defined as the half-height width of peaks – were determined from the average BF profiles for each animal.

Since there was no BF after death, post-mortem BF measurements were made by aligning post-mortem anatomical profiles to the anatomical profiles obtained under isoflurane. The locations of rBF and chBF peaks were determined from the isoflurane BF profile. rBF and chBF were measured from the post-mortem BF profile by averaging over nine pixels centered at the respective BF peak. Group-average data were expressed as mean ± SD. Statistical analysis of BF data used two-sided, paired t-tests. Analysis of thickness data used the Wilcoxon rank-sum test. For all tests, $p < 0.05$ indicated statistical significance.

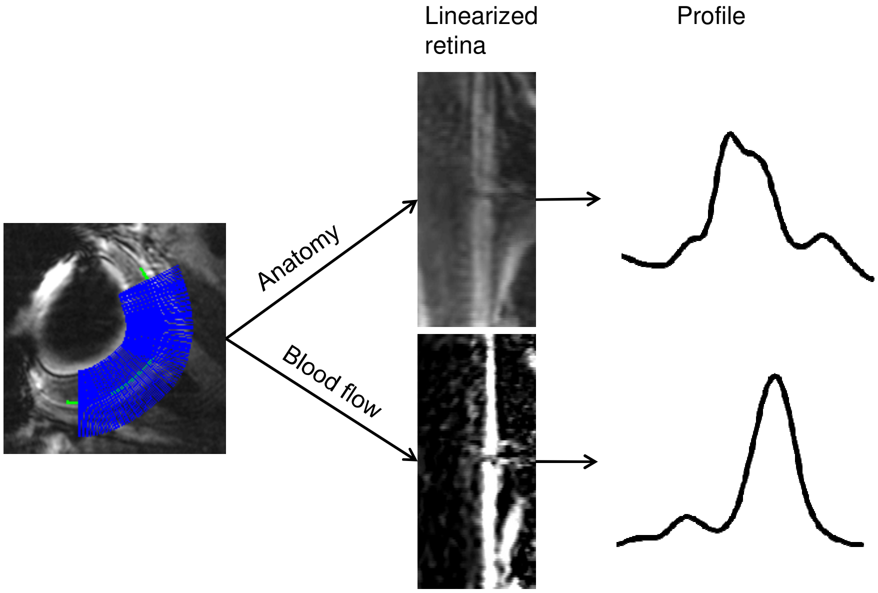

Figure 3.1: Profile analysis of BF MRI data. The image on the left shows an EPI image of the eye. The blue lines on the left image show the profiles taken perpendicularly to the retina. The profiles can then be used to create a linearized representation of the retina, including anatomy and BF images (center images). All the profiles consisting of the linearized retina can be averaged, to give an average profile for the entire length of the retina (right images).

3.1.2 Results

With a resolution of 42x42x400 μm^3, two distinct BF layers in the retina were resolved, separated by a region of no BF contrast (Figure 3.2 A). The outer BF layer, which corresponds to the choroid, had very high BF. The inner BF layer, which corresponds to the retinal vessels, had substantially lower BF than the choroid. The middle layer with little to no BF contrast corresponds to the avascular region – made up of the outer nuclear layer and the outer and inner photoreceptor segments. BF signals in the ciliary bodies and extra-ocular tissue were also detected sometimes, although not clearly or consistently due to susceptibility-induced signal dropout in the anterior regions of the eye. No statistically significant BF signal was detected in the vitreous or lens ($p > 0.05$, one sample t-test comparing the sample mean to 0, $n = 7$). Figure 3.2 B shows a BF image obtained from the same mouse post-mortem. No BF contrast was detected in the dead animals ($p > 0.05$ for both rBF and chBF, one sample t-test comparing the sample mean to 0, $n = 4$), suggesting that BF was the source of signals in vivo. The BF profiles in Figure 3.2 C show two BF layers distinctly separated by an avascular region in the live mouse and the absence of BF contrast in the dead mouse retina.

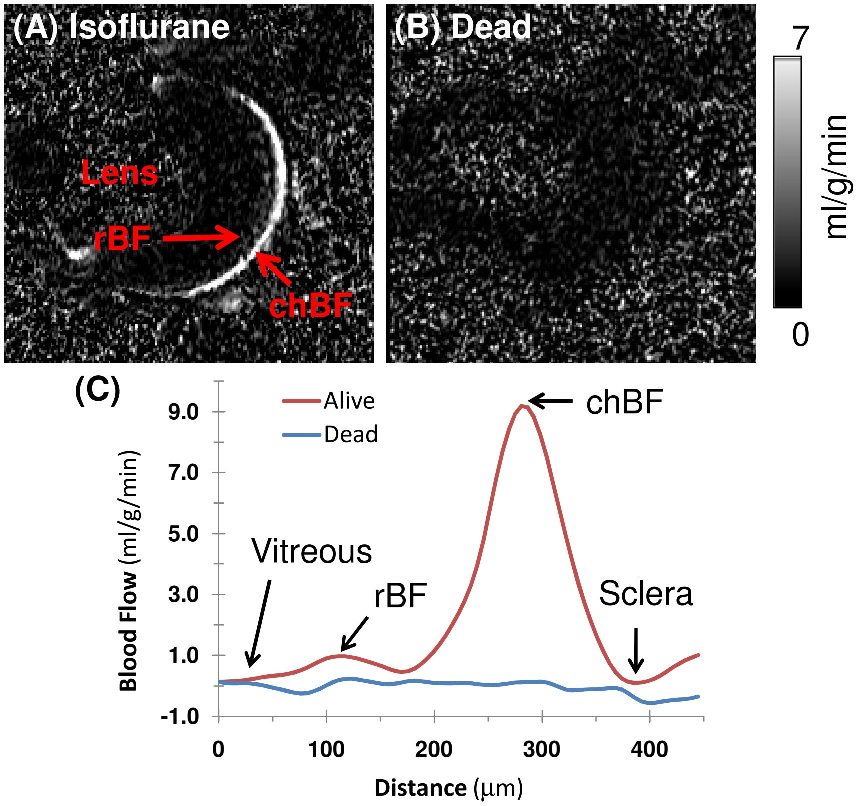

Figure 3.2: (A) Layer-specific blood flow image from a mouse under 1.1% isoflurane. (B) Blood flow acquired in the same mouse after euthanasia. (C) Blood flow profiles from the images in (A) and (B). chBF – choroid blood flow, rBF – retinal blood flow. Adapted from Muir et al., NMR Biomed 2010, (139).

Layer-specific BF measurements were made under isoflurane (Figure 3.3 A) and ketamine/xylazine (Figure 3.3 B). Group-averaged BF profiles under each anesthetic are shown in Figure 3.3 C. Retinal BF and chBF were both substantially lower under ketamine/xylazine compared to isoflurane.

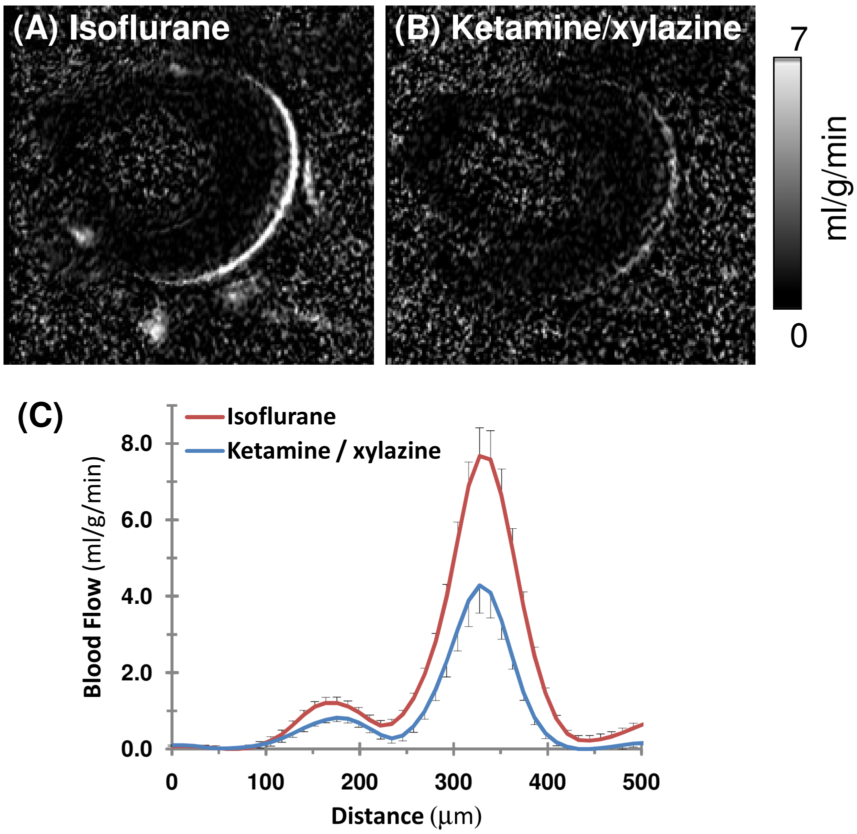

Figure 3.3: Blood flow image in a mouse under (A) 1.1% isoflurane, and (B) ketamine/xylazine (100 mg/kg - 10 mg/kg). (C) Group-average blood flow profiles across the retinal thickness under isoflurane or ketamine/xylazine from the same animals (n = 7, error bars are standard error of the mean (SEM)). Adapted from Muir et al., NMR Biomed 2010, (139).

Table 3.1 summarizes the peak rBF and chBF values under each anesthetic. BF under ketamine/xylazine was 42% lower in the choroid ($p < 0.01$, n = 7) and 29% lower in retinal vessels ($p < 0.01$), compared to isoflurane. The ratio of chBF:rBF was 6.3 under isoflurane and 4.8 under ketamine/xylazine, suggesting that these anesthetics affect rBF and chBF differently. The magnitude changes of chBF and rBF between anesthetics, -3.4 and -0.42 ml/g/min respectively, were significantly different from each other ($p < 0.05$). The group average standard deviations across acquisition time for isoflurane were 0.22 and 0.53 ml/g/min for rBF and chBF, respectively. The group average standard deviations across time for ketamine/xylazine were 0.33 and 0.36 ml/g/min for rBF and chBF, respectively.

Table 3.1: Blood flow peak values (ml/g/min) of the retinal and choroidal layers under isoflurane or ketamine/xylazine (mean ± SD, n=7). Adapted from Muir et al., NMR Biomed 2010, (139)
[a] $p < 0.01$ compared to isoflurane, [b] $p < 0.01$ compared to rBF

	rBF (ml/g/min)	chBF (ml/g/min)	chBF / rBF
Isoflurane	1.3 ± 0.44	7.7 ± 2.1[b]	6.3 ± 1.9
Ketamine/Xylazine	0.88 ± 0.22[a]	4.3 ± 1.9[a, b]	4.8 ± 1.2
% Difference	-29 ± 17	-42 ± 23	

Based on the BF profiles, thicknesses of the retinal and choroidal vascular layers and the avascular layer in between were estimated (Table 3.2). Average thickness of the retina, including the choroid, was about 249 μm under isoflurane and ketamine/xylazine ($p > 0.05$, $n = 7$). The distances between the rBF and chBF peaks were 170 μm (isoflurane) and 161 μm (ketamine/xylazine) ($p > 0.05$).

Table 3.2: Thicknesses (μm) of retinal BF peak, avascular layer, choroidal BF peak, and peak-to-peak distance between retinal and choroidal vasculatures (mean ± SD, n = 7). Adapted from Muir et al., NMR Biomed 2010, (139)

	Retinal Layer	Avascular Retina	Choroid Layer	Total Thickness	Peak to Peak Distance
Isoflurane	77 ± 24	94 ± 13	78 ± 3	249 ± 19	170 ± 18
Ketamine/Xylazine	84 ± 26	87 ± 6	78 ± 10	249 ± 28	161 ± 17

3.1.3 Discussion

This study demonstrates non-invasive, high-resolution, quantitative blood flow measurements of the retinal and choroid vasculature in the mouse retina *in vivo*. This was made possible by the novel cardiac spin labeling BF MRI and a high-performance gradient. Choroidal BF was many times higher than rBF. Additionally, rBF was 29% lower while chBF was 42% lower under ketamine/xylazine compared to isoflurane. This approach allows quantification of rBF and chBF as well as detecting differences between the two anesthetics. MRI ASL BF measurement is: 1) non-invasive which would allow longitudinal monitoring of disease progression in vivo, 2) quantitative which facilitates comparison across experimental groups, and 3) depth-resolved with high spatial resolution which allows unambiguous resolution of rBF and chBF. This novel application of BF MRI could serve as a valuable imaging tool to study rBF and chBF regulation in normal retinas and perturbations in retinal diseases in a longitudinal fashion.

Movement and partial-volume effect: In contrast to previous studies of the rat retina in which paralytics were found to be needed in addition to isoflurane (9,140), eye movement in movies of time-series MRI from isoflurane-anesthetized mice was considerably less, so paralytic was not used. Any small motion that did occur over prolonged scans was tolerable and effectively corrected by image alignment. While both isoflurane and ketamine/xylazine were effective in minimizing eye movement in mice, ketamine/xylazine yielded more stable images than isoflurane in the same animals, likely because xylazine is also a muscle relaxant (137).

The in-plane resolution of 42x42 μm^2 (before zero filling and interpolation) had ~6 pixels across the entire retina and choroid. This spatial resolution was sufficient to clearly differentiate BF between the retinal and choroidal vascular layers. In the slice thickness direction, the partial-volume effect due to the curvature of the retina from a slice thickness of 0.4 mm was estimated to be 12 μm or < 5% of total retinal thickness, from a simulation assuming a spherical eye of 3.3 mm diameter and a 270 μm thick retina (combined neural retina and choroid).

Blood flow calculation: The ASL technique for imaging the retina and choroid has some assumptions and limitations. The blood-tissue partition coefficient (λ) of the brain (64) was used in the BF calculations because the blood-tissue partition coefficient in the retina and choroid have not been measured. This is a reasonable assumption for the retina because it is neural tissue and has similar BF and water content as gray matter (64,66). In this study, the effect of transit time on blood flow measurements was not taken into consideration. In rats, transit time to the brain is short, ~200 ms (124), and in mice, the transit time is expected to be shorter. Additionally, the labeling efficiency used was measured at the brain (114), modeling the transit delay effects as a modulation of labeling efficiency.

However, there could be a slight transit time difference between the two anesthetics which may cause some error in BF comparison, although this should likely be insignificant in small animals such as mice. In some disease states such as vascular occlusive diseases, the effect of transit time could be significant and would need to be corrected by using appropriate post-labeling delays. T_1 of the retina and choroid have been reported to be about 1.8 s at 7 Tesla, similar to brain T_1 (68). It has also been reported at 11.7 Tesla that retina and choroid T_1 are similar to brain T_1 (19). BF errors from λ and T_1 inaccuracies are likely small and cause only a linear scaling. As such, reliable comparison across experimental groups can still be made at the least if the experimental settings were similar.

Thickness measurements from BF data: Images acquired with EPI had relatively low resolution compared to the retina and had noticeable geometric distortion which likely introduces some error in thickness measurements. Thicknesses derived from the BF MRI should still be reasonably close to the ranges measured from histology. The neural retina (including rBF layer and avascular layer) determined by BF MRI was about 171 μm. The neural retina has been reported to be 182 μm in mice (19) and 180 μm in rats (9) by anatomical MRI. Histological thickness measurements of the neural retina were 176-223 μm in mice (19,141,142) and 169 μm in rats (9). Neural retinal thickness in mice and rats by MRI and histology are in reasonably good agreement.

The choroid thickness was 78 μm by BF MRI, consistent with the choroid thickness of 86 μm reported in rats (9), although somewhat thicker than 52 μm reported in mice (19) with anatomical MRI. Choroid thickness measured by histology is 15-28 μm in mice (19,142) and 37 μm in rats (9), thinner than MRI measured thicknesses. Similar differences have been noted in humans between *in vivo* measurements of choroid thickness using optical coherence tomography (143) compared to histological measurements (144). Possible explanations for this difference include partial-volume effect from the limited in-plane MRI spatial resolution, histological shrinkage, and collapse of choroid vessels after being removed from the systemic circulation for histology. The peak-to-peak distances between the rBF and chBF profiles were 170 and 161 μm in this study, under isoflurane and ketamine/xylazine, respectively, comparable to the peak-to-peak distance of 162 μm in rats measured by anatomical MRI (9).

Quantitative rBF and chBF: Under isoflurane, rBF was 1.3 ml/g/min and chBF was 7.7 ml/g/min. Under ketamine/xylazine, rBF was 0.88 ml/g/min and chBF was 4.3

ml/g/min. Retinal BF and chBF have been reported using destructive techniques including microspheres, autoradiography, krypton-85 washout, and hydrogen clearance methods. Table 3.3 summarizes the results from these methods in various species and experimental conditions. Values of rBF are seen to range from 0.12-3.73 ml/g/min while chBF ranges from 2-18.98 ml/g/min. The MRI BF measurements fall somewhere in the middle of these reported ranges.

Table 3.3: Reported values of retinal, choroidal, and cerebral blood flow (rBF, chBF, and CBF respectively) in ml/g/min, except where noted. Adapted from Muir et al., NMR Biomed 2010, (139)

Ref	Method	Animal	Anesthesia	rBF	chBF	CBF
(22)	microspheres	monkey		0.48	18.98	0.78
(35)	microspheres	cat	urethane	0.198		
(7)[a]	microspheres	cat	a-chloralose	0.141	7.46	
(25)	microspheres	cat	halothane	0.54	13.09	0.69
(26)	microspheres	rat	Inactin	0.44	1.42[b]	0.58
(145)	microspheres	rat	thiopental	0.4	3.8[b]	0.58
(27)	microspheres	rat	halothane[c]	0.22	1.45[b]	
(146)	microspheres	dog	pentobarbital	0.12	9.61	
(147)	microspheres	dog	pentobarbital/succinylcholine	0.91		
(28)	autoradiography	rat	awake	0.92		0.97
(148)	krypton-85	cat	pentobarbital	1.66	12	
(95)	H_2 clearance	rat	Inactin	3.73		
(92)	H_2 clearance	cat	a-chloralose	0.56		
(91)	H_2 clearance	dog	pentobarbital/thiopental		2-4	

[a] Values reported as g/g/min. Given that blood density is 1.06 g/ml (64), values in g/g/min and ml/g/min units are essentially equal.

[b] Values are of the combined choroid and sclera, likely reducing the quantitative value substantially.

[c] Ketamine/xylazine were given during surgery, so they could have some lingering effect on BF.

These comparisons show that rBF and chBF measurements vary over a wide range. Factors that could contribute to this spread include differences in species, anesthetics, and methodologies. The extent of the retinal vasculature varies widely in mammals, with some species even completely lacking this vascular layer (149,150), giving rise to large species difference. As demonstrated different anesthetics and dosages have marked effects on BF (151). MRI BF measurements have some assumptions as described above. The size and dose of microspheres can also have significant effects on measurement of rBF and chBF (90). BF in the eye measured by microspheres is often given in units of µl blood/min/whole tissue. Conversion to ml/g/min requires the weight of whole neural retina and whole choroid. Such conversion could introduce inaccuracies in quantitative values through dehydration of tissue before weighing, difficulty separating the whole retina and choroid from other tissues, and use of the entire retina weight when the retinal vessels only perfuse the inner retina (7,35).

Regardless of experimental conditions or units, chBF has been consistently reported to be many times higher than rBF (7,22,35,148,152), with the chBF:rBF ratios ranging from 7 (148) to 80 (146). In this study, MRI measured chBF to be 6.3 times larger than rBF under isoflurane and 4.8 times larger under ketamine/xylazine, most consistent with findings using the krypton-85 washout method (148). High chBF also agrees with a previous MRI study which reported combined rBF and chBF in rats at a resolution that was insufficient to resolve the retinal and choroid vascular layers as 6.3 ± 1.0 ml/g/min under 1% isoflurane and similar experimental conditions to those used herein (151).

Table 3.3 also summarizes CBF data measured in the same animals as rBF and chBF. By comparison, chBF is many time higher than CBF, whereas rBF is similar to CBF. CBF has been reported to be 0.86-1.27 ml/g/min in rats (128) and 1.1 ml/g/min in mice (see Chapter 2) (114) under 1% isoflurane, similar to rBF (1.3 ml/g/min) but much lower than chBF (7.7 ml/g/min) measured herein. Together, these comparisons support the validity of MRI ASL BF measurements in the retina and choroid.

Effects of different anesthetics: Isoflurane is a known vasodilator. BF under isoflurane is higher than awake conditions in the brain (128,136), and higher isoflurane concentration yields higher CBF up to 2% isoflurane (128,136). In the rat retina, total BF (combined rBF and chBF) under 1.5% isoflurane was 48% higher compared to 1.0% isoflurane (151), showing similar effects as in the brain. However, in the cat eye, halothane caused rBF to increase while chBF decreased (25). In contrast, ketamine/xylazine is known to cause vasoconstriction and has been shown to yield 25-65% lower CBF compared to isoflurane, depending on brain region (138).

Both rBF and chBF were higher under isoflurane compared to ketamine/xylazine, consistent with the anesthetic effects in the brain. This is likely the combined effects of the removal of vasodilatory isoflurane and the addition vasoconstrictive ketamine/ xylazine. Choroidal BF under ketamine/xylazine was 42% lower, but rBF under ketamine/xylazine was only 29% lower compared to isoflurane. These changes could be due to systemic effects of the anesthetics or local effects, which could explain the large BF difference in the choroid.

Systemic respiratory, cardiovascular, or metabolic differences between the two anesthetics could account for these global BF differences. The respiration rate was lower under ketamine/xylazine compared to isoflurane, which could potentially result in lower partial pressure of arterial oxygen (PaO_2) and higher partial pressure of arterial carbon dioxide ($PaCO_2$) (137,138). These changes could not explain the lower BF under ketamine/xylazine because they should increase BF. Ketamine/xylazine does not have significant effect on blood pressure relative to isoflurane in rats (138), but xylazine has been reported to cause an initial hypertension followed by a return to normal or low blood pressure (137).

Xylazine could affect rBF and chBF differently. Xylazine is an α2-agonist which binds central and peripheral α2-adrenoreceptors in the sympathetic nervous system. (137). The choroid contains sympathetic nerves which can induce vasoconstriction (43,44,153) while retinal vessels lack direct sympathetic innervation (44,153). This could explain why ketamine/xylazine reduced chBF more than rBF.

3.2 Layer-Specific Blood Flow Functional MRI with Hypoxic Challenge

3.2.1 Methods

Animal preparation: Experiments were performed on C57BL/6 mice (female, 17-25 g, n = 7). Mice were imaged under 1.2% isoflurane and spontaneous breathing conditions. Animals were placed in an animal holder with ear and tooth bars. Respiration rate and rectal temperature (37 ± 0.5^{o} C) were monitored and maintained within normal physiological ranges. Baseline conditions consisted of 30% O_2 in balance nitrogen. Mice were prepared in a lit room before being transferred to the MRI room, in which lights were turned off. Lighting conditions were not changed during the duration of imaging.

Hypoxic challenge used premixed gas of 10% O_2 and balance N_2. The baseline consisted of 30% O_2 with balance N_2. Each trial consisted of a 9 min scan with baseline conditions during the first 4.5 min of the trial and hypoxia during the second 4.5 min. A 10 min break was given between trials for the animals to return to normal physiologic conditions. Two repeated measurements were typically made.

MRI methods: MRI studies were performed on a 7 Tesla, 30 cm horizontal magnet and a 100 G/cm BGA6S gradient insert (Bruker, Billerica, Massachusetts). For imaging, a small circular surface eye coil with active decoupling (diameter = 6 mm) was placed over the left eye. A circular labeling coil (diameter = 8 mm) was placed at the heart position for a cardiac ASL technique (114). The two coils were separated by about 2.3 cm from center to center.

BF MRI was acquired using two-coil continuous ASL with an inversion-recovery, echo planar imaging (EPI) sequence. Paired images, one with and one without labeling, were acquired in an interleaved fashion. ASL employed a 2.1 s square radio frequency pulse to the labeling coil in the presence of 2.0 G/cm gradient along the flow direction with a post label delay of 10 ms. The sign of the frequency offset was switched for non-labeled images. MRI was acquired with inversion-recovery to suppress the strong vitreous signal and reduce noise and motion artifacts in BF images. The inversion pulse was an adiabatic 20 ms hyperbolic secant pulse, occurring prior to the application of the labeling pulse.

Images were acquired in a coronal orientation with a single slice passing through the retina at the optic nerve head, with the slice angled perpendicular to the retina. Inversion-recovery, gradient-echo EPI was used with field of view = 6.0x6.0 mm^2. Basal BF images (n = 7) were acquire with 2 segments, matrix = 144x144 (42x42 μm^2), a single 0.4 mm slice, TR = 4.0 s, TE = 11.7 ms, and inversion time = 2.12 s. fMRI of hypoxia (n = 7) was acquired with a single segment, matrix = 128x128 or 112x112 (47x47 μm^2 or 54x54 μm^2), a single 0.6 mm slice, TR = 4.0 s, TE = 12.7 or 14.9 ms, and inversion time = 2.12 s. For quantitative calculation of BF, regular gradient-echo EPI scans (without inversion recovery) were also acquired. The imaging parameters were otherwise the same, except for TR = 3.0 s.

Data analysis: Image analysis was done using codes written in Matlab (MathWorks, Natick, MA), STIMULATE software (University of Minnesota), and Statistical Parametric Mapping 5 (SPM5) software. Images were zero-padded to 256x256 for basal BF imaging or 128x128 for fMRI imaging before Fourier transform into imaging space. All images from each scan were acquired as time series, aligned using the spatial realignment function in SPM5 and averaged off line.

Blood flow images of the eye, in units of ml/g/min, were calculated pixel-by-pixel using Eq. 3.1. M_0 is the equilibrium value of the magnetization of the object, which was approximated as the gradient-echo EPI images without inversion recovery. λ, the water tissue-blood partition coefficient, was taken to be 0.9, the same as the brain (64). The retina and choroid T_1 at 7 T was taken to be 1.8 s (68) which is similar to brain T_1. A value of 0.7 was used for α, the labeling efficiency, as was previously measured in the distal internal carotid arteries at the base of the frontal lobe (114). The labeling duration, LD, was 2.1 s.

$$BF = \frac{\lambda}{T_1} \cdot \frac{M_{NL} - M_L}{2\alpha \cdot M_0 \cdot (1 - e^{-LD/T_1})} \qquad \text{(Eq. 3.1)}$$

Profile analysis was used to calculate basal BF values, BOLD %-changes, and magnitude and BF %-changes. Anatomy and BF intensity profiles across the retinal thickness were obtained from the images by radially projecting lines perpendicular to the retina (9,139) with profiles obtained at 8x spatial interpolation. Further motion correction was performed on the extracted profiles in Matlab (see Chapter 4.2 for details). The inversion-recovery and regular EPI images were aligned separately, and then the averaged anatomical profiles from both scans were both manually aligned before BF calculation.

Percent-change BOLD profiles were calculated from the anatomical profiles of the non-labeled images and averaged across the length of the retina. The BOLD %-change was then measured as the peaks of the averaged BOLD profile located at the choroidal and retinal vasculatures. BF profiles were calculated using Eq. 3.1 and averaged along the length of the retina. BF values were obtained under baseline and hypoxic conditions separately, and then magnitude and percent BF changes were calculated from these values. Reported values come from the peak values of the profiles.

3.2.2 Results

Figure 3.4 shows a basal BF image at 42x42x400 μm^3 from a single animal and the group-averaged basal BF profile across the retina. Retinal and choroidal BF and the avascular layer in between were well resolved. Basal chBF at 42x42x400 μm^3 was 7.1 ± 1.4 ml/g/min, and rBF was 1.2 ± 0.24 ml/g/min (mean ± SD, n = 7). Basal chBF was 5.9 times higher than rBF. The BF images and quantitative values are similar to those previously found and reported in Section 3.1, in which inversion-recovery background suppression was not used.

Figure 3.5 shows BF and BOLD % change maps associated with hypoxia from a single animal. Hypoxia decreased BF and BOLD signals, with distinct responses in the retinal and choroid layer. Figure 3.6 shows profiles from the hypoxia fMRI, including BF under 30% and 10% O_2, the BF magnitude change, and the BOLD % change. Distinct layers corresponding to the retinal and choroidal vascular layers could be distinguished in the BF and BOLD fMRI profiles. Group-averaged data are summarized in Table 3.4. In magnitude, the decrease in chBF was 5.2 times more than rBF, but BF % changes were similar. Choroid BOLD % changes were 1.9 times larger than in the retinal vessels.

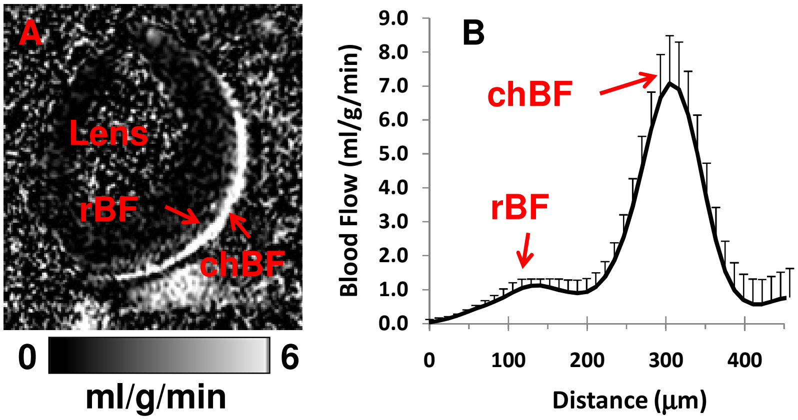

Figure 3.4: (A) Blood flow image from a mouse at 42x42x400 μm^3. (B) Group-average blood flow profiles across the retinal thickness (n = 7, error bars are SD). rBF – retinal BF, chBF – choroidal BF.

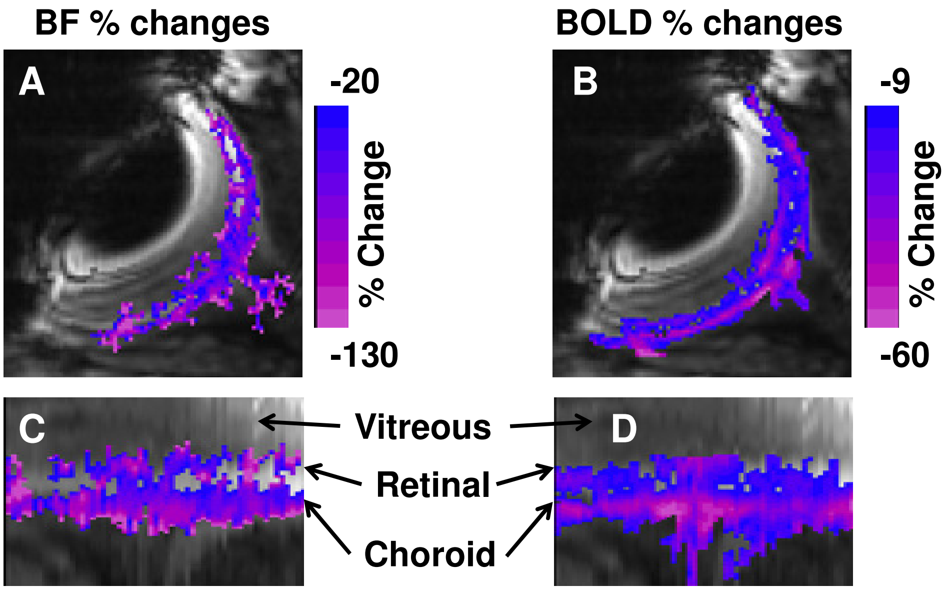

Figure 3.5: (A) BF and (B) BOLD % change maps due to hypoxia overlaid on the EPI image from a single mouse. (C) and (D) show corresponding images of the linearized retina.

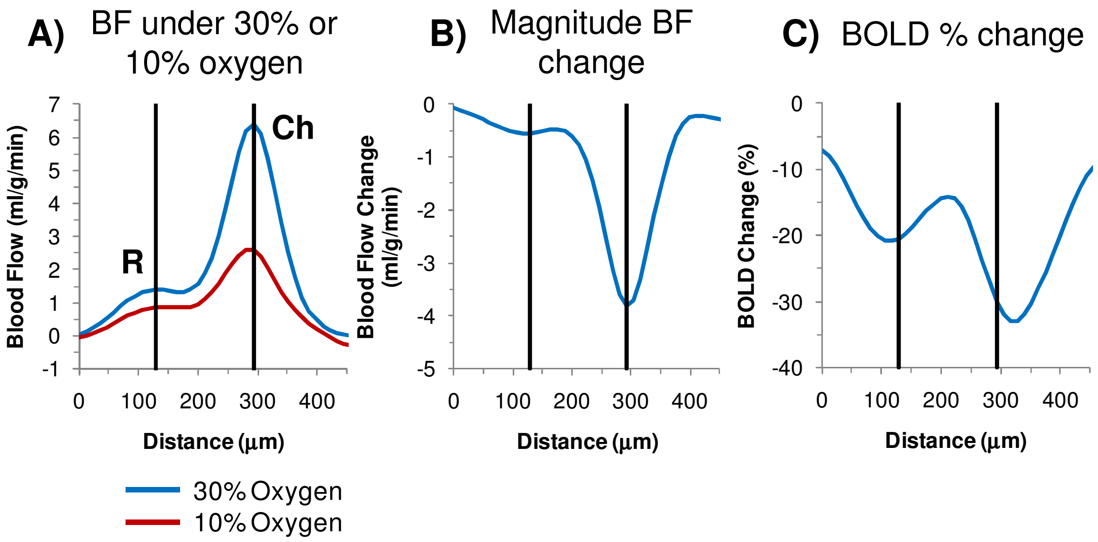

Figure 3.6: Profiles of BF and BOLD changes from one mouse. (A) BF profiles under 30% and 10% O_2. (B) BF magnitude-change profile calculated from the subtraction of the BF profile under 10% O_2 from the BF profile under 30% O_2. (C) BOLD %-change profile. The vertical black lines are located at the rBF and chBF peaks under 30% O_2. R – retinal vascular layer, Ch – choroid.

Table 3.4: Layer-specific basal BF and BF and BOLD responses to hypoxia (mean ± SD, n = 7) $^*p < 0.01$ compared to choroidal layer, $^\dagger p < 0.01$ compared to BF under 30% O_2

Vascular Layer	**Blood Flow**				**BOLD**
	BF under 30% O_2 (ml/g/min)	**BF under 10% O_2** (ml/g/min)	**Magnitude Change** (ml/g/min)	**Percent Change** (%)	**Percent Change** (%)
Retinal	$1.2 \pm 0.32^*$	$0.62 \pm 0.22^{*\dagger}$	$-0.58 \pm 0.31^*$	-47 ± 16	$-15 \pm 4.0^*$
Choroidal	5.9 ± 1.8	$2.9 \pm 0.95^\dagger$	-3.0 ± 1.6	-48 ± 16	-29 ± 10

3.2.3 Discussion

ASL MRI was able to detect layer-specific changes of BF and BOLD signals in the retina and choroid during hypoxic challenge. The BOLD signal was found to drop in the retina and choroid, as would be expected from hypoxia. BF of the retina and choroid was found to drop in response to hypoxia, opposed to an increase in BF as might be expected. Similar decreases in BF of the brain have also been reported (52,154). Two likely reasons for the decrease in BF are drops in mean arterial blood pressure and $PaCO_2$

which are generally found in acute hypoxic challenge. In rats (52) and mice (155,156), blood pressure has been reported to drop during hypoxia, which could cause decreased BF. In free breathing animals, hypoxia tends to cause increased respiration rate, which will cause hypocapnia, which is vasoconstrictive (154).

The magnitude decrease of chBF was significantly larger than rBF, but the percent decrease of chBF and rBF were almost the same due to the high basal chBF. The rBF responses to hypoxia were similar to the brain, in both magnitude and % changes. Hypoxia is reported to reduce CBF by 48% under similar conditions (154). The chBF magnitude change due to hypoxia was larger than that reported for CBF, while the % change of chBF and CBF were similar (154). These findings caution interpretation of BF fMRI %-changes in diseased states where basal BF is significantly altered.

If the changes in BF are actually in part due to hyperventilation-induced hypocapnia, then this offers an explanation for the large change in BF in the choroid. The retinal circulation is responsive to modulations of O_2 and CO_2, while the choroid has little response to O_2 but is responsive to CO_2 (33,157). This could potentially lead to large chBF decreases in response to hypoxia induced hypocapnia since there is no regulatory response to the low O_2, as in retinal or cerebral circulations. Additionally, the retinal and choroidal circulations may have differences in their autoregulation to changes in perfusion pressure to maintain BF. rBF is consistently reported to be autoregulated (38), while chBF is reported to have (41) and to lack (40) autoregulation. Thus, it is uncertain what affect a drop on blood pressure would have on the two vasculatures, but it might be that chBF has less autoregulatory ability and would then have a larger change in BF due to a drop in blood pressure.

The hypoxia-induced BOLD decrease was larger in the choroid compared to the retinal vascular layer. In the brain, hypoxia is reported to reduce BOLD by 9% (154), similar to the retinal response and lower than the choroidal response. The large choroid BOLD change compared to the retinal layer and the brain could be a result of high basal blood volume and vascular density of the choroid (23,158) or the large magnitude chBF decrease that occurred.

These findings demonstrated differential responses to hypoxia between the retinal and choroidal vasculatures. This is consistent with a previous MRI study which showed layer-specific BOLD responses to hyperoxia and hypercapnia in the rat retina at 90x90x1000 μm^3 (9). This is also consistent with laser Doppler flowmetry studies of hyperoxia and hypercapnia in the optic nerve head where retinal vessels dominate and in the fovea where retinal vessels are absent (159). A previous MRI study in rats reported BF changes of the retina in response to hyperoxia and hypercapnia, but at a resolution insufficient to resolve the retinal and choroidal vasculature (100).

3.3 Conclusions

It was demonstrated that MRI could be used to image layer-specific blood flow to the retina and choroid for the first time, providing both basal BF and functional BF changes. Quantitative retinal and choroid BF could be clearly resolved *in vivo* by high-resolution MRI. The BF MRI approach was capable of detecting the effects of isoflurane and ketamine/xylazine anesthesia on rBF and chBF. Additionally, the feasibility of layer-specific BF fMRI was demonstrated using hypoxic challenge. MRI has the potential to provide information on the unique rBF and chBF regulation in the normal retina, and rBF and chBF dysregulation in disease states. Quantitative blood flow measurement affords comparison of BF changes between experimental groups, facilitating early detection and monitoring of treatment efficacy. The BF fMRI technique could provide a means of studying neurovascular coupling of the retinal and choroid vessels in disease states as well.

CHAPTER 4

PASSBAND BALANCED STEADY STATE FREE PRECESSION FUNCTIONAL MRI OF THE RETINA

MRI can non-invasively image functional hemodynamic responses without depth limitation. Blood oxygen level dependent (BOLD) fMRI, based on the susceptibility effects of hemoglobin in blood, is the most commonly used MRI technique to study function (160). Most BOLD fMRI studies prefer echo planar imaging (EPI) over conventional gradient-echo or spin-echo sequences because EPI allows rapid, real-time image acquisition. However, EPI is vulnerable to susceptibility artifacts such as geometric distortion and signal dropout due to magnetic inhomogeneity. Standard gradient echo sequences have been used for BOLD fMRI, but are much slower than EPI and have lower SNR per unit time, making them impractical for retinal imaging.

MRI of the retina is particularly prone to these artifacts because the region around the eye is very inhomogeneous and is at an air-tissue interface. A few functional MRI studies of the retina have been previously reported. BOLD fMRI of the retina using EPI has detected changes associated with physiologic stimulations (9) and visual stimulation (98,99). Perturbations of BOLD fMRI to physiological challenges in rat retinas with retinal degeneration have also been reported (9).

Balanced steady state free precession (bSSFP) sequences provide fast acquisition, in contrast to conventional MRI sequences, have high SNR, and do not have geometric distortion or signal dropout artifacts associated with EPI. The bSSFP signal is, however, a highly sensitive function to off-resonance frequency shifts, producing passbands and transition bands (Figure 4.1) (161,162). The passband has high signal while the transition band has low signal (except at small flip angles where this contrast is reversed) (162). Magnetic inhomogeneity across an object will result in dark bands in some regions of images obtained with bSSFP. The passbands and transition bands in an image can be shifted by cycling the phase of the radiofrequency (RF) pulse.

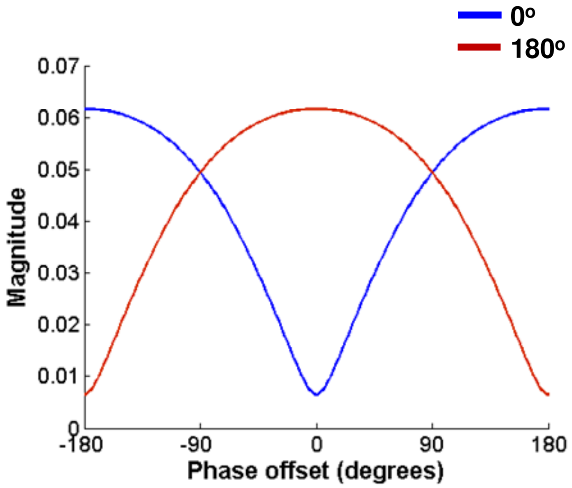

Figure 4.1: Simulation of the magnitude of the bSSFP signal as a function of resonance phase offset during TR. Parameters of the simulation include T_1 = 2.0 s, T_2 = 43 ms, flip angle = 30°, TE = 3.5 ms, and TR = 7.0 ms. Two curves are plotted for RF phase cycling with 0° or 180°.

bSSFP fMRI was only recently demonstrated, initially making use of the transition bands where the signal is very sensitive to off-resonance frequency shifts, such as those caused by deoxyhemoglobin (163,164). Passband bSSFP fMRI was later demonstrated as well, in which imaging is done within the wider and more stable passband region (161,165). Passband bSSFP fMRI has been shown to be useful in human brain imaging, particularly in regions of large magnetic susceptibility such as the prefrontal cortex where EPI has severe artifacts (166).

The features of bSSFP make it an attractive sequence for fMRI of the retina. In this study, the feasibility of high spatiotemporal resolution, passband bSSFP fMRI to resolve layer-specific changes in the mouse retina and choroid was explored. As a demonstration of proof of concept, hypoxic challenge was used to modulate BOLD signals. bSSFP fMRI of the eye at 45x45x500 μm^3 was free of susceptibility related artifacts and provided high-resolution, layer-specific images sensitive to blood oxygenation changes. This approach provides high spatiotemporal resolution without susceptibility artifacts for functional of imaging the retina and choroid.

4.1 Methods

Animal preparation: Experiments were performed on male C57BL/6 mice (8-16 weeks old, *n* = 6). Animals were placed in a holder with a circulating warm water pad and nose cone to provide anesthesia and premixed gases. Imaging was performed under 1.1% isoflurane and spontaneous breathing conditions. Mice were provided 30% O_2 in nitrogen as baseline conditions. Hypoxic challenge was performed by switching the provided gas mixture to 10% O_2 in nitrogen. Respiration rate, heart rate, oxygen saturation, and rectal temperature were monitored. Temperature was maintained at 37 ± 0.5° C. Mice were prepared in a lit room before being transferred to the MRI room, in which lights were turned off. Lighting conditions were not changed during the duration of imaging.

MRI methods: MRI studies were performed on a 7 Tesla, 30 cm magnet and a 150 G/cm BGA6S gradient insert (Bruker, Billerica, MA). For imaging, a small circular surface eye coil (diameter = 6 mm) was placed over the left eye. Images were acquired using bSSFP in a coronal orientation with a single slice passing through the retina near the optic nerve head, with the slice angled perpendicular to the retina. Imaging parameters were field of view = 5x5 mm^2, matrix = 112x112 (45x45 μm^2), one 0.5 mm thick slice, and 3.67/7.34 ms TE/TR. Data were oversampled by 2x in both frequency and phase encode directions.

FASTMAP shimming was used to reduce banding, and the RF phase cycling was adjusted to move bands away from the retina. Alternatively, bSSFP images were acquired with 4 alternating RF phase cycling angles (0, 90, 180, and 270^o) and combined to remove banding from the image (n = 1). Hypoxic challenge involved imaging 4.5 min during baseline and 4.5 min during hypoxia. Hypoxic challenge was repeated twice in all animals with 10 min rests between trials.

Gradient-echo EPI images under 30% O_2 were obtained with the same slice position and resolution for comparison to bSSFP images. Parameters for EPI images were field of view = 6x6 mm^2, matrix = 134x134 (45x45 μm^2), one 0.5 mm slice, BW = 333 kHz, either 1 or 2 segments, and TE/TR = 12.0/2000 ms.

Data analysis: Image processing and analysis was done using codes written in Matlab (Math-Works, Natick, MA), STIMULATE software (University of Minnesota), and Statistical Parametric Mapping (SPM5) software. Images were zero-padded to 128x128 (nominal resolution of 39x39 μm^2) before subsequent processing. All images from each scan were acquired as time series and aligned using the spatial realignment function in SPM5. bSSFP images acquired with 4 phase cycling angles were combined by averaging 3 of the 4 highest image intensities pixel-by-pixel before motion correction.

Image intensity profiles across the retinal thickness were obtained from the anatomical images by radially projecting lines perpendicular to the retina (Figure 4.2 A) with profiles obtained at 8x spatial interpolation (9). Percent-change between baseline and hypoxia was calculated for each profile, and all profiles were averaged along the length of the retina to provide an average %-change profile for the retina. Peak %-change values were determined from the average %-change profile for each animal.

STIMULATE was used for display and calculation of %-change maps of the final motion-corrected images. For the %-change maps, a 95 or 99% confidence interval was used with a %-change threshold between about -5% to -100% and a cluster size of at least 20 contiguous pixels. The %-change map was masked to remove signal decreases in extra-ocular tissues and strong fluctuations in the anterior portion of the eye around the transition bands.

Group-average data were tabulated and expressed as mean ± SD. Statistical analysis with either one-sample t-tests comparing to zero mean or paired t-tests were used, with $p < 0.05$ indicating statistical significance.

4.2 Profile Realignment and Motion Correction

Movement of the eye due to the animal is often non-uniform across the eye and the retina. Thus, global rigid-body motion correction of the entire image of the eye cannot optimally correct motion in all parts of the eye. Further, motion of anterior parts of the eye and extra-ocular tissue can occur separately of the motion that occurs in the retina. Since only the retina is of interest, motion correction performed on the extracted, linearized retina should work better than global correction of the entire eye. As such, the motion correction done by SPM5, which corrected for translation and rotation, effectively removed any large motion, but smaller subtle motion of the retina could remain uncorrected.

After obtaining profiles across the retina from the anatomical images (Figure 4.2 A), further motion correction was performed on the extracted profiles in Matlab. This was done by correcting for 1 dimensional translation in the direction perpendicular to the retina (Figure 4.2 B-C). This realignment was first done on the entire group of profiles together. This was followed by realignment applied to smaller blocks of profiles (usually blocks of 5-10 profiles) to correct for non-uniform movement across the retina which occurred during some experiments. After profile realignment, the motion-corrected anatomical profiles were projected back into the anatomical images (Figure 4.2 D-E) for image display and calculation of %-change maps in STIMULATE.

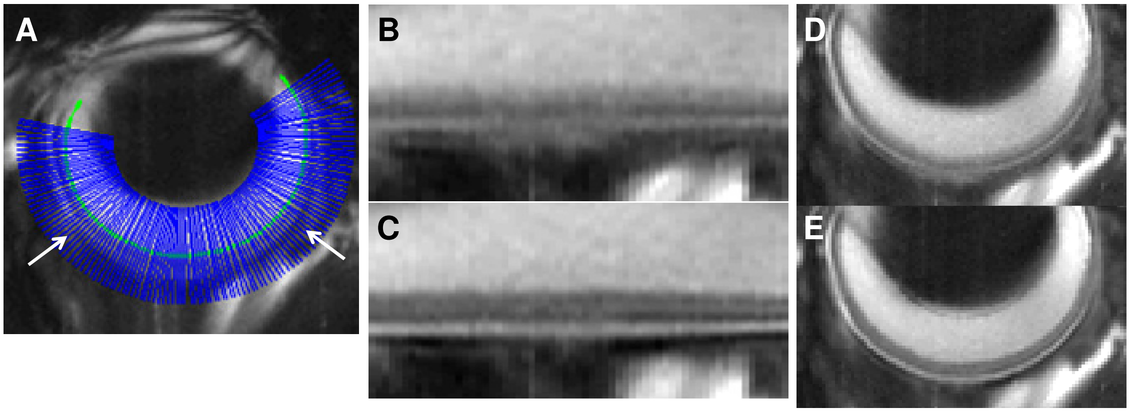

Figure 4.2: (A) bSSFP image showing radially projected profiles (blue lines) perpendicular to the inner edge of the retina (green line). The white arrows indicate the region selected for profile analysis. (B) The linearized retina from the collection of profiles shown in A. (C) The linearzied retina after motion correction applied to the profiles. (D) The original image with blurring due to motion. (E) The image after projecting the motion corrected profiles back into the original image. All images are time-series averages.

In isoflurane anesthetized mice, the motion of the eye most commonly occurring in the MR images was a small jittering or a slow drift of the eye oriented in and out of the eye socket. This type of motion could be corrected very effectively with the profile realignment. Although it rarely occurred, rotation of the eye within the socket, either through-plane or within-plane, would not be effectively corrected by this profile realignment. Finally, severe motion, including large twitches or deformations of the eye, which is also quite rare, would be unlikely to be accurately corrected through any means.

4.3 Results

Physiological parameters of the mice under 30% and 10% O_2 are summarized in Table 4.1. Respiration rate and heart rate were significantly increased under 10% O_2 compared to 30% O_2, while arterial O_2 saturation was significantly lower.

Table 4.1: Physiological parameters of mice under 30% and 10% O_2 (mean ± SD, n = 6) $^*p < 0.01$ compared to 30% O_2

	Respiration Rate (breaths/min)	**Heart Rate** (beats/min)	**Arterial O_2 Saturation** (%)
30% O_2	91 ± 11	371 ± 29	97 ± 1
10% O_2	106 ± 11*	453 ± 65*	68 ± 6*

EPI and bSSFP images of the same eye at 45x45x500 μm^3 are shown in Figure 4.3. The EPI images (Figure 4.3 A, 1 segment; Figure 4.3 B, 2 segments) show distortion in the retina as well as the rest of the eye. One to three distinguishable retinal layers were usually detected in EPI with non-uniform structure and thickness along the retina. In contrast, bSSFP (Figure 4.3 C) produced images without obvious distortion. Four distinguishable dark-bright-dark-bright retinal and choroidal layers were detected in the bSSFP image with uniform structure along the retina.

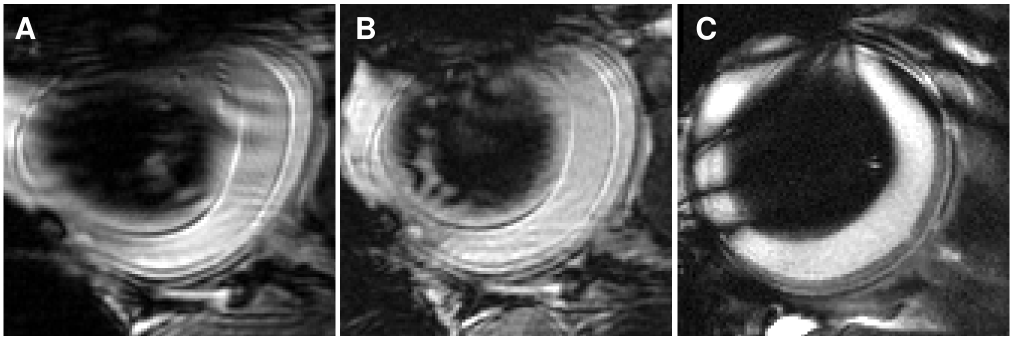

Figure 4.3: EPI images at 45x45x500 μm^3, demonstrating the geometric distortion and other artifacts in the eye acquired with (A) 1 segment or (B) 2 segments. Phase encoding orientation is left-right. (C) bSSFP image (45x45x500 μm^3) from the same animal acquired during baseline conditions showing clear retinal layers without distortion.

Figure 4.4 A shows a representative %-change map associated with hypoxic challenge from a single mouse using bSSFP. Hypoxia decreased the signal in the retina, with a stronger response in the choroidal vascular layer than the retinal vascular layer. Anatomy profiles during baseline and hypoxia (Figure 4.4 B) show four alternating dark-bright-dark-bright layers. Figure 4.4 C shows the corresponding %-change profile due to hypoxia. Two well resolved layers were detected in the %-change maps and profiles that showed signal reductions. These layers were assigned to be the retinal and the choroidal vascular layer. The middle layer in between these two vascular layers showed no significant change and was assigned as the avascular photoreceptor layers (outer nuclear layer and inner and outer segments).

The group-averaged %-changes were -11.6 ± 2.4 % in the inner (retinal) layer ($p < 1E-4$), -1.6 ± 1.4 % in the middle (avascular) layer ($p < 0.05$), and -25.9 ± 6.4 % in the outer (choroid) layer ($p < 1E-3$) (mean ± SD, $n = 6$, one-sample t-test comparing the sample mean to zero). The %-changes in the middle layer were statistically different from that of the inner ($p < 1E-3$) and outer layer ($p < 1E-3$) (paired t-test). The %-changes of the inner and outer layer were also statistically different ($p < 0.01$) (paired t-test).

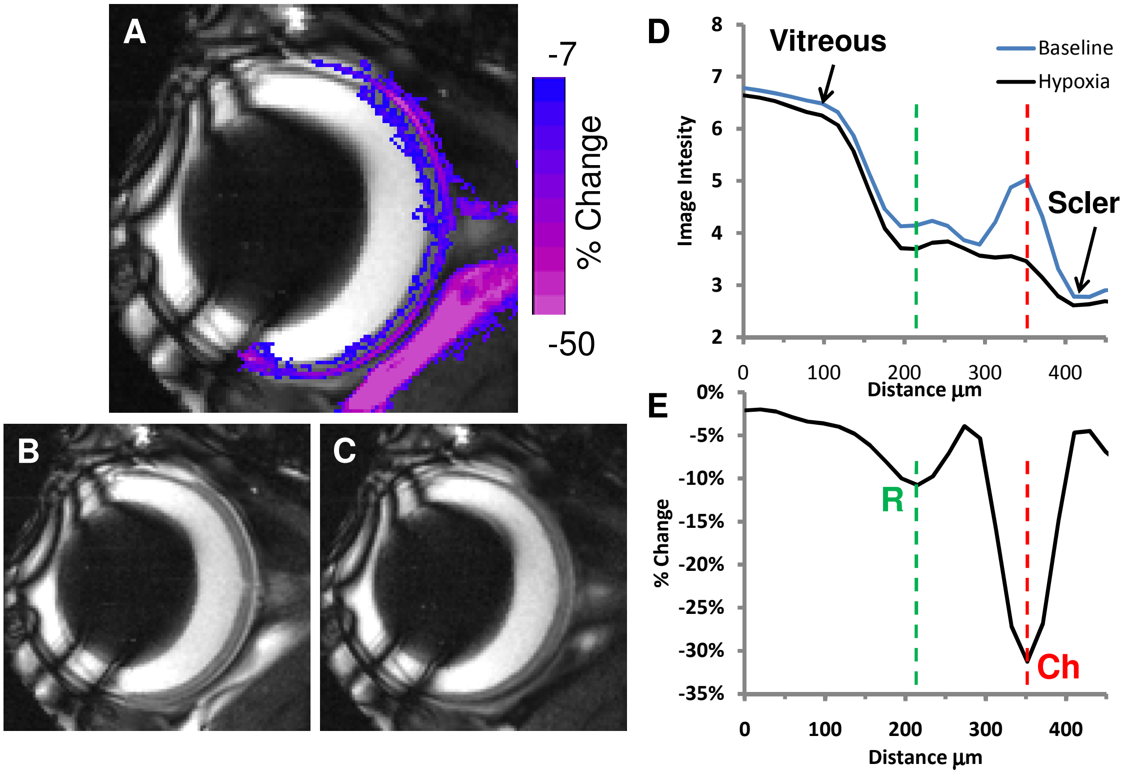

Figure 4.4: (A) Percent-change map in response to hypoxia from a single mouse at 45x45x500 μm^3 overlaid on the bSSFP image. The bSSFP images during (B) baseline and (C) hypoxia. (D) The corresponding anatomical profiles (arbitrary units) of the retina during baseline and hypoxia. (E) The %-change profile due to hypoxia. The red dashed lines indicate the location of peak choroidal vessels (Ch) change and green dashed lines indicate peak retinal vessels (R) change.

A potentially major problem with bSSFP is banding artifacts. The transition bands can be moved away from the region of interest with RF phase cycling. Alternatively, images obtained using multiple RF phase cycling angles can be combined to remove banding artifacts. Figure 4.5 demonstrates that images acquired with 4 RF phase cycling angles can be used to effectively remove all dark transition bands from the bSSFP image of the eye, while maintaining sensitivity to functional changes.

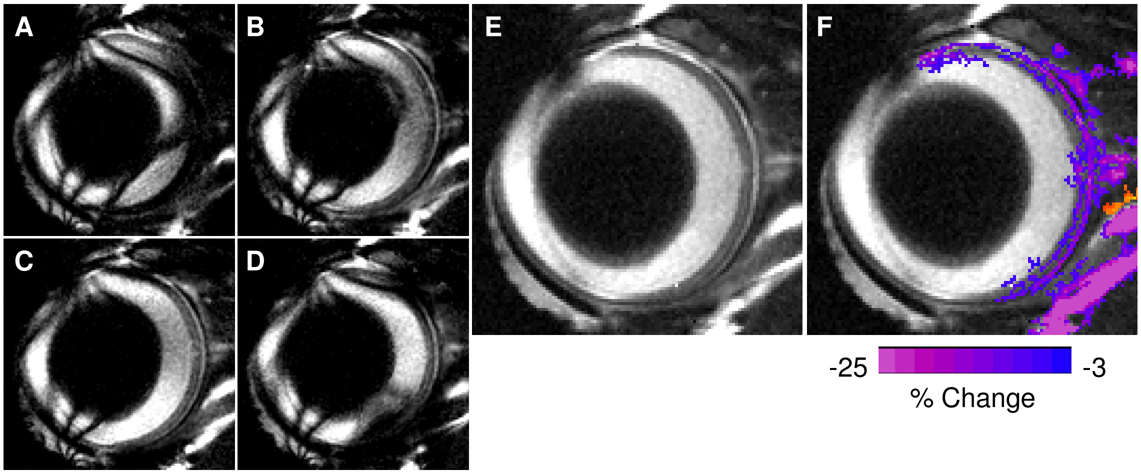

Figure 4.5: (A-D) bSSFP images of the eye with RF phase cycling of 0, 90, 180, and 270°. (E) The four images are combined by averaging the 3 of the 4 highest intensities pixel-by-pixel to remove banding. (F) The %-change map in response to hypoxia overlaid on the bSSFP image with banding removed.

4.4 Discussion

This study demonstrates for the first time the feasibility of applying passband bSSFP fMRI to the retina without magnetic susceptibility-induced signal drop out and geometric distortion. In the bSSFP images of the eye, the retina had clearly defined structure and layers, unlike EPI, allowing for clear definition of both functional and anatomical layers of the retina and choroid. The temporal resolution and SNR per unit time of bSSFP should be comparable to EPI.

Movement: From movies of MRI time-series images, eye movement in isoflurane-anesthetized mice was considerably less than in rats, so paralytics were not used (9,139). The profile realignment discussed in Section 4.2 was effective at correcting small movements which still occurred in some scans. The use of paralytics would likely provide almost no motion and thus better image results, particularly for fMRI. However, successfully recovering rats and mice from paralysis and mechanical ventilation is difficult, so most studies with paralytics are terminal. Additionally, paralytics and anesthesia generally could not be used in human studies, so effective means of correcting motion of the retina is essential.

fMRI of the retina: The eye is an area with large magnetic field inhomogeneity, which results in substantial artifacts in EPI images. bSSFP images were free from these artifacts, although the banding present in bSSFP MRI could be problematic. Banding occurs mostly in regions with large magnetic inhomogeneity, like signal drop out and image distortion artifacts in EPI, so bSSFP imaging of the eye could be prone to severe banding. With FASTMAP shimming using first-order gradients with a small voxel placed within the eye and adjustment of RF phase cycling angle in each animal, the banding could consistently be moved away from the retina. Additionally, strong imaging gradients are necessary to allow for rapid acquisition (short TR to minimize banding) while maintaining the small FOV needed for high-resolution, laminar imaging of the retina. Meanwhile, geometric distortion and other artifacts were still present in EPI even with FASTMAP shimming and the strong gradients to minimize readout time. If the banding did pose a problem in the bSSFP images, they could be removed by acquiring and combining images with multiple RF phase cycling angles, although this will decrease temporal resolution and SNR.

Passband bSSFP fMRI of the retina during hypoxia showed negative signal changes, as would be expected of BOLD fMRI. Passband bSSFP fMRI yields contrast similar to T_2 or T_2* BOLD (167), but the sources of the bSSFP fMRI signals have been unclear, with dependence on TR/TE and field strength (161,162,166,167). Nonetheless, the bSSFP parameters that were used showed good sensitivity to oxygenation changes.

A previous MRI study using EPI demonstrated layer-specific BOLD responses to hyperoxia and hypercapnia in the rat retina at lower resolutions, 90x90x1000 μm^3 (9). The BOLD study demonstrated differential response between the inner and outer edges of the retina, likely corresponding to the retinal and choroid vessels, although the retina consisted of only a single anatomical layer. By comparison, layer-specific bSSFP fMRI was obtained at much higher resolution and with 3 clearly separated functional layers, overlaid on 4 anatomical layers.

Response of the retina to hypoxia: The signal decrease due to hypoxia was significantly larger in the choroid (-25.9 ± 6.4 %) than retinal vascular layer (-11.6 ± 2.4 %). One factor contributing to this difference is likely the high basal choroid blood volume compared to the inner retina (23,149,158), since the BOLD response increases with higher basal blood volumes (160,168). Additionally, the choroid vessels have extremely low oxygen extraction fraction compared to the retinal vessels (23,169) which could potentially factor into different BOLD responses between the two layers. It is difficult to predict what effect, if any this would have though, without knowing the oxygen saturation of both vasculatures under normoxic and hypoxic conditions. Finally, as previously described in Chapter 3, under the same experimental conditions and hypoxic challenge, blood flow of the retina and choroid both decrease, with a much larger change in magnitude in the choroid. This could perhaps result in a larger increase in deoxyhemoglobin concentration in the choroid. Although the small response of the outer retina (-1.6 ± 1.4 %) was significant at $p = 0.04$, this change is possibly due to partial volume from the inner retina and choroid due to the relatively low in-plane resolution.

Four alternating dark-bright-dark-bright anatomical layers were present in the bSSFP images. The lamina-specific bSSFP fMRI response could thus be assigned to specific MRI anatomical layers with bSSFP, unlike EPI which lacked clear anatomical layers. The %-change peak of the choroid consistently lined up with the outermost bright layer of the anatomy. The %-change peak of the retinal layer appeared to span the inner dark and bright layer of the anatomy. The dark layer in the middle of the retina is therefore likely the photoreceptors (outer nuclear layer and inner and outer segments), although further work is needed to assign the MRI layers to specific anatomical layers.

A previous BOLD fMRI study using hyperoxia in rats found a stronger signal increase in the choroid than inner retina (1.7 time larger), similar to the hypoxic changes with bSSFP (9). This further supports the interpretation that high choroidal blood volume is an important factor in the BOLD response, since venous choroidal oxygen saturation is similar to arterial blood (23,169). Hyperoxia should therefore only have small changes on the concentration of deoxyhemoglobin in the choroid, but with such large volumes of blood in the choroid, this could still have a large change in the total quantity of deoxyhemoglobin in the choroid.

4.5 Conclusions

Functional MRI of the retina is challenging because the eye is a region with large magnetic inhomogeneity, causing substantial artifacts in EPI sequences usually used for fMRI studies. Passband bSSFP fMRI of the retina yields high spatial and temporal resolution without geometric distortion and signal dropout. Differential responses of the retinal and choroidal vasculature, separated by the avascular region of the outer retina, were detected. This MRI approach is sensitive to blood-oxygenation changes. bSSFP fMRI has the potential to provide layer-specific information about vascular regulation in the normal retina and dysregulation in disease states.

CHAPTER 5

BLOOD FLOW OF THE RETINA IN DIABETIC RETINOPATHY

Diabetic retinopathy (DR) is the leading cause of blindness in most developed countries (170,171). Approximately 40% of adult diabetic patients in the United States have DR (172) and the prevalence rises to 75% among patients with type 1 diabetes (173). Dysfunction of the retinal vasculature is the most prominent feature of diabetic retinopathy, signs of which are used clinically to diagnosis the disease. Vascular changes include thickening of the vascular layers, altered vascular autoregulation, capillary non-perfusion, plasma protein leakage, ischemia, and ultimately proliferative growth of new vessels (174-176). The changes in retinal and choroidal blood flow in diabetic retinopathy are complex and remain unclear, with conflicting reports finding no changes in blood flow in diabetics (2,177), increased blood flow (3,178,179), and decreased blood flow (4).

Since high-resolution ASL MRI had been demonstrated to be capable of imaging quantitative blood flow of the retina and choroid, this technique was applied to a mouse model of diabetes. ASL MRI was utilized to image quantitative, layer-specific retinal blood flow (rBF) and choroidal blood flow (chBF) in the $Ins2^{Akita}$ (Akita) mouse model of diabetic retinopathy. Additionally, visual function was assessed in the mice using psychophysical tests to quantify deficits in visual acuity and contrast sensitivity in diabetic mice.

5.1 Diabetic Retinopathy

Hyperglycemia and possibly other risk factors associated with diabetes, such as hypertension, induce various physiological changes which can damage the microvasculature (180). Factors involved in this damage include oxidative stress, inflammation, and increased advanced glycation end-products, which result in ischemia and hypoxia, increased permeability of vessels, and microaneurysms (180,181). This can eventually lead to neovascularization and macular edema resulting in severely impaired vision (180,181). Diabetes may also directly affect the retinal neurons in addition to the retinal vasculature, causing damage to the retina preceding clinical diagnosis (182). Possible mechanisms for neuronal damage could be directly related to hyperglycemia or reduced activity of retinal insulin receptors (182,183).

The most commonly studied animal models of DR have diabetes induced using toxins such as streptozotocin (STZ) or alloxan to kill pancreatic β-cells, causing hypoinsulemia and hyperglycemia (184,185). Although STZ rats are a common model, the use of STZ in mice can be problematic, due to large strain-dependent variations in the effectiveness of STZ (185). There are a number of genetic models of type 1 and type 2 diabetes in mice (186-188) and rats (189,190) that provide an alternative to the toxin induced diabetes.

While it is important to monitor progressive visual deficits that occur in human patients with diabetes, visual testing has not been commonly reported in animal models of DR, aside from electroretinograms (ERG). In diabetic patients, visual deficits in contrast sensitivity, visual acuity, color vision, and ERG precede the clinical signs of vascular lesions (191-195). Visual function assessed by ERG in animal models indicates disruptions in the inner retina while the outer retina remains normal (196,197). The oscillatory potentials, possibly originating from the amacrine cells of the inner plexiform layer (198), are sensitive to early DR changes, while the most commonly measured a and b waves - originating from the photoreceptors and inner retina, respectively - remain normal (197).Visual acuity and contrast sensitivity can be studied in animals by monitoring the optomotor response to rotating visual stimulation which induces reflexive turning of the head and neck (199-201).

5.1.1 Retinal and Choroidal Blood Flow in Diabetes

Diabetes causes damage to the microvasculature, and is of particular concern in the retina. Measurements of rBF and chBF in DR have yielded conflicting results. Reports show decreased BF, increased BF, or no changes in BF due to diabetes. Possible reasons for this inconsistency include i) type or model of diabetes (type 1 or 2 diabetes, toxin induced or genetic animal models, etc.), ii) duration and stage of retinopathy (diabetes with no clinical signs of retinopathy, early stage retinopathy, proliferative retinopathy, macular edema, etc.), iii) treatment (insulin to maintain normal blood glucose levels), iv) techniques for measuring blood flow (laser Doppler velocimetry, laser Doppler flowmetry, fluorescein angiography), v) the location of measurement (arteries, capillaries, venules, tissue, etc.), and vi) the type of parameters measured (velocity or circulation time of exogenous dyes, erythrocyte velocity or flow rates, blood volume, vessel size, etc.).

In human patients, BF of the retina in diabetes has been studied mostly using laser Doppler velocimetry and fluorescein angiography and is usually reported to either increase or not change in diabetes. A spectrum of diabetic patients, ranging from no retinopathy to severe retinopathy, had no changes in blood velocity, BF, and arteriolar diameter of the retinal vasculature (2,177). Other studies report that total BF to the retina is increased in diabetic patients with no or mild retinopathy (3,178,179), while blood velocity in retinal veins was unchanged (178,179). However, decreased blood velocity in retinal veins and arteries of diabetic patients is also reported (4). In the choroid, blood volume and BF were lower in proliferative diabetic retinopathy, while blood velocity is unchanged (106).

Most often, rBF is reported to be lower in rodent models of diabetes. In non-obese diabetic mice, BF in retinal arteries of diabetic mice was lower (187). In STZ mice, retinal blood velocity and vessel diameter were reduced compared to controls (202). In STZ rats, retinal blood velocity was lower as well (30). In another study with STZ rats, blood flow and vessel diameter of retinal arteries were lower while blood velocity in the arteries was unchanged (203). In an alloxan induced model of diabetes in dogs, rBF was lower in diabetic animals (147). chBF may also be altered in animal models of diabetes. In the choriocapillaris, red blood cell velocity and flux were lower in STZ rats, while vessel diameter is not changed (204). Increased BF has also been reported in rodent models. In the genetic db/db mouse model of type 2 diabetes, red blood cell velocity was increased in the retinal capillaries of diabetic mice (188). Using the microsphere and hydrogen clearance methods, rBF and BF of the combined choroid/sclera were increased in STZ rats (205,206).

5.1.2 The Ins2Akita Mouse Model of Diabetes

The Akita mouse is a genetic model of Type 1 diabetes that develops many retinal complications (207-209). The Akita mouse has a point mutation in the insulin 2 gene which leads to misfolding of the insulin 2 protein. Mice heterozygous for this mutation have severely reduced levels of insulin, despite the presence of a remaining wild-type insulin 2 allele and two alleles for insulin 1. The misfolded protein leads to its accumulation in pancreatic β cells and disruption of transport mechanisms within the cells (186,210). This results in disruption and death of the β cells causing hypoinsulemia, hyperglycemia, and diabetes. Male mice heterozygous for the $Ins2^{Akita}$ mutation consistently develop hyperglycemia (186).

Akita mice become hyperglycemic at about 4 weeks old (207). They begin to show signs of diabetic retinopathy by 1-3 months after onset of hyperglycemia (207,208). These mice have neuronal damage in the retina as indicated by increased apoptosis in the retina, reduced retinal ganglion cell and amacrine cell number, and eventual thinning of the inner plexiform and inner nuclear layers. Some vascular abnormalities also occur in the Akita mouse retina, including increased retinal vascular permeability and acellular capillaries (207,208).

5.2 Methods

Animal preparation: Experiments were performed on male mice heterozygous for the $Ins2^{Akita}$ mutation on a C57BL/6J background (Jackson Laboratory, Bar Harbor, Maine). Wild type littermates lacking the $Ins2^{Akita}$ mutation were used for controls. To confirm hyperglycemia, blood glucose was measured using a blood glucose meter (AlphaTrak; Abbott Labs; Abbott Park, IL) at 4.5 weeks of age. Blood glucose > 250 mg/dl was considered to be hyperglycemic.

MRI was performed on mice at 30-37 weeks of age (n = 9 Akita, n = 8 wild type). Optomotor responses of awake, freely moving animals were determined at 29-32 weeks of age (n = 10 Akita, n = 8 wild type). MRI and visual tests were performed on the same mice except visual tests were performed on 1 Akita mouse and 1 wild type mouse without MRI, and MRI was performed on 1 wild type mouse without visual tests. The visual acuity measurement from 1 wild type mouse was excluded from analysis due to an unreasonable value being recorded.

MRI methods: For MRI, animals were placed into a head holder with ear and tooth bars. Imaging was performed under 1.1-1.4% isoflurane, 30% oxygen with balance nitrogen, and spontaneous breathing conditions. A circulating warm water pad was used to maintain rectal temperature at 37 ± 0.5° C. Mice were prepared in a lit room before being transferred to the MRI room, in which lights were turned off. Lighting conditions were not changed during the duration of imaging. Breath rate, heart rate, and oxygen saturation were monitored and maintained (MouseOx, STARR Life Science Corp., Oakmont, PA).

MRI studies were performed on a 7 Tesla, 30 cm horizontal magnet and a 150 G/cm BGA6S gradient insert (Bruker, Billerica, Massachusetts). For imaging, a small circular surface eye coil with active decoupling (diameter = 6 mm) was placed over the left eye. A circular labeling coil (diameter = 8 mm) was placed at the heart position for a cardiac spin labeling technique as previously described (114). The two coils were separated by 2.3 cm from center to center.

BF MRI was acquired using two-coil continuous ASL with an echo planar imaging (EPI) sequence. Paired images, one with and one without labeling, were acquired in an interleaved fashion. ASL employed a 2.6 s square radio frequency pulse to the labeling coil in the presence of a 2.0 G/cm gradient along the flow direction with a post label delay of 350 ms. The sign of the frequency offset was switched for non-labeled images. Images were acquired in a coronal orientation with a single slice passing through the optic nerve head, with the slice angled perpendicular to the retina. Two-segment, gradient-echo EPI was used with field of view = 6.0x6.0 mm^2, matrix = 144x144 (42x42 μm^2 resolution), a single 0.4 mm slice, TR = 3.0 s per segment, and TE = 12.6 ms. For each scan, 100 pairs of images were acquired in time-series with a total acquisition time of 20 min.

Visual acuity and contrast sensitivity measurements: Visual acuity and contrast sensitivity were assessed in mice by measuring the optomotor response to drifting gratings (199-201) using the OptoMotry system (Cerebral Mechanics, Inc., Lethbridge, Canada). The mouse was placed on a platform in the center of a chamber made of computer monitors. A virtual cylinder of sinusoidal gratings rotating at 12 degrees/sec was displayed on the monitors. The mouse is watched via an overhead video camera to determine if the head turns in response to the rotating gratings. A cursor placed at the animal's head is used to center the virtual cylinder at the animal's head. Both eyes can be tested since the left and right eyes are most sensitive to clockwise and counterclockwise rotations, respectively. Visual function was assessed in the left eyes of the mice (same eye as MRI).

To test for acuity, 100% contrast was used while the spatial frequency of the gratings (in cycles/degree (cpd)) was varied using a stair-step protocol with a minimum step size of 0.003 cpd. A threshold was reported by the OptoMotry software as the contrast at which a head turn in response to the stimulus was observed in 70% of trials. Contrast sensitivity was assessed in a similar way at two spatial frequencies, 0.103 and

0.064 cpd, and with a minimum step size of 0.1%. These values encompass the spatial frequency that gives the peak sensitivity in C57BL6 mice (199). Contrast was calculated as (max-min)/(max+min), where max and min are the maximum and minimum values of the sinusoidal gratings. The contrast threshold was the contrast level where responses were observed in 70% of trials.

MRI image analysis: Image analysis was done using codes written in Matlab (Math-Works, Natick, MA), STIMULATE software (University of Minnesota), and Statistical Parametric Mapping 5 (SPM5) software. Images were zero-padded to 256x256 (nominal resolution of 23x23 μm^2) before subsequent processing. All images from each scan were acquired as time series, aligned using the spatial realignment function in SPM5 and averaged off line.

Blood flow images in units of (ml blood)/(g tissue)/min were calculated pixel-by-pixel using Eq. 1.1. λ, the water tissue-blood partition coefficient, was taken to be 0.9, the same as the brain (64). The retina and choroid T_1 at 7 T was taken to be 1.8 s which is similar to brain T_1 (68). The labeling efficiency α was previously measured to be 0.7 (see Chapter 2) (114).

BF intensity profiles across the retinal thickness were obtained from BF images by radially projecting lines perpendicular to the retina with profiles obtained at 4x spatial interpolation (9,139). Further motion correction was performed on the extracted profiles in Matlab (see Section 4.2). BF profiles were averaged along the length of the retina, excluding the optic nerve head. Measurements of peak values and layer thicknesses – defined as half-height width of BF peaks – were determined from the average BF profiles for each animal. The average length of the retina used for profile analysis was 2516 ± 45 μm in the Akita mice (n = 9) and 2543 ± 111 μm in wild type mice (n = 8, mean ± standard deviation (SD)).

Data analysis: Group-average data were tabulated and expressed as mean ± SD. Two-sided t-tests with $p < 0.05$ indicating statistical significance were used to compare means of rBF, chBF, spatial frequency, and contrast sensitivity. Thickness measurements from MRI were compared between Akita and wild type mice using the Wilcoxon rank-sum test. Correlation and linear regression were used on values of rBF, chBF, spatial frequency, and contrast sensitivity to analyze possible relations between the different measurements.

5.3 Results

Physiological parameters measured from the mice are summarized in Table 5.1. Mice with blood glucose > 250 dg/ml were considered to be hyperglycemic. At 5 weeks of age the mice with the Ins2^{Akita} mutation already had raised blood glucose. The Akita mice also had significantly lower body mass compared to controls at the time of MRI measurements. The wild type mice were imaged under ~1.4 % isoflurane, while the Akita mice were imaged under ~1.1 % to maintain their physiology close to that of the wild type mice. The Akita mice required less isoflurane likely due to diabetes and their smaller body mass. Despite this the respiration rate of the Akita mice was still slightly but significantly lower than controls ($p = 0.04$). Heart rate and oxygen saturation were not different between the wild type and Akita mice.

With a resolution of 42x42x400 μm^3, two distinct BF layers in the retina were resolved, separated by a region of low BF contrast (Figure 5.1 A). The outer BF layer, which corresponds to the choroid, had very high BF. The inner BF layer, which corresponds to the retinal vessels, had substantially lower BF than the choroid. The middle layer with little to no BF contrast corresponds to the avascular region, made up of the outer nuclear layer and the outer and inner photoreceptor segments.

Table 5.1: Physiological parameters in Akita and wild type mice (mean ± SD, WT - wild type) *p < 1E-6, **p < 0.05 between wild type and Akita

	WT	Akita	n (WT)	n (Akita)
Blood Glucose (mg/dl, at 4.5 wks) *	193 ± 36	461 ± 58	9	9
Age (wks, at time of MRI)	32 ± 2.1	33 ± 2.4	8	9
Age (wks, at time of visual tests)	29 ± 0.2	30 ± 1.7	8	10
Weight (g, at time of MRI) *	32 ± 2.1	24 ± 1.4	8	9
Respiration Rate (breaths/min) **	109 ± 7.4	99 ± 10.2	8	9
Heart Rate (beats/min)	435 ± 47	407 ± 38	8	9
Oxygen Saturation (%)	98.8 ± 0.5	98.3 ± 0.5	8	9

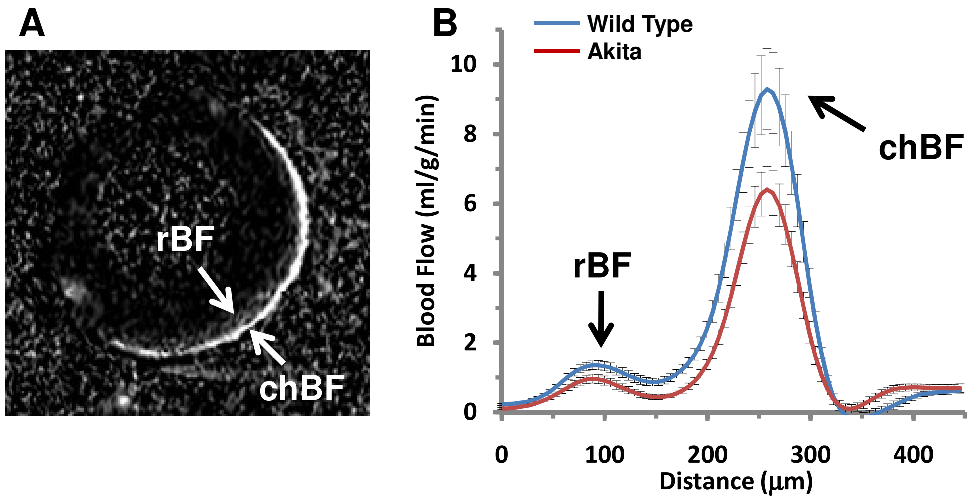

Figure 5.1: (A) Blood flow image from a wild type mouse at 42x42x400 μm^3 showing the retinal and choroidal blood flow. Intensity is scaled from 0 to 7 ml/g/min. (B) Group averaged blood flow profiles from Akita (n = 9) and wild type mice (n = 8). Two distinct peaks are present, indicating the retinal (rBF) and choroidal (chBF) blood-flow peaks. Error bars represent SEM.

Group averaged BF profiles from Akita and wild type mice are shown in Figure 5.1 B. Overall, BF was lower in the Akita retina compared to wild type. BF values of the retina and choroid in Akita and wild type mice are summarized in Table 5.2 and Figure 5.2. rBF was lower by 0.45 ± 0.48 ml/g/min or 33% in Akita mice compared to wild types ($p = 0.018$, n = 9 Akita and 8 wild type). chBF was lower by 2.96 ± 3.94 ml/g/min or 32% in Akita mice compared to wild type ($p = 0.054$, n = 9 Akita and 8 wild type).

Table 5.2: Blood flow (n = 8 wild type, n = 9 Akita) and optomotry (n = 8 wild type, n = 10 Akita) results in wild type and Akita mice (mean ± SD)
* $p < 0.05$, ** $p < 0.01$ between wild type and Akita

	Wild Type	Akita	Magnitude Difference	Percent Difference
Retinal BF (ml/g/min)*	1.4 ± 0.4	0.9 ± 0.3	-0.5 ± 0.5	-33
Choroidal BF (ml/g/min)	9.4 ± 3.4	6.4 ± 2.0	-3.0 ± 3.9	-32
Acuity (cycles/degree)**	0.42 ± 0.04	0.33 ± 0.06	-0.088 ± 0.070	-21
Contrast Threshold, 0.103 (%)**	2.2 ± 0.7	6.7 ± 4.4	4.6 ± 4.5	213
Contrast Threshold, 0.064 (%)*	3.1 ± 1.1	7.1 ± 4.6	4.0 ± 4.7	132

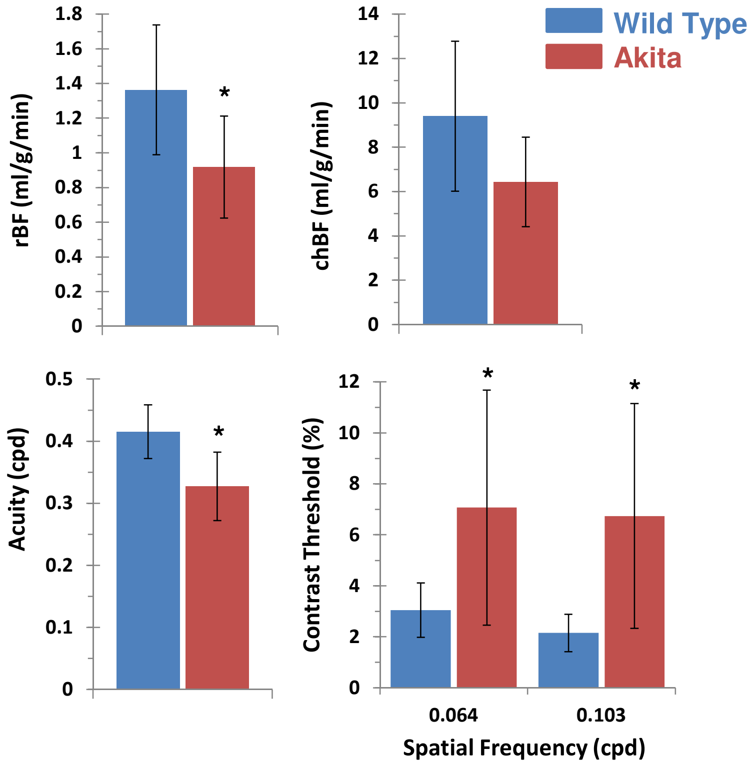

Figure 5.2: (A) Retinal blood flow and (B) choroidal blood flow in wild type (n = 8) and Akita (n = 9) mice. (C) Visual acuity and (D) contrast sensitivity in wild type (n = 8) and Akita (n = 10) mice (mean ± SD). *$p < 0.05$ compared to wild type mice.

Based on the BF profiles, thicknesses of the retinal and choroid vascular layers and the avascular layer in between were estimated (Table 5.3). The thicknesses of the neural retina and choroid were about 165 μm and 70 μm, respectively. There were no significant differences in thicknesses between wild type and Akita mice ($p > 0.05$).

Table 5.3: Thicknesses of retinal and choroidal vascular layers and the avascular layer (μm, mean ± SD, n = 8 wild type, n = 9 Akita). Neural Retina is the sum of the Retinal Vascular Layer and Avascular Layer. Retinal-Choroidal Peak Separation is the distance from the BF peak of the Retinal Vascular to the BF peak of the Choroidal Vascular Layer

	Wild Type	**Akita**
Retinal Vascular Layer	62 ± 11	65 ± 13
Avascular Layer	102 ± 8	105 ± 11
Choroidal Vascular Layer	74 ± 3	69 ± 6
Neural Retina	164 ± 16	169 ± 18
Retinal-Choroidal Peak Separation	167 ± 13	170 ± 20

Visual acuity and contrast thresholds are summarized in Table 5.2. The visual acuity measurement of one wild type mouse was excluded from analysis due to an obviously unrealistic reading, which likely came from user error. The visual acuity of Akita mice was significantly worse than wild types, measured as a decrease in the spatial frequency threshold ($p = 0.002$, n = 10 Akita and 7 wild type). The contrast thresholds with grating sizes of 0.064 and 0.103 cpd were both significantly worse in the Akita mice, measured as a larger contrast threshold ($p = 0.023$ and 0.009, respectively). The contrast thresholds with gratings of 0.064 and 0.103 cpd were not significantly different from each other in either the Akita or wild type mice ($p > 0.05$).

Figure 5.3 shows scatter plots and linear fits of rBF, chBF, acuity, contrast threshold at 0.064 cpd, and contrast threshold at 0.103 cpd for the Akita and wild type mice. In general, most of the measures were correlated with each other in the wild type

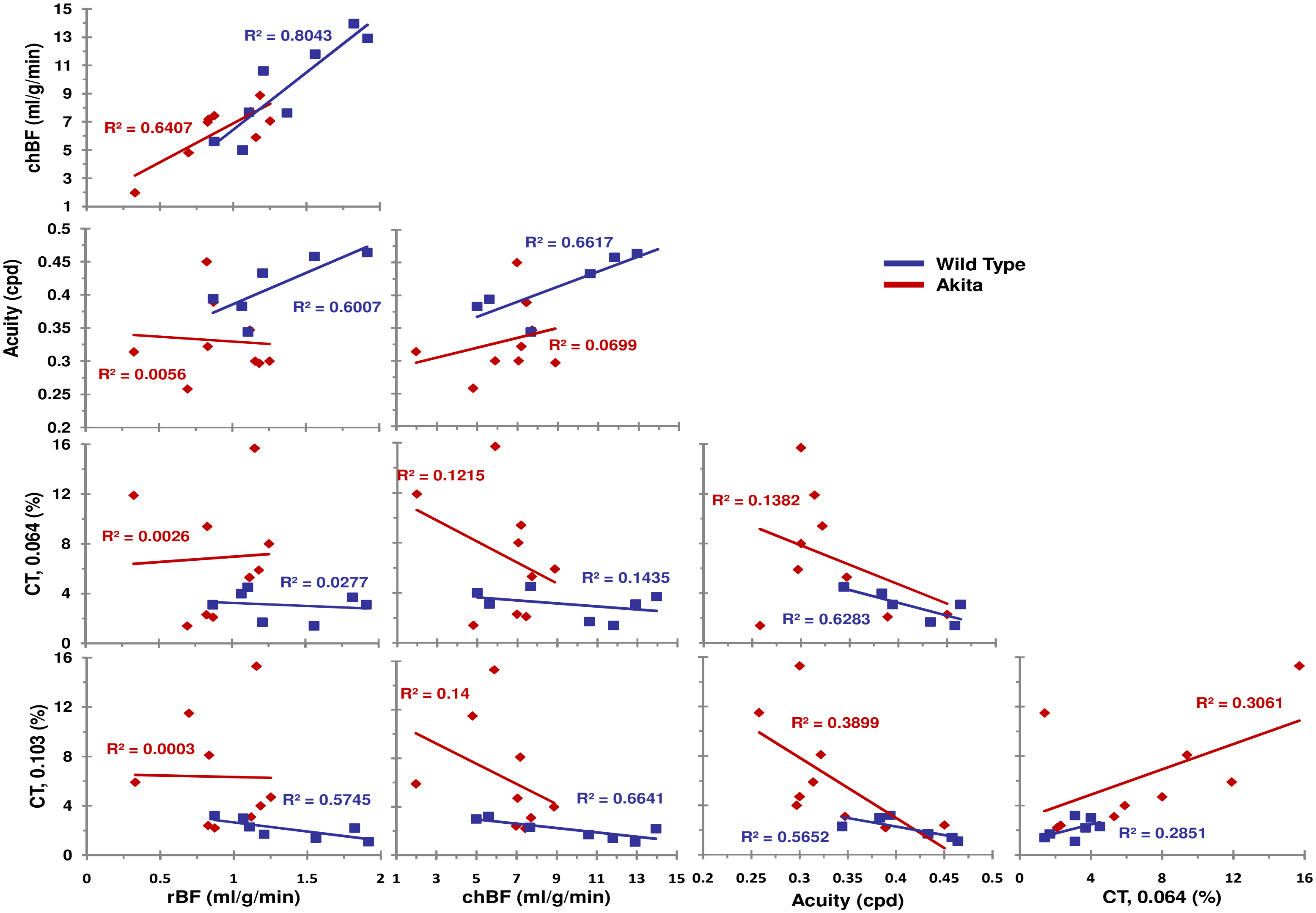

Figure 5.3: Scatter plots of rBF, chBF, visual acuity (acuity), and contrast threshold at 0.064 cpd (CT, 0.064) and 0.103 cpd (CT, 0.103) in wild type (n = 8 for rBF and chBF, 6 for acuity, 7 for both contrast thresholds) and Akita (n = 9 for all) mice. R^2 is shown for each plot.

mice, but not the Akita mice. In the wild type mice, higher BF tended to correlate with better performance in the visual behavior tasks (higher acuity or lower contrast thresholds). The Akita mice appear to have more variability in these measurements than the wild types. In both Akita and wild type mice, rBF and chBF correlated with each other. The 3 measures of vision tended to correlate with each other in both Akita and wild type mice.

5.4 Discussion

MRI detected laminar specific BF differences in the retina of hyperglycemic Akita mice compared to age-matched controls at 7-8 months of age. Retinal BF was lower in the Akita mouse retina compared to age-matched controls. chBF was also lower but not significantly. No significant differences in retinal and choroidal thicknesses were found between control and Akita mice, measured from MRI. The visual acuity and contrast sensitivities to rotating gratings were significantly worse in the hyperglycemic mice compared to wild type controls. In wild type mice, higher BF tended to correlate with better vision, while in Akita mice, BF and vision had little correlation. These findings demonstrate further evidence of diabetic retinopathy in the Akita mouse

Thicknesses: There were no differences in thicknesses of the retina of Akita and wild type mice, as measured from the BF MRI. Histological measurements of thickness have shown thinning of the inner plexiform and inner nuclear layers in Akita mice (by around 5-20 μm) (207). With an actual MRI resolution of 42x42 μm^2, it is unlikely that such subtle changes presumably present in the diabetic retinas would be detected.

Visual function: Visual acuity and contrast sensitivity were worse in the 7-8 month old Akita mice. Visual deficits can occur in human diabetic patients before clinical signs of diabetic retinopathy (191), including deficits in contrast sensitivity (192) and color sensitivity (193). Changes in ERG have also been noted in human DR, particularly in the oscillatory potentials and scotopic threshold (194,195,211) which arise from inner retinal activity. The ERG of STZ rats have similar deficits in the oscillatory potentials and scotopic threshold (196,197). Reports of visual tests in animal models of DR could not be found for comparison to the reduced visual acuity and contrast sensitivity found in Akita mice. Finally, since visual function was assessed with a behavioral test, deficits elsewhere, such as the brain or muscles, could influence the results. As such it is not entirely certain visual deficits in Akita mice arose from the retina.

Blood flow in diabetes: At 7-8 months of age, rBF was significantly lower in the Akita mice. While chBF was also reduced, the change was not significant. These results are consistent with previous studies in other animal models of diabetes, which demonstrated reduced retinal blood flow, blood velocity, and vessel size (30,187,202-204). Decreased measures of rBF has been found in the non-obese diabetic mouse (187), STZ-induced diabetic mice (202), STZ-induced diabetic rats (30,203). However, there are also some reports of increased rBF in rodent models, including the db/db mouse (188) and STZ rat (205,206).

In the choroid, decreased BF has been reported in humans (106). However, in STZ rats, chBF has been reported to both decrease (204) and increase (205) in diabetic animals. Most animal models induce diabetes with the toxins STZ or alloxan, and reported studies of BF in these animals are commonly performed only a few weeks after induction of hyperglycemia (30,187,202-204). As such it is uncertain how relevant these previous studies are to the aged genetic model of diabetes used herein.

Akita mice have neuronal and some vascular signs of diabetic retinopathy mainly localized to the inner retina by 2-3 months of age (207). The oxygen of the outer retina is mainly supplied by the choroidal vasculature, while the oxygen of the inner retina comes from the retinal vasculature (24,157). Thus, the finding of lower rBF is consistent with the previous reports of inner retinal damage in the Akita mice (207).

A possible confounding factor of the BF measurements is the lower isoflurane levels used in the Akita mice (1.1%) compared to wild type mice (1.4%). Isoflurane is a vasodilator (136), and there is some evidence that it can increase BF of the combined retina/choroid (100). However, in STZ diabetic rats, the minimum alveolar concentration of isoflurane and halothane is reduced in diabetics (212,213). Further, diabetic patients have more severe drops in mean arterial blood pressure under isoflurane/nitrous oxide anesthesia compared to non-diabetics with the same anesthesia regimen (214). Since isoflurane causes blood pressure to drop due to vasodilation, this suggests the diabetic patients may have had more extensive vasodilation. Also, the wild type mice were much heavier and appeared to have more body fat, so they may require higher isoflurane levels due to this. Thus it is expected that the diabetic Akita mice would need lower levels of isoflurane to maintain the same depth of anesthesia as normal wild type mice.

Additionally, the respiration rate of the Akita mice was modestly, but significantly, lower during anesthesia. Lower respiration rate would cause hypoxia and hypercapnia which could cause increased BF, although oxygen saturation measurements suggest no differences in oxygenation between the Akita and wild type mice.

Blood flow and visual tests: Comparison of BF measurements and visual tests, suggest that higher BF in the retina / choroid and better visual acuity / contrast sensitivity are correlated in wild type mice. In Akita mice, however, this relationship was disrupted. Despite the fact that BF tended to be lower and vision tended to be worse in Akita mice, these changes were weakly correlated to each other.

Although diabetic retinopathy has been traditionally thought of mostly as a disease of the vasculature, there is evidence that neuronal damage occurs in the retina independent of and possibly prior to vascular abnormality (182). Hyperglycemic Akita mice have been shown to have neuronal damage in the retina by 2-3 months of age (207). It may thus be possible that the vision deficit in the Akita mice is mainly due to direct neuronal damage, independent of damage to the microvasculature and altered BF to the retina. Both hyperglycemia and hypoinsulemia may possibly be damaging to retinal neurons (182,183). Alternatively, if the visual tests were influenced by deficits in the brain or muscles of Akita mice, then the measured visual deficit could be entirely unrelated to rBF and chBF.

5.5 Conclusions

ASL MRI was used to investigate retinal and choroidal BF in the Ins2^{Akita} mouse model of diabetes. In addition, visual function was assessed in the hyperglycemic Akita mice, testing visual acuity and contrast sensitivity. In aged Akita mice, retinal BF was lower and acuity and contrast sensitivity were worse, indicating retinopathy. However, the reduction in BF and worsening of vision did not seem to be correlated in the Akita mice, suggesting these changes may occur through independent mechanisms. Further studies are needed to determine the effects of Akita at earlier time points and to corroborate the unique BF and visual findings in the Akita mouse.

CHAPTER 6

MRI OF RETINAL DEGENERATION

Retinitis pigmentosa is the most common inherited retinal degeneration, affecting 1.5 million people worldwide (215). It consists of a group of retinal dystrophies that cause photoreceptor death and blindness (216). There is some evidence of vascular disruption in the retina (7,10,217). While perturbations of the vasculature and blood flow of the retina and choroid are known to be significant factors in some retinal diseases, such as diabetic retinopathy (1) and glaucoma (5), these factors have not been extensively studied in retinal degeneration.

The cardiac ASL method could non-invasively image blood flow of the retina and choroid, so the method was utilized to study BF changes in retinal degeneration. MRI was utilized to image quantitative, layer-specific retinal blood flow (rBF) and choroidal blood flow (chBF) in the rd10 mouse model of retinal degeneration at different stages of degeneration. Anatomical MRI was also obtained to monitor changes in retinal and choroidal thickness over time and compared to histological measurements.

6.1 Retinal Degeneration and Retinitis Pigmentosa

Retinitis pigmentosa is group of inherited diseases of the retina which causes retinal degeneration and vision loss. It is characterized initially by a progressive loss of photoreceptors, usually affecting the rods first, followed by a secondary loss of cones. Retinitis pigmentosa begins with loss of peripheral vision and impaired night vision due to the loss of rods and progresses to loss of the central visual field and complete blindness (215). In addition to the photoreceptors, other neural and synaptic layers in the retina deteriorate slowly over time (218). A large number of mutations in many different genes which cause retinitis pigmentosa have been described, including the genes for rhodopsin, mertk, and phosphodiesterase β (216,218,219).

The retinal vasculature has been found to atrophy in retinal degeneration (10,220,221), often considered to be a secondary effect of photoreceptor loss. It is has been proposed that extensive loss of the photoreceptors, which have a high metabolic rate, causes hyperoxia in the retina which in turn may attenuate the retinal vasculature (157,222). Further, light exposure can accelerate degeneration (223,224), while reduction of light can slow or possibly reverse degeneration (223). It has been suggested that the effects of light are mediated through retinal oxygenation, since oxygen is increased under light compared to dark conditions (23). However, hyperbaric oxygen therapy preserves vision in retinitis pigmentosa patients, suggesting the retina is hypoxic, leading to increased photoreceptor degeneration (225). Additionally, injection of hematopoietic stem cells into the eye of rd mice prior to degeneration, rescued retinal vasculature from atrophy, reduced degeneration of the outer retina, and preserved some electroretinogram (ERG) response (10). This suggests that vasculature dysfunction may have an important role in early stages of and progression of retinal degeneration.

Although the vasculature is known to be affected retinal degenerations, BF of the retina and choroid has rarely been studied. In humans, diameter, blood velocity, and blood flow in retinal veins were all substantially lower in retinitis pigmentosa patients, as well as total retinal BF (217). In a cat model of retinitis pigmentosa, rBF was compromised while chBF was not significantly affected (7). In human patients the ocular pulse amplitude, used as an indication of chBF, was reduced in later stages of the disease, but not early (226). chBF was also reported to be lower in patients with retinitis pigmentosa as measured by laser Doppler flowmetry (227). A study using MRI to image combined retinal/choroidal BF in the RCS rat model of retinal degeneration, found that the combined BF was lower in the animals with retinal degeneration (8).

The regulation of the retinal and choroidal vasculature may potentially be altered in retinitis pigmentosa as well. A study using BOLD fMRI found attenuated retinal and choroidal responses to hyperoxia and hypercapnia in the RCS rat model of retinal degeneration (9). BF changes of the combined retina/choroid due to hyperoxic and hypercapnic challenges were also attenuated in RCS rats (8). In human patients, however, the retinal vascular response to hyperoxia was not altered (217). These studies suggest that the retinal and choroidal vasculature may play an important role in retinal degeneration.

6.1.1 The rd10 Mouse Model of Retinal Degeneration

The rd10 mouse is an animal model of retinal degeneration (228-230). Retinal degeneration begins in rd10 mice about post natal 16 days and is complete by 60 days (229,230). Degeneration of the outer retina (outer nuclear layer and inner and outer segments) begins first with remodeling of the inner retina occurring later (230). The outer nuclear layer and inner and outer segments eventually completely degenerate by post natal 60 days (229).

rd10 mice have a mutation in the *Pde6b* gene, encoding a subunit of the rod phosphodiesterase (228,229). Similarly, mutations in the gene for the β subunit of the rod phosphodiesterase have been found in human cases of autosomal recessive retinitis pigmentosa (219,231). In the normal retina, the absorption of photons in the photoreceptors results in the activation of the phosphodiesterase, which degrades cyclic guanosine monophosphate (GMP) causing the closure of cyclic GMP gated ion channels. The mutation in the *Pde6b* gene causes deficient activity of the rod phosphodiesterase which results in the accumulation of cyclic GMP and death of rod cells (229). The rd10 mouse has a mutation in the same gene as mice with the *rd1* mutation, present in some common strains of mice, but the *rd10* mutation produces a milder degeneration with later onset (229).

Changes in other cellular and vascular layers occur, likely secondary to photoreceptor loss (10,218,230). The retinal vessels atrophy in the rd10 mouse model of retinal degeneration; injection of hematopoietic stem cells rescues retinal vessels from degradation and also rescues cellular layers of the retina including the cones of the photoreceptors, suggesting vascular dysfunction may be partially responsible for degeneration in this model (10). Electroretinography has shown that functional deficits are present in photoreceptors of rd10 mice from birth, but further decline in function occurs progressively eventually becoming undetectable (229).

6.2 Methods

Animal preparation: Experiments were performed on mice homozygous for the Pde6b mutation bred onto a C57BL/6J background (Jackson Laboratory, Bar Harbor, Maine). For controls, normal age-matched C57BL/6J mice were used (Jackson Laboratory, Bar Harbor, Maine). MRI and histology were performed on mice at post-natal ages 25, 35, and 60 days.

For MRI, animals were placed into a head holder with ear and tooth bars. Blood flow imaging was performed under 1.0-1.1% isoflurane, 30% oxygen with balance nitrogen, and spontaneous breathing conditions. For high resolution anatomical imaging urethane anesthesia was used (1.5 g/kg, intraperitoneal) and isoflurane discontinued. Under isoflurane alone, the eye is prone to motion (140), while urethane is effective at minimizing motion. The high resolution anatomical MR images had relatively long times to acquire a single image and low signal to noise (making motion correction perform worse), so preventing motion was much more important. A circulating warm water pad was used to maintain rectal temperature at 37 ± 0.5° C. Mice were prepared in a lit room before being transferred to the MRI room, in which lights were turned off. Lighting conditions were not changed during the duration of imaging. Breath rate, heart rate, and oxygen saturation were monitored during imaging (MouseOx, STARR Life Science Corp., Oakmont, PA).

MRI methods: MRI studies were performed on a 7 Tesla, 12 cm horizontal magnet and a 150 G/cm BGA6S gradient insert (Bruker, Billerica, Massachusetts). For imaging, a small circular surface eye coil with active decoupling (diameter = 6 mm) was placed over the left eye. A circular labeling coil (diameter = 8 mm) was placed at the heart position for a cardiac spin labeling technique as previously described (114). The two coils were separated by 2.3 cm from center to center.

BF MRI was acquired using two-coil continuous ASL with an EPI sequence. Paired images, one with and one without labeling, were acquired in an interleaved fashion. ASL employed a 2.6 s square radio frequency pulse to the labeling coil in the presence of 2.0 G/cm gradient along the flow direction with a post label delay of 350 ms. The sign of the frequency offset was switched for non-labeled images. Images were acquired in a coronal orientation with a single slice passing through the optic nerve head, with the slice angled perpendicular to the retina. Two-segment, gradient-echo EPI was used with field of view = 6.0x6.0 mm^2, matrix = 144x144 (42x42 μm^2 resolution), a single 0.4 mm slice, TR = 3.0 s per segment, and TE = 9.7 in 25 and 60 day old mice or 12.6 ms for 35 day old mice. For each scan, 100 pairs of images were typically acquired in time-series with a total acquisition time of 20 min.

Anatomical images were acquired using a balanced steady state free precession (bSSFP) sequence at low and high resolutions. Low resolution scans were obtained with field of view = 5x5 mm^2, matrix = 120x120 (42x42 μm^2), a single 0.4 mm slice, and TE/TR = 3.6/7.2 ms. Data were oversampled by a factor of 2 in both frequency and phase encode directions. Fifty repetitions were acquired in time-series with 3 averages per repetition for an acquisition time of about 4.5 min. High resolution scans were obtained with a 3D acquisition with field of view = 4.48x4.48x3.2 mm^3, matrix = 128x128x16 (35x35x200 μm^2), and TE/TR = 3.3/6.5 ms. Data were oversampled by a factor of 2 in the frequency and first phase encode directions. Sixty four repetitions were acquired in time-series for an acquisition time of about 30 min.

Histology: At the end of the MRI session, the mice were euthanized, and eyes were enucleated and placed in 10% paraformaldehyde overnight. Eyes were then dehydrated with washes of ethanol and xylene. Whole eyes were embedded in paraffin and sectioned at 8 μm on a microtome. Multiple slices through the optic nerve were obtained and stained using hematoxylin and eosin. Thickness measurements were made at 100x from 2 different slices about 200-300 μm away from the optic nerve head and on both sides of the optic nerve.

Data analysis: Image analysis was done using codes written in Matlab (MathWorks, Natick, MA), STIMULATE software (University of Minnesota), and Statistical Parametric Mapping 5 (SPM5) software. Blood flow images were zero-padded to 256x256 (nominal resolution of 23x23 μm^2) before Fourier transform into imaging space. Anatomical images were zero-padded to 128x128 (nominal resolution of 39x39 μm^2). High resolution anatomical images were zero-padded to 256x256 (nominal resolution of 18x18 μm^2). Images were acquired in time series, aligned using the spatial realignment function in SPM5 and averaged off line. For the high resolution anatomical images, realignment and averaging was performed on the complex-valued images, which provided substantially better image quality and contrast to noise than if only the magnitude images were used.

Blood flow images of the eye, in units of ml/g/min, were calculated pixel-by-pixel using Eq. 1.1. λ, the water tissue-blood partition coefficient, was taken to be 0.9, the same as the brain (64). The retina and choroid T_1 at 7 T was taken to be 1.8 s (68). A value of 0.7 was used for α, the labeling efficiency, as was previously measured in the distal internal carotid arteries at the base of the frontal lobe (see Chapter 2) (114).

BF intensity profiles across the retinal thickness were obtained from BF images by radially projecting lines perpendicular to the retina with profiles obtained at 4x spatial interpolation (9,139). Further motion correction was performed on the extracted profiles in Matlab (see Chapter 4.2). BF profiles were averaged along the length of the retina, excluding the optic nerve head. Anatomical profiles were averaged over two 273 μm long regions located on either side of the optic nerve head. Measurements of peak values and layer thicknesses – defined as half-height width of anatomical or BF peaks – were determined from the average profiles for each animal.

rBF and chBF data were analyzed separately using two-way ANOVA to analyze effects of mouse strain and age. Multiple comparisons were made using the Bonferroni correction. Thickness measurements from MRI were compared using the Wilcoxon rank-sum test. Thickness measurements from histology were compared using two-way ANOVA or two-sided unpaired t-tests as specified. For all tests, $p < 0.05$ was considered significant.

6.3 Results

6.3.1 Anatomical MRI of Retinal Degeneration

Anatomical images at 42x42x400 μm^3 of a C57BL/6J and rd10 mouse at post natal 60 days are shown in Figure 6.1. Group average profiles from C57BL/6J and rd10 mice at post natal 25, 35 and 60 days are shown in Figure 6.1 C. In the normal C57BL/6J mice, 4 layers were present in the retina (including a layer that was the choroid) at all ages. In rd10 mice at all ages there were only 2 layers (including a layer that was the choroid) in the retina. Thicknesses of MRI anatomical layers are summarized in Table 6.1 and Figure 6.2.

The thickness of the neural retina was significantly less in rd10 mice compared to age matched C57BL6/J mice at 25, 35 and 60 days ($p < 0.05$), but the thickness of the choroid (MRI layer 4) was not changed. In rd10 mice the neural retina was significantly thinner at 35 and 60 days compared to 25 day old rd10 mice ($p < 0.01$). The neural retina was also significantly thinner in 60 day old rd10 mice compared to 35 day old rd10 mice

($p < 0.05$). However, the 10 µm difference in thickness is much less than the actual image resolution of 42 µm, and so may not be meaningful.

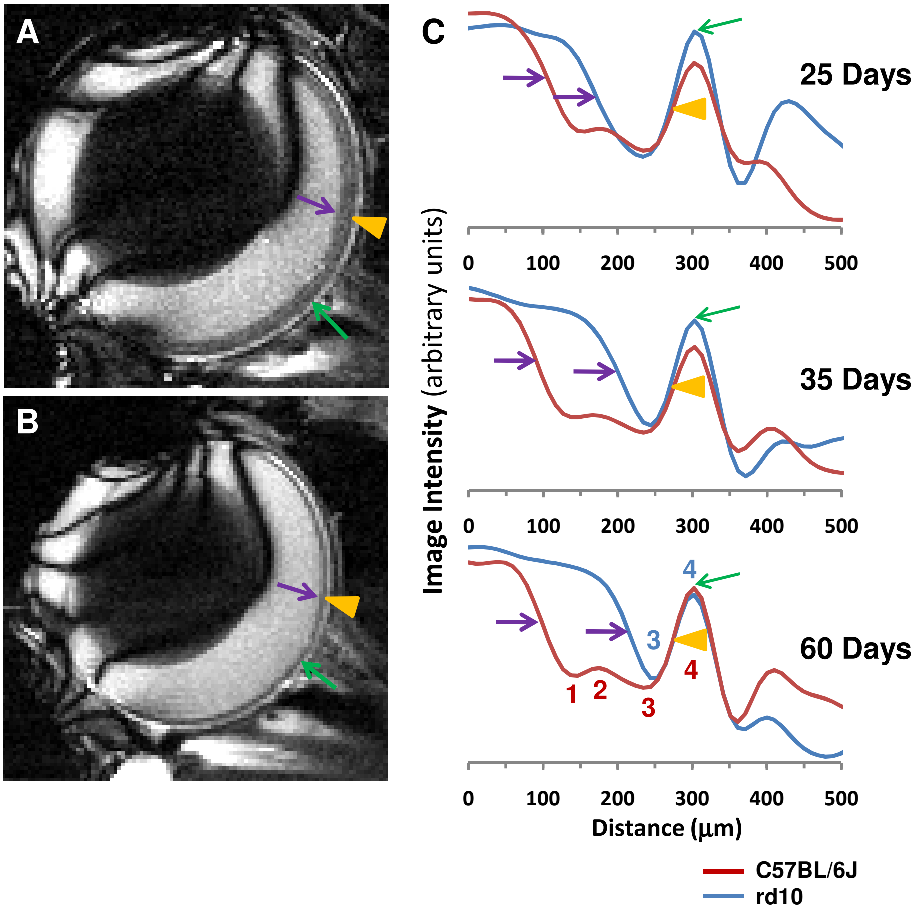

Figure 6.1: Anatomical images at 42x42x400 μm^3 from a single (A) C57BL/6J mouse and (B) rd10 mouse at 60 days post natal. (C) The group average anatomical profiles for C57BL/6J mice at postnatal 25, 35, and 60 days (n = 4, 6, and 6, respectively) and for rd10 mice at postnatal 25, 35, and 60 days (n = 4, 6, and 6, respectively). The choroid peaks from all profiles were aligned together. Four layers were present in the C57BL/6J retina, including the choroid (labeled 1-4 in red). Two layers were present in the rd10 retina, including the choroid (labeled 3-4 in blue). Layer 3 likely corresponds to different anatomical layers in the C57BL/6J and rd10 retina. The green arrows indicate the choroid (layer 4). The purple arrows indicate the vitreous-retina boundary and the orange arrowheads indicate the retina-choroid boundary.

Table 6.1: Thicknesses of anatomical MRI layers at 42x42x400 µm^3 from C57BL/6J and rd10 mice (µm, mean ± SD). Neural Retina is the sum of MRI Layers 1, 2, and 3
*p < 0.05, **p < 0.01 compared to age-matched C57BL6/J mice (statistical tests only used on Layer 4 and Neural Retina)

Age (days)	**Strain**	**n**	**MRI Layer** **Layer 1**	**Layer 2**	**Layer 3**	**Layer 4**	**Neural Retina**
25	C57BL/6J	4	59 ± 8	42 ± 5	71 ± 5	59 ± 8	171 ± 6
	rd10	4	-	-	105 ± 9	59 ± 0	105 ± 9*
35	C57BL/6J	6	63 ± 11	45 ± 5	75 ± 5	64 ± 12	182 ± 8
	rd10	6	-	-	75 ± 5	61 ± 4	75 ± 5**
60	C57BL/6J	6	63 ± 8	46 ± 10	73 ± 16	56 ± 5	182 ± 10
	rd10	6	-	-	65 ± 5	59 ± 0	65 ± 5**

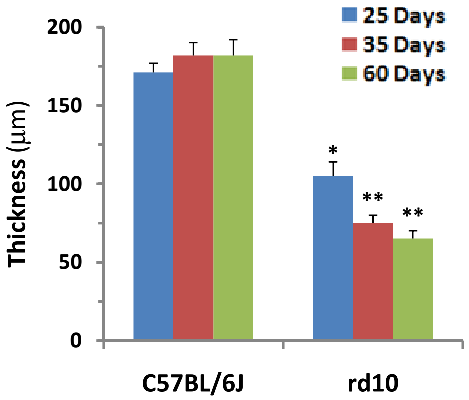

Figure 6.2: Group average thicknesses of the neural retina (sum of MRI layers 1, 2, and 3) from anatomical MRI at 42x42x400 µm^3 from C57BL/6J and rd10 mice at 25, 35, and 60 days post natal. Error bars represent standard deviation. *p < 0.05, **p < 0.01 compared to age-matched C57BL6/J mice.

High resolution anatomical images at 35x35x200 µm^3 of a C57BL/6J and rd10 mouse at post natal 25 days are shown in Figure 6.3. Group average profiles from C57BL/6J and rd10 mice at post natal 25 days are shown in Figure 6.3 C. In the normal C57BL/6J mice, 6 layers were present in the retina at high resolution (including a layer that was the choroid). In rd10 mice, 4 layers were detected (including a layer that was the choroid) in the retina. Thicknesses of high-resolution MRI anatomical layers are summarized in Table 6.2. The thickness of the neural retina was significantly less in rd10 mice compared to age matched C57BL6/J mice ($p < 0.05$), but the thickness of the choroid (MRI layer 6) was not changed.

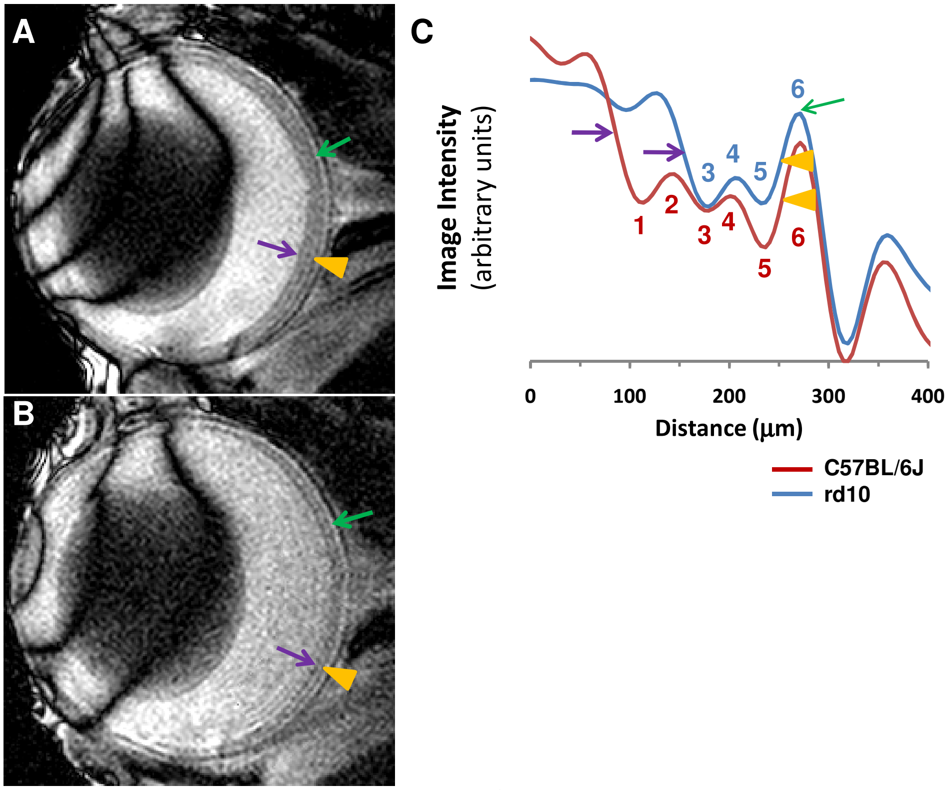

Figure 6.3: Anatomical images at 35x35x200 μm^3 from a (A) C57BL/6J and (B) rd10 mouse at 25 days post natal. (C) The group average anatomical profiles for C57BL/6J and rd10 mice at post natal 25 days (n = 4 and 4, respectively). The choroid peaks from all profiles were aligned together. Six layers were present in the C57BL/6J retina, including the choroid (labeled 1-6 in red). Four layers were present in the rd10 retina, including the choroid (labeled 3-6 in blue). Layers 3-5 likely correspond to different anatomical layers in the C57BL/6J and rd10 retina. The green arrows indicate the choroid (layer 6). The purple arrows indicate the vitreous-retina boundary and the orange arrowheads indicate the retina-choroid boundary.

Table 6.2: Thicknesses of anatomical MRI layers at 35x35x200 μm^3 from C57BL/6J (n = 4) and rd10 (n = 4) mice at post natal 25 days (µm, mean ± SD). Neural Retina is the sum of MRI Layers 1-5

*$p < 0.05$ compared to age-matched C57BL6/J mice (statistical tests only used on Layer 6 and Neural Retina)

			MRI Layer				Neural
Strain	**Layer 1**	**Layer 2**	**Layer 3**	**Layer 4**	**Layer 5**	**Layer 6**	**Retina**
C57BL/6J	42 ± 3	34 ± 2	30 ± 3	29 ± 5	35 ± 0	40 ± 3	169 ± 3
rd10	-	-	38 ± 2	27 ± 3	33 ± 2	40 ± 3	98 ± 4*

Histology was acquired in the same mice as MRI at 25 and 60 days post natal (Figure 6.4). In 60 day old rd10 mice the inner and outer segments could not be detected. The outer nuclear and outer plexiform layers were substantially reduced to the point that they could not be cleanly distinguished from each other (so in this group a single value is reported for both layers). In 25 day old rd10 mice the inner and outer segments could not be distinguished from each other, so a single value is reported for both layers. Anatomical layer thicknesses are summarized in Table 6.3.

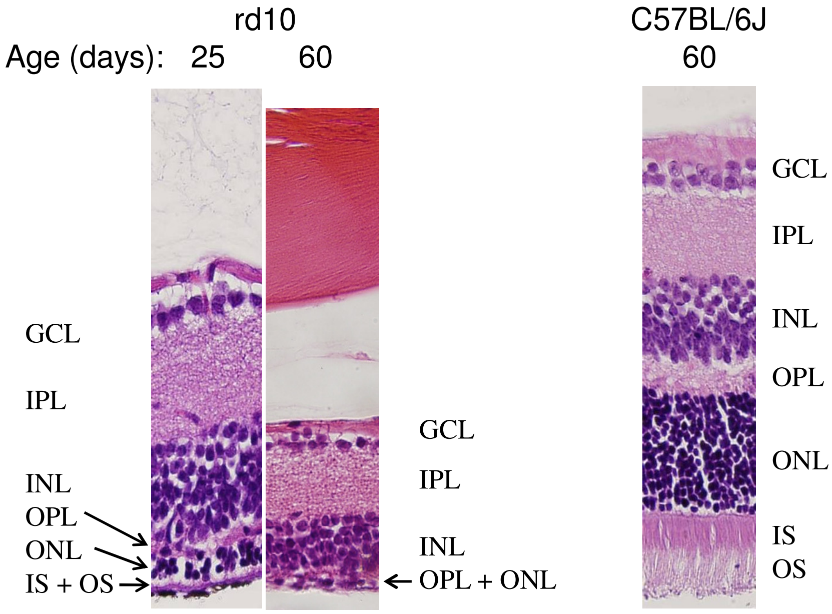

Figure 6.4: Histology of rd10 and C57BL/6J mouse retinas obtained at 40x magnification. GCL – ganglion cell and nerve fiber layers, IPL – inner plexiform layer, INL – inner nuclear layer, OPL – outer plexiform layer, ONL – outer nuclear layer, IS – inner segment, OS – outer segment.

Two-way ANOVA was separately run on the total neural retina, GCL, IPL, INL. For OPL, ONL, IS, and OS, two-sided unpaired t-tests were used since these layers were missing in groups of the rd10 mice. With the layers that were combined in the rd10 mice, comparisons were made to the corresponding sum of the layers (ie OPL+ONL for the 60 day old rd10 mice). Each layer of the 60 day old rd10 mouse was significantly thinner compared to 25 and 60 day old C57BL/6J mice and 25 day old rd10 mice. In 25 day old rd10 mice, all of the outer layers of the retina were significantly thinner, while none of the inner retinal layers were changed. The only significant difference between 25 and 60 day old C57BL/6J mice was the outer segment ($p < 0.05$, two-sided unpaired t-test).

Table 6.3: Thicknesses of histological layers from C57BL/6J and rd10 mice (µm, mean ± SD). Neural Retina is the sum of all layers
$^{a}p < 0.05$ between rd10 and age-matched C57BL/6J mice, $^{b}p < 0.05$ between 60 and 25 day old rd10 mice, $^{c}p < 0.05$ between 60 and 25 day old C57BL/6J mice

Age (days)	**Strain**	**n**	**GCL**	**IPL**	**INL**	**OPL**	**ONL**	**IS**	**OS**	**Neural Retina**
25	C57BL/6J	4	23 ± 3	55 ± 2	39 ± 3	16 ± 2	55 ± 2	18 ± 1	22 ± 2	229 ± 8
	rd10	4	20 ± 1	56 ± 2	41 ± 3	12 ± 1^{a}	14 ± 1^{a}	7 ± 1^{a}		150 ± 5^{a}
60	C57BL/6J	6	22 ± 2	54 ± 3	41 ± 3	15 ± 1	56 ± 3	17 ± 2	26 ± 2^{c}	231 ± 8
	rd10	6	16 ± 3^{ab}	40 ± 3^{ab}	32 ± 2^{ab}	9.7 ± 2^{ab}		-	-	98 ± 7^{ab}

6.3.2 Blood Flow MRI of Retinal Degeneration

BF images at 42x42x400 μm^3 of a C57BL/6J and rd10 mouse at post natal 60 days are shown in Figure 6.5. Group average BF profiles from C57BL/6J and rd10 mice at post natal 25, 35 and 60 days are shown in Figure 6.6. In the normal C57BL/6J mice at all ages, 2 BF peaks, corresponding to rBF and chBF, were present and were separated by a dip. In the rd10 mice, the chBF peak was easily distinguished at all ages, but the rBF peak was not as clear. At 25 days there was an obvious rBF layer, but it was not well separated from the chBF. At 35 days, there generally seemed to be a weak layer in the BF images that was likely the rBF, but it was not separated from the chBF and was generally difficult to distinguish from noise. At 60 days, rBF was even more difficult to detect, and in some animals could not be distinguished.

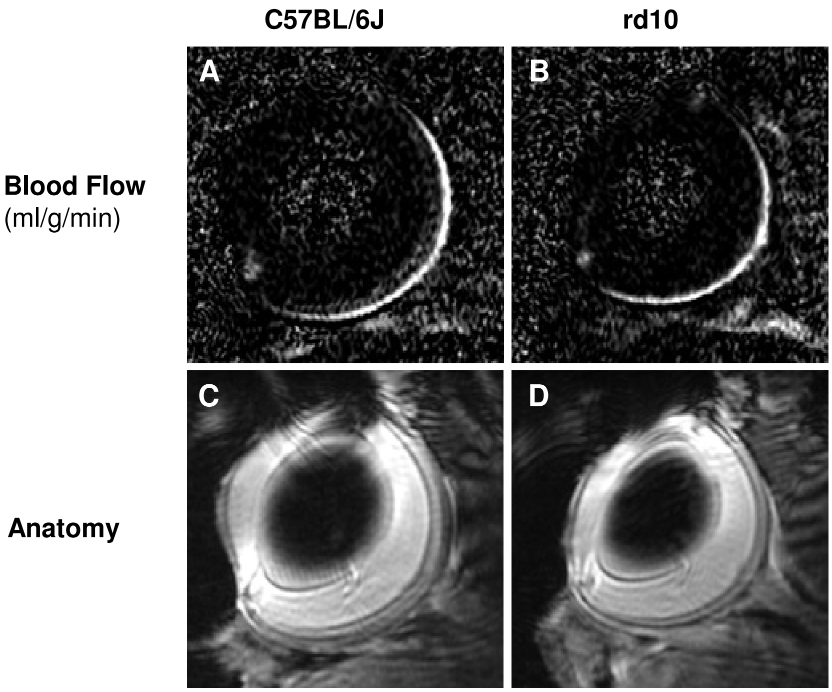

Figure 6.5: Blood flow images at 42x42x400 μm^3 from a single (A) C57BL/6J mouse and (B) rd10 mouse at 60 days post natal. (C,D) The corresponding EPI images.

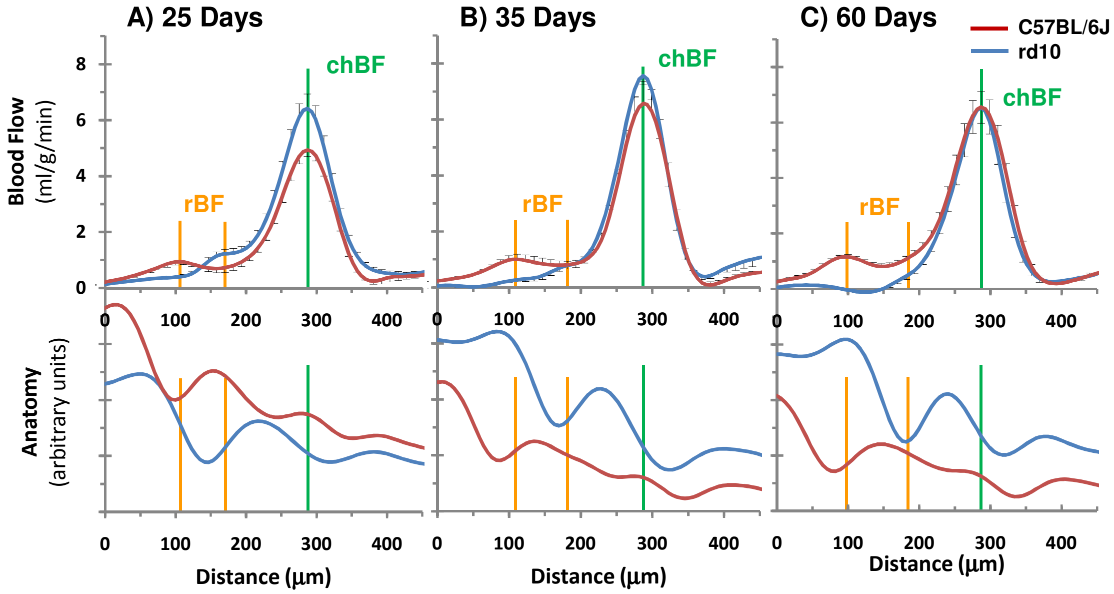

Figure 6.6: Group average BF profiles (top row) for rd10 and C57BL/6J mice at post natal (A) 25 (n = 4 and 4, respectively), (B) 35 (n = 6 and 6, respectively), and (C) 60 days (n = 6 and 6, respectively). Error bars represent standard error of the mean. The bottom row is the corresponding group average anatomical profiles from the non-labeled EPI images. The chBF peak is marked by the green vertical lines and rBF peak is marked by the orange vertical lines. Two orange lines are shown in each plot to indicate the rBF layer of both C57BL/6J and rd10 mice, which had different locations.

In the group averaged BF profiles, there was a small hump inside the choroid in the profile of the rd10 mice at 35 days that is probably the rBF layer, although there is no dip separating it from the chBF layer. At 60 days, even this small hump seemed to almost completely disappear, although rBF was not significantly different between the two ages. Values of rBF and chBF, as well as physiological parameters, are summarized in Table 6.4 and Figure 6.7. None of the physiological parameters were significantly different between aged matched C57BL/6J and rd10 mice ($p > 0.05$, two-sided unpaired t- tests).

The results of ANOVA showed that the strain had a significant effect on rBF ($p < 0.01$) and chBF ($p < 0.05$). Age did not have a significant effect on rBF or chBF ($p > 0.05$). The interaction of strain and age was significant for rBF ($p > 0.05$), but not chBF. Multiple comparisons of groups showed that rBF of 60 day old rd10 mice was significantly less than 35 and 60 day old C57BL/6J as well as 25 day old rd10 mice. Additionally, chBF in 25 day old C57BL/6J was significantly less than 35 day old rd10 mice.

Table 6.4: Retinal BF, choroidal BF, and physiological parameters during BF imaging from C57BL/6J and rd10 mice (mean ± SD). RR – respiration rate, HR – heart rate, SaO$_2$ – arterial oxygen saturation
$^{a}p < 0.05$, $^{b}p < 0.05$compared to ^{B}

Age (days)	**Strain**	**n**	**Weight** (g)	**RR** (breath/min)	**HR** (beat/min)	**SaO$_2$** (%)	**chBF** (ml/g/min)	**rBF** (ml/g/min)
25	C57BL/6J	4	14 ± 1	115 ± 6	507 ± 50	98.3 ± 0.6	5.0 ± 0.4^{a}	0.9 ± 0.2
	rd10	4	12 ± 1	120 ± 9	421 ± 53	98.8 ± 0.5	7.0 ± 1.1	1.1 ± 0.2^{B}
35	C57BL/6J	6	18 ± 1	117 ± 6	475 ± 69	98.3 ± 0.3	6.8 ± 1.9	1.1 ± 0.6^{B}
	rd10	6	19 ± 1	118 ± 10	430 ± 35	98.7 ± 0.4	8.3 ± 1.1^{a}	0.7 ± 0.3
60	C57BL/6J	6	20 ± 2	117 ± 4	483 ± 41	98.6 ± 0.4	6.7 ± 1.5	1.2 ± 0.2^{B}
	rd10	6	18 ± 2	121 ± 7	524 ± 30	98.5 ± 0.1	6.9 ± 1.8	0.5 ± 0.2^{b}

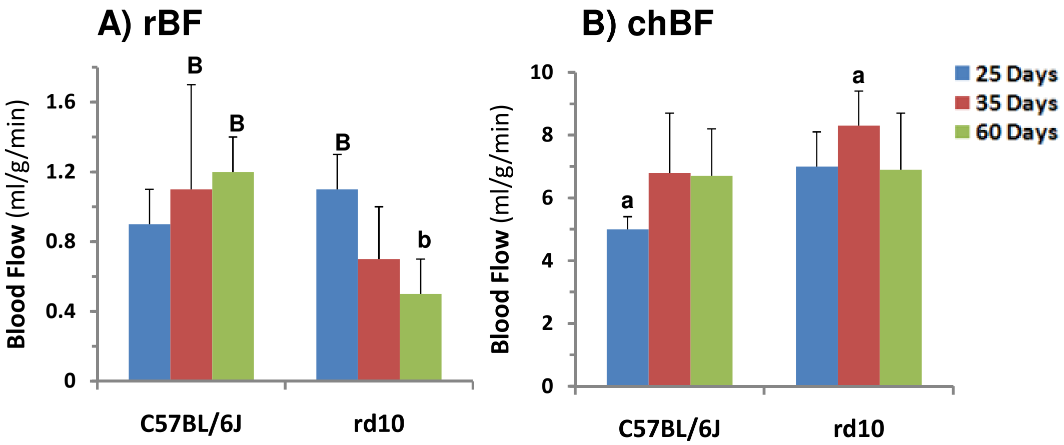

Figure 6.7: Group average (A) retinal and (B) choroidal BF in C57BL/6J and rd10 mice at 25, 35, and 60 days post natal. Error bars represent standard deviation. $^{a}p < 0.05$, $^{b}p < 0.05$compared to ^{B}.

6.4 Discussion

The retina of the rd10 mouse had substantial degeneration of the photoreceptors by post natal 25 days, resulting in a thinner retina measured by anatomical MRI and histology. The rd10 mouse retina underwent further thinning and degeneration at post natal 35 and 60 days. Retinal BF in the rd10 mouse was reduced at 60 days compared to age matched controls and 25 day old rd10 mice. However, choroidal BF was not affected in the rd10 mice at any stage of disease.

Retinal thickness and anatomical MRI: The neural retina was substantially thinner in the rd10 mice compared to age-matched controls. The thickness of the choroid did not change. Low resolution MR images ($42x42x400 \mu m^3$) had 3 layers in the neural retina of normal C57BL/6J mice. The neural retina was reduced from 3 layers to 1 layer in rd10 mice at all ages. Low resolution MRI could detect differences in retinal thickness at all ages of rd10 mice compared to age matched controls. The low resolution MRI could also clearly detect thinning of the rd10 retina over time, with the retina being substantially thinner at 35 and 60 days compared to 25 days. High resolution MR images (35x35x200 μm^3) had 5 layers in the neural retina in normal C57BL/6J mice but only 3 layers in 25 day old rd10 mice.

Both the low and high resolution anatomical MRI provided similar measurements of the neural retina thickness in 25 day old C57BL/6J (low – 171 μm, high – 169) and rd10 mice (low – 105 μm, high – 98 μm). However, the choroid seemed slightly thicker in the low resolution MRI (59 μm in both C57BL/6J and rd10 mice) compared to high resolution MRI (40 μm in both C57BL/6J and rd10 mice). The thickness of the neural retina measured from MRI was much less compared to histology from the 25 day old mice however (229 μm in C57BL/6J and 150 μm in rd10 mice). The difference in thickness between C57BL/6J and rd10 mice is similar measured from both MRI (66 μm) and histology (79 μm).

At 60 days, the photoreceptors (outer nuclear layer and inner/outer segments) were almost completely gone in the histology. The neural retina was measured to be thinner from MRI (182 μm in C57BL/6J and 65 μm in rd10 mice) compared to histology (231 μm in C57BL/6J and 98 μm in rd10 mice). The difference in thickness between C57BL/6J and rd10 mice was 117 μm from MRI and 133 μm from histology, which is again more similar than the thicknesses.

Possible reasons for the differences in thickness between MRI and histology include partial volume effects in the relatively low resolution MR images or distortion of the retina during fixation and sectioning. Regardless of the discrepancy between MRI and histology, both methods detected thinning of the retina in the 25 and 60 day old rd10 mice.

Blood flow measurement: In normal C57BL/6J mice, two separated BF layers, corresponding to rBF and chBF, could be distinguished. In 25 day old rd10 mice, the rBF and chBF layers were clearly present in all mice, but were not well separated. In two 25 day old rd10 mice the two BF peaks were separated by a slight dip in the BF profile; in the other two 25 day old rd10 mice the two BF layers were not separated. In rd10 mice at 35 and 60 days, the chBF layer was still clearly present, but the rBF layer was difficult to detect, particularly at 60 days. A small hump that was not separated from the chBF layer could generally be found at 35 days, but at 60 days, even this was essentially gone. Due to the loss of most of the avascular layer (outer nuclear layer and inner/outer segments), it is expected that the rBF and chBF would no longer be separated by a region of minimal BF.

The difficulty in detecting the rBF layer could be due to reduced BF or insufficient resolution to detect the thinned retinal vascular layer. Both likely occur to some extent. Based on the anatomical profiles of the EPI images, the neural retina was still thick enough to be clearly distinguished. This suggests that rBF, if present, should still be able to be detected by MRI. The presence of the rBF layer in the 35 day old rd10 mice supports this (since 35 and 60 day old rd10 mice had similar retinal thicknesses based off the low-resolution anatomical MRI).

Partial volume of the rBF layer could affect comparison of quantitative rBF values between normal and thinned retina. The thinned retina of the rd10 mice could be more prone to partial volume with the avascular vitreous and highly vascularized choroid. Since the inner retina, where the retinal vasculature is located, is only modestly thinned in the rd10 mice, the partial volume from the vitreous to the rBF is likely not altered much.

The loss of most of the avascular outer retina moves the rBF layer much closer to the strong chBF peak, and likely introduces some amount of partial volume from the choroid. This would be expected to erroneously increase rBF, making detection of decreased rBF more difficult.

Retinal and choroidal BF in retinal degeneration: In the rd10 mouse model of retinal degeneration, rBF had a trend of decreasing overtime, but was only significantly reduced at 60 days. chBF was unaffected in rd10 mice up to 60 days old. In 25 day old C57BL/6J mice, chBF was significantly lower compared to 35 day old rd10 mice. chBF was otherwise consistent between all groups. Due to the noisiness of the BF data, the lack of any other differences in chBF, and the small sample size, this difference is possibly not real and may disappear with larger samples.

Previous studies of retinal degeneration have found decreased rBF and potentially decreased chBF. In humans, diameter, blood velocity, and blood flow in retinal veins were all lower in retinitis pigmentosa patients, as well as total rBF (217). In a cat model of retinitis pigmentosa, rBF was compromised while chBF was not significantly affected (7). However, in human patients, the ocular pulse amplitude, used as an indication of chBF, is reduced in later stages of the disease, but not early (226).

Previous MRI studies in the RCS rat model of retinal degeneration have also found changes in BF. In a relatively low-resolution study imaging combined retinal/choroidal BF, the combined BF was lower in RCS rats with retinal degeneration (8). The combined retinal/choroidal BF signal in rats is probably dominated by the very high chBF, so the reduced BF found in RCS rats suggests possible changes in chBF in the model. However, in another study of the RCS rat with layer-specific BF of the retina and choroid, chBF was not altered in the RCS rat (232). The rBF layer could be detected in normal rats but was absent in the RCS rats. It was unclear whether the resolution was insufficient to separate rBF from chBF, or if rBF was reduced so much as to be undetectable.

There is evidence that the attenuation of retinal vasculature is due to hyperoxia in the retina caused by the loss of metabolically active photoreceptors (23,157,221,222,233). Using oxygen electrodes, RCS rats had higher oxygen in the remaining outer retina, increased flow of oxygen from the choroid to the inner retina, and reduced oxygen input from the retinal circulation (157,222,234). In a cat model of retinal degeneration, the inner retinal oxygen was not altered while the retinal vessels were attenuated (233). Contrary to these findings, hyperbaric oxygen therapy preserves vision in retinitis pigmentosa patients, suggesting retinal hypoxia which then leads to increased photoreceptor degeneration (225). Additionally, it has been found that injection of hematopoetic stem cells into the eye of rd mice prior to degeneration rescues retinal vasculature from atrophy, reduces degeneration of the outer retina, and preserves some electroretinogram (ERG) response (10).

6.5 Conclusions

High resolution MRI could detect anatomical and physiological changes at different stages of disease in the retina of the rd10 mouse model of retinal degeneration. Retinal blood flow was reduced at a late stage of retinal degeneration, while choroidal blood flow was unchanged. Future studies could measure functional BF changes to physiological stimulations. Since MRI provides a non-invasive method to pinpoint anatomical and vascular changes *in vivo*, it could be used for longitudinal studies of retinal degeneration and testing of potential treatments.

CHAPTER 7

CONCLUSION

This thesis detailed the development of MRI methods to image anatomy, function, and blood flow (BF) of the retina and choroid, and their application to two diseases of the retina: diabetic retinopathy and retinal degeneration. MRI provides anatomical, functional, and physiological images at relatively high spatial resolution, is non-invasive, and does not have depth limitation. MRI is widely used to study anatomy and physiology throughout the body due to these favorable properties. However, the application of MRI to study the retina is still difficult due to the very small size of the retina. The retina, which can be seen through the pupil, has thus traditionally been studied using optical techniques, which are mostly limited to probing the retinal surface.

In order to image BF of the retina, a technique to image BF in mice with good sensitivity was needed. To perform BF imaging, a two-coil continuous arterial spin labeling (ASL) technique was developed and applied to image cerebral blood flow in mice. Two-coil continuous ASL has been employed in rats (13,103), humans (69), and monkeys (70,104), but it had not yet been extended to mice. The approach, which used a labeling coil placed at the heart, provided all the benefits of two-coil continuous ASL including, high labeling efficiency, ability for multi-slice acquisitions, and lack of magnetization transfer artifacts.

The retina is nourished by two distinct circulations, the retinal vessels within the inner retina and the choroid vessels behind the neural retina. These two vascular layers are separated by an avascular region of the outer retina. There are substantial differences in basal BF and regulation of BF between the two blood supplies (22,25,26,34,35,37), so it is important to be able to distinguish the two vasculatures. The continuous ASL technique with cardiac labeling proved capable of imaging cerebral BF in mice with good SNR and BF contrast in relatively short time. Thus, this technique was promising for BF studies of the mouse retina.

High-resolution cardiac ASL could image quantitative, layer-specific retinal BF (rBF) and choroidal BF (chBF) in the mouse retina *in vivo*. BF differences due to different anesthetics and hypoxic challenge could be detected with MRI. This demonstrated for the first time that MRI could be used to image layer-specific blood flow to the retina and choroid, providing both basal BF and functional BF changes. Quantitative blood flow measurement affords comparison of BF changes between experimental groups, facilitating early detection and monitoring of treatment efficacy. The BF fMRI technique could provide a means of studying neurovascular coupling of the retinal and choroid vessels in disease states as well.

With the feasibility of layer-specific BF MRI of the retina and choroid having been demonstrated in healthy mice, the method was applied to study BF in two retinal diseases: diabetic retinopathy and retinal degeneration. Diabetic retinopathy is the leading cause of blindness in most developed countries (170,171). Dysfunction of the retinal vasculature is the most prominent feature of diabetic retinopathy, signs of which are used clinically to diagnosis the disease. ASL MRI was utilized to image quantitative, layer-specific rBF and chBF in the Ins2^{Akita} mouse model of diabetic retinopathy. The Ins2^{Akita} mouse has deficient β cells in the pancreas resulting in hypoinsulemia and hyperglycemia

(207). Further, the vision of the hyperglycemic mice was studied using psychophysical tests to determine changes of visual acuity and contrast sensitivity in diabetic mice (199).

In aged hyperglycemic mice, rBF was lower and acuity and contrast sensitivity were worse, indicating retinopathy. However, the reduction in BF and worsening of vision did not seem to be correlated in the hyperglycemic mice, suggesting these changes may occur through independent mechanisms. Further studies are needed to determine the effects of hyperglycemia at earlier time points and to corroborate the unique BF and visual findings in the $Ins2^{Akita}$ mouse. Decreased rBF is consistent with previous studies in other animal models of diabetes (30,187,202-204). However, in general the changes in retinal and choroidal BF in diabetic retinopathy are complex and remain unclear, with conflicting reports finding no changes of BF in diabetics (2,177), increased BF (3,178,179), and decreased BF (4).

Retinitis pigmentosa is the most common inherited form of retinal degeneration, affecting 1.5 million people worldwide (215). Retinitis pigmentosa is a group of retinal dystrophies that cause photoreceptor death and blindness (216). There is also evidence of vascular disruption in the retina (7,10,217), although this factor has not been well studied.

MRI was utilized to image quantitative, layer-specific retinal and choroidal BF and anatomy in the rd10 mouse model of retinal degeneration at different stages of degeneration. In the rd10 mice, the retina was much thinner as cellular layers degenerated, as detected by anatomical MRI and histology. Retinal BF was found to be reduced at later stages of degeneration, while chBF was unaffected in rd10 mice. This is in agreement with previous studies of retinal degenerations. In humans, blood flow in retinal veins is lower in retinitis pigmentosa patients, as well as total rBF (217). In a cat model of retinitis pigmentosa, rBF is compromised while chBF was not significantly affected (7). A study using ASL MRI in a rat model of retinal degeneration showed that chBF was not affected, while rBF was decreased (232). These studies demonstrate that BF is affected in retinal degeneration, although it is not clear if this is only a side-effect of retinal damage or possibly involved in degeneration.

7.1 Future Work

These studies showed the feasibility of using high-resolution MRI to study the retina in mice. Although the results demonstrated that MRI could be a useful tool for imaging the retina, further improvement of the techniques are necessary. In particular, much work remains to further develop and validate ASL MRI to image BF of the retina and choroid. MRI was used to acquire unique information about retinal / choroidal BF under different anesthetics and disease states. However, no previous reports of retinal and choroidal BF differences between isoflurane and ketamine/xylazine, in the $Ins2^{Akita}$ mouse model of diabetes, or in the rd10 mouse model of retinal degeneration could be found for comparison. Therefore, it would help to validate the utility of ASL MRI in the retina if these unique findings could be corroborated by other, more established techniques, like laser Doppler velocimetry or microspheres.

There is also much more that could be done to improve the sensitivity and quantitative accuracy of MRI BF measurements in the retina. Background suppression has been widely utilized in ASL sequences to reduce the noise of the BF signal by suppressing the static tissue signal (56). Background suppression was explored to some extent in Chapter 3.2, but preliminary results found little improvement in the BF signal, so this method was not used in later studies. However, background suppression seems to be important in obtaining layer-specific BF MRI of the rat retina and choroid (232). Also, as demonstrated in Chapter 4, EPI is not an ideal sequence for imaging the retina. Standard gradient echo and spin echo sequences would not have the speed or signal to noise ratio necessary for BF MRI. Alternative sequences that have rapid acquisition, such as bSSFP or gradient and spin echo (GRASE), have had promising results in the brain and kidneys (235,236). Application of these sequences to acquire ASL data of the retina might be another way of improving BF measurements.

More complicated models to calculate BF have been developed, such as two compartment models (73), which account for more parameters. Although more complex models might give more accurate BF values, they require the measurement of additional parameters used in the calculation, making their implementation difficult. Their application to the retina is currently impractical due to the difficulty and long times needed to obtain even simple BF measurements. Also determination of the water tissue blood partition coefficient for the retina and choroid could possibly be made. The water content of the neural retina has been determined (66), so it is possible that similar experiments could be performed on the choroid as well.

Future studies should also look at regulation of rBF and chBF in disease in addition to basal BF. Although BF and BOLD fMRI of the retina was detailed in Chapter 3, the hypoxic stimulation likely provides limited information on the local regulation of rBF and chBF. The hypoxic challenge seems to cause large drops in systemic blood pressure, which may be the cause of the BF changes of the retina/choroid, rather than local vasoconstriction of the two vasculatures. An ideal stimulation should directly cause vasoconstriction or dilation of the retinal and choroidal vasculatures without altering the subject's physiology. Hypercapnic stimulation which is widely used in studies of cerebral BF may offer a more relevant stimulation. Preliminary studies of the affect of hypercapnia in the mouse retina have shown inconsistency. Some mice show moderate to strong changes in rBF and chBF in response to hypercapnia, but others seem to have absolutely no BF response to the stimulation. Mechanically ventilating mice and monitoring blood gas could possibly provide more stable physiology and give more consistent BF changes. Other stimulations, such as pharmacological challenge (for example sodium nitroprusside or phenylephrine (237)), could be explored as a means of studying BF regulation in the retina and choroid.

MRI has the potential to provide unique, layer-specific information about the retina and choroid non-invasively. Although MRI of the retina is difficult and is limited by resolution and signal to noise ratio, the studies detailed in this thesis demonstrate the feasibility of layer-specific MRI to study anatomy, function, and blood flow of the retina in mice. Further, these methods were shown to provide a novel means of studying animal models of retinal disease *in vivo*. Future improvements of MRI techniques should enhance and broaden their utility as a method to study the retina.

REFERENCES

1. Pemp B, Schmetterer L. Ocular blood flow in diabetes and age-related macular degeneration. Can J Ophthalmol 2008;43:295-301.

2. Gilmore ED, Hudson C, Nrusimhadevara RK, Ridout R, Harvey PT, Mandelcorn M, Lam WC, Devenyi RG. Retinal arteriolar hemodynamic response to an acute hyperglycemic provocation in early and sight-threatening diabetic retinopathy. Microvasc Res 2007;73(191-197).

3. Pemp B, Polska E, Garhofer G, Bayerle-Eder M, Kautzky-Willer A, Schmetterer L. Retinal blood flow in type 1 diabetes patients with no or mild diabetic retinopathy during euglycemic clamp. Diabetes Care 2010.

4. Burgansky-Eliash Z, Nelson DA, Bar-Tal OP, Lowenstein A, Grinvald A, Barak A. Reduced retinal blood flow velocity in diabetic retinopathy. Retina 2010;30:765-773.

5. Flammer J, Orgul S, Costa VP, Orzalesi N, Krieglstein GK, Serra LM, Renard JP, Stefansson E. The impact of ocular blood flow in glaucoma. Prog Retin Eye Res 2002;21:359-393.

6. Roth S, Pietrzyk Z. Blood flow after retinal ischemia in cats. Invest Ophthalmol Vis Sci 1994;36:1904-1909.

7. Nilsson SFE, Maepea O, Alm A, Narfstrom K. Ocular blood flow and retinal metabolism in Abyssinina cats with hereditary retinal degeneration. Invest Ophthalmol Vis Sci 2001;42:1038-1044.

8. Li Y, Cheng H, Shen Q, Kim M, Thule PM, Olson DE, Pardue MT, Duong TQ. Blood-flow Magnetic Resonance Imaging of Retinal Degeneration. Invest Ophthalmol Vis Sci 2009;50:1824-1830.

9. Cheng H, Nair G, Walker TA, Kim MK, Pardue MT, Thule PM, Olson DE, Duong TQ. Structural and functional MRI reveals multiple retinal layers. Proc Natl Acad Sci USA 2006;103:17525-17530.

10. Otani A, Dorrell MI, Kinder K, Moreno SK, Nusinowitz S, Banin E, Heckenlively J, Friedlander M. Rescue of retinal degeneration by intravitreally injected adult bone marrow-derived lineage-negative hematopoietic stem cells. J Clin Invest 2004;114:765-774.

11. Brown GG, Clark C, Liu TT. Measurement of cerebral perfusion with arterial spin labeling: part 2. applications. J Int Neuropsycholog Soc 2007;13:526-538.

12. Chalela JA, Alsop DC, Gonzalez-Atavales JB, Maldjian AA, Kasner SE, Detre JA. Magnetic resonance perfusion imaging in acute ischemic stroke using continuous arterial spin labeling. Stroke 2000;31:680-687.

13. Shen Q, Fisher M, Sotak CH, Duong TQ. Effect of reperfusion on ADC and CBF pixel-by-pixel dynamics in stroke: Characterizing tissue fates using quantitative diffusion and perfusion imaging. J Cereb Blood Flow and Metab 2004;24:280-290.

14. Weber MA, Zoubaa S, Schlieter M, Juttler E, Huttner HB, Geletneky K, Ittrich C, Lichy MP, Kroll A, Debus J, Giesel FL, Hartmann M, Essig M. Diagnostic performance of spectroscopic and perfusion MRI for distinction of brain tumors. Neurology 2006;66:1899-1906.

15. Asllani I, Habeck C, Scarmeas N, Borogovac A, Brown TR, Stern Y. Multivariate and univariate analysis of continuous arterial spin labeling perfusion MRI in Alzheimer's disease. J Cereb Blood Flow and Metab 2008;28:725-736.

16. Niwa K, Kazama K, Younkin SG, Carlson GA, Iadecola C. Alterations in cerebral blood flow and glucose utilization in mice overexpressing the amyloid precursor protein. Neurobiol Disease 2002;9:61-68.

17. Wolf RL, Alsop DC, Levy-Reis I, Meyer PT, Maldjian AA, Gonzalez-Atavales JB, French JA, Alavi A, Detre JA. Detection of mesial temporal lobe hypoperfusion in patients with temporal lobe epilepsy by use of arterial spin labeled perfusion MR imaging. Am J Neuroradiol 2001;22:1134-1341.

18. Sharma RK, Ehinger BEJ. Development and Structure of the Retina. In: Alm A, Ehinger BEJ, Kaufman PL, editors. Adler's Physiology of the Eye - 10th ed. St. Louis: Mosby; 2003. p 319-343.

19. Chen J, Wang Q, Zhang J, Yang X, Wang J, Berkowitz BA, Wickline SA, Song SK. In vivo quantification of T1, T2, and apparent diffusion coefficient in the mouse retina at 11.74T. Magn Reson Imaging 2008;59:731-738.

20. Picaud S. Retinal Biochemistry. In: Alm A, Ehinger BEJ, Kaufman PL, editors. Adler's Physiology of the Eye - 10th ed. St. Louis: Mosby; 2003. p 382-403.

21. Cunha-Vaz JG. The blood-retinal barriers. Documenta Ophthalmol 1976;41:287-327.

22. Cioffi GA, Granstam E, Alm A. Ocular Circulation. In: Kaufman PL, Alm A, editors. Adler's Physiology of the Eye - 10th ed. St. Louis: Mosby; 2003. p 747-776.

23. Stone J, Valter K. Roles of Oxygen in the Stability of Photoreceptors. In: Chalupa LM, Williams RW, editors. Eye, Retina, and Visual System of the Mouse. Cambridge: MIT Press; 2008. p 559-572.

24. Linsenmeier RA, Braun RD. Oxygen distribution and consumption in the cat retina during normoxia and hypoxemia. J Gen Physiol 1992;99(2):177-197.

25. Roth S. The effects of halothane on retinal and choroidal blood flow in cats. Anesthesiology 1992;76:455-460.

26. Tilton RG, Chang K, Weigel C, Eades D, Sherman WR, Kilo C, Williamson JR. Increased ocular blood flow and 125I-Albumin Permeation in Galactose-Fed Rats: Inhibition by Sorbinil. Invest Ophthalmol Vis Sci 1988;29:861-868.

27. Lin J, Roth S. Ischemic preconditioning attenuates hypoperfusion after retinal ischemia in rats. Invest Ophthalmol Vis Sci 1999;40(12):2925-2931.

28. Pouliot M, Deschenes MC, Hetu S, Chemtob S, Lesk MR, Couture R, Vaucher E. Quantitative and regional measurement of retinal blood flow in rats using N-isopropyl-p-[14C]-iodoamphetamine ([14C]-IMP). Exp Eye Res 2009;89:960-966.

29. Linsenmeier RA, Padnick-Silver L. Metabolic dependence of photoreceptors on the choroid in the normal and detached retina. Invest Ophthalmol Vis Sci 2000;41:3117-3123.

30. Clermont AC, Brittis M, Shiba T, McGovern T, King GL, Bursell SE. Normalization of retinal blood flow in diabetic rats with primary intervention using insulin pumps. Invest Ophthalmol Vis Sci 1994;35:981-990.

31. Riva CE, Grunwald JE, Singclair SH. Laser Doppler velocimetry study of the effect of pure oxygen breathing on retinal blood flow. Invest Ophthalmol Vis Sci 1983;24:47-51.

32. Frayser R, Hickam JB. Retinal vascular response to breathing increased carbon dioxide and oxygen concentrations. Invest Ophthalmol Vis Sci 1964;3:427-431.

33. Geiser MH, Riva CE, GDorner GT, Diermann U, Luksch A, Schmetterer L. Response of choroidal blood flow in the foveal region to hyperoxia and hyperoxia-hypercapnia. Current Eye Res 2000;21:669-676.

34. Riva CE, Cranstoun SD, Grunwald JE, Petrig BL. Choroidal blood flow in the foveal region of the human ocular fundus. Invest Ophthalmol Vis Sci 1994;35:4273-4281.

35. Ahmed J, Pulfer M, Linsenmeier RA. Measurement of blood flow through the retinal circulation of the cat during normoxia and hypoxemia using fluorescent microspheres. Microvasc Res 2001;62:143-153.

36. Alm A, Bill A. The oxygen supply to the retina: II. Effects of high intraocular pressure and of increased arterial carbon dioxide tension on uveal and retinal blood flow in cats. Acta Physiol Scand 1972;84:306-319.

37. Wang L, Grant C, Fortune B, Cioffi GA. Retinal and choroidal vasoreactivity to altered PaCO2 in rat measured with a modified microsphere technique. Exp Eye Res 2008;86:908-913.

38. Riva CE, Grunwald JE, Petrig BL. Autoregulation of human retinal blood flow: an investigation with laser Doppler velocimetry. Invest Ophthalmol Vis Sci 1986;27:1706-1712.

39. Riva CE, Sinclair SH, Grunwald JE. Autoregulation of retinal circulation in response to decrease of perfusion pressure. Invest Ophthalmol Vis Sci 1981;21:34-38.

40. Alm A, Bill A. Ocular and optic nerve blood flow at normal and increased intraocular pressures in monkeys (macaca irus): a study with radioactively labeled microspheres including flow determinations in brain and some other tissues. Exp Eye Res 1973;15:15-29.

41. Kiel JW, van Heuven WAJ. Ocular perfusion pressure and choroidal blood flow in the rabbit. Invest Ophthalmol Vis Sci 1995;36:579-585.

42. Kiel JW. Choroidal myogenic autoregulation and intraocular pressure. Exp Eye Res 1994;58:529-544.

43. Steinle JJ, Krizsan-Agbas D, Smith PG. Regional regulation of choroidal blood flow by autonomic innervation in the rat. Am J Physiol Regul Integr Comp Physiol 2000;279:202-209.

44. Alm A. The effect of sympathetic stimulation on blood flow through the uvea, retina and optic nerve in monkeys. Exp Eye Res 1977;25:19-24.

45. Nilsson SFE, Linder J, Bill A. Characteristics of uveal vasodilation produced by facial nerve stimulation in monkeys, cats and rabbits. Exp Eye Res 1985;40:841-852.

46. Haacke EM, Brown RW, Thompson MR, Venkatesan R. Magnetic Resonance Imaging: Physical Principles and Sequence Design. New York: John Wiley & Sons; 1999.

47. Ogawa S, Lee T-M, Kay AR, Tank DW. Brain magnetic resonance imaging with contrast dependent on blood oxygenation. Proc Natl Acad Sci USA 1990;87:9868-9872.

48. Ugurbil K, Hu X, Chen W, Zhu XH, Kim S-G, Georgopoulos A. Functional mapping in the human brain using high magnetic fields. Phil Trans R Soc Lond B 1999;354:1195-1213.

49. Fox PT, Raichle ME. Focal physiological uncoupling of cerebral blood flow and oxidative metabolism during somatosensory stimulation in human subjects. Proc Natl Acad Sci USA 1986;83:1140-1144.

50. Posse S, Elghahwagi B, Wiese S, Kiselev VG. Effect of graded hypo- and hypercapnia on fMRI contrast in visual cortex: quantification of T2* changes by multiecho EPI. Magn Reson Med 2001;46:264-271.

51. Cohen ER, Ugurbil K, Kim S-G. Effect of basal conditions on the magnitude and dynamics of the blood oxygenation level-dependent fMRI response. J Cereb Blood Flow Metab 2002;22:1042-1053.

52. Sicard KM, Duong TQ. Effects of Hypoxia, Hyperoxia and Hypercapnia on Baseline and Stimulus-Evoked BOLD, CBF and CMRO2 in Spontaneously Breathing Animals. NeuroImage 2005;25:850-858.

53. Duong TQ, Iadecola C, Kim SG. Effect of hyperoxia, hypercapnia and hypoxia on cerebral interstitial oxygen tension and cerebral blood flow in the rat brain: an 19F/1H study. Magn Reson Med 2001;45:61-70.

54. Dobre M, Marjanska M, Ugurbil K. Blood T1 measurements at high magnetic field strengths. Proceedings of the 13th Annual Meeting of ISMRM. Miami Beach, FL, USA; 2005.

55. Barbier EL, Lamalle L, Decorps M. Methodology of brain perfusion imaging. J Magn Reson Imaging 2001;13:496-520.

56. Wolf RL, Detre JA. Clinical neuroimaging using arterial spin-labeled perfusion MRI. Neurotherapeutics 2007;4:346-359.

57. Liu TT, Brown GG. Measurement of cerebral perfusion with arterial spin labeling: Part 1. Methods. J Int Neuropsycholog Soc 2007;13:517-525.

58. Williams DS, Detre JA, Leigh JS, Koretsky AP. Magnetic resonance imaging of perfusion using spin inversion of arterial water. Proc Natl Acad Sci USA 1992;89:212-216.

59. Wong EC, Buxton RB, Frank LR. Quantitative imaging of perfusion using a single subtraction (QUIPSS and QUIPSSII). Magn Reson Med 1998;39:702-708.

60. Kim S-G. Quantification of relative cerebral blood flow change by flow-sensitive alternating inversion recovery (FAIR) technique: application to functional mapping. Magn Reson Med 1995;34:293-301.

61. Detre JA, Wang JJ, Wang Z, Rao H. Arterial spin-labeled perfusion MRI in basic and clinical neuroscience. Cur Opinion Neuro 2009;22:348-355.

62. Steger TR, White RA, Jackson EF. Input parameter sensitivity analysis and comparison of quantification model for continuous arterial spin labeling. Magn Reson Med 2005;53:895-903.

63. Shen Q, Ren H, Cheng H, Fisher M, Duong TQ. Functional, perfusion and diffusion MRI of acute focal ischemic brain injury. J Cereb Blood Flow and Metab 2005;25:1265-1279.

64. Herscovitch P, Raichle ME. What is the correct value for the brain-blood partition coefficient for water? J Cereb Blood Flow Metab 1985;5:65-69.

65. Reinoso RF, Telfer BA, Rowland M. Tissue water content in rats measured by desiccation. J Pharmacol Toxicol Methods 1997;38:87-92.

66. Stefansson E, Wilson CA, Lightman SL, Kuwabara T, Palestine AG, Wagner HG. Quantitative measurements of retinal edema by specific gravity determinations. Invest Ophthalmol Vis Sci 1987;28:1281-1289.

67. Guilfoyle DN, Dyakin VV, O'Shea J, Pell GS, Helpern JA. Quantitative measurements of proton spin-lattice (T1) and spin-spin (T2) relaxation times in the mouse brain at 7.0 T. Magn Reson Med 2003;49(3):576-580.

68. Nair G, Shen Q, Duong TQ. Relaxation time constants and apparent diffusion coefficients of rat retina at 7 Tesla. Int J Imaging Syst Technol 2010;20:126-130.

69. Talagala SL, Ye FQ, Ledden PJ, Chesnick S. Whole-brain 3D perfusion MRI at 3.0 T using CASL with a separate labeling coil. Magn Reson Med 2004;52:131-140.

70. Zhang X, Nagaoka T, Auerbach E, Champion R, Zhou L, Hu X, Duong TQ. Quantitative basal CBF and CBF fMRI of rhesus monkeys using three-coil continuous arterial spin labeling NeuroImage 2007;34:1074-1083.

71. Alsop D, Detre J. Reduced transit-time sensitivity in noninvasive magnetic resonance imaging of human cerebral blood flow. J Cereb Blood Flow Metab 1996;16:1236-1249.

72. Wang J, Alsop DC, Li L, Listerud J, Gonzalez-At JB, Schanll MD, Detre JA. Comparison of quantitative perfusion imaging using arterial spin labeling at 1.5 and 4.0 Tesla. Magn Res Med 2002;48:242-254.

73. Parkes LM, Tofts PS. Improved accuracy of human cerebral blood perfusion measurements using arterial spin labeling: Accounting for capillary water permeability. Magn Reson Med 2002;48:27-41.

74. St. Lawrence KS, Frank JA, McLaughlin AC. Effect of restricted water exchange on cerebral blood flow values calculated with arterial spin tagging: a theoretical investigation. Magn Reson Med 2000;44:440-449.

75. Silva AC, Zhang W, Williams DS, Koretsky AP. Estimation of water extraction fractions in rat brain using magnetic resonance measurement of perfusion with arterial spin labeling. Magn Reson Med 1997;37:58-68.

76. Silva A, Williams D, Koretsky A. Evidence for the exchange of arterial spin-labeled water with tissue water in rat brain from diffusion-sensitized measurements of perfusion. Magn Reson Med 1997;38:232-237.

77. Duong TQ, Kim DS, Ugurbil K, Kim SG. Localized cerebral blood flow response at submillimeter columnar resolution. Proc Natl Acad Sci USA 2001;98:10904-10909.

78. Fujimoto JG, Pitris C, Boppart SA, Brezinski ME. Optical coherence tomography: an emerging technology for biomedical imaging and optical biopsy. Neoplasia 2000;2:9-25.

79. Wojtkowski M, Srinivasan V, Fujimoto JG, Ko T, Schuman JS, Kowalczyk A, Duker JS. Three-dimensional retinal imaging with high-speed ultrahigh-resolution optical coherence tomography. Opth 2005;112:1734-1746.

80. Szkulmowska A, Szkulmowski M, Szlag D, Kowalczyk A, Wojtkowski M. Three-dimensional quantitative imaging of retinal and choroidal blood flow velocity using joint spectral and time domain optical coherence tomography. Optics Express 2009;17:10584-10598.

81. An L, Wang RK. In vivo volumetric imaging of vascular perfusion within human retina and choroids with optical micro-angiography. Opt Exp 2008;16:11438-11452.

82. Harris A, Kagemann L, Cioffi GA. Assessment of human ocular hemodynamics. Surv of Ophthalmol 1998;42:509-533.

83. Preussner PR, Richard G, Darrelmann O, Weber J, Kreissig I. Quantitative measurement of retinal blood flow in human beings by application of digital image-processing methods to television fluorescein angiograms. Graefes Arch Clin Exp Ophthalmol 1983;221:110-112.

84. Bishoff PM, Flower RW. Ten years experience with choroidal angiography using indocyanine green dye: a new routine examination or an epilogue. Doc Ophthalmol 1985;60:235-291.

85. Riva CE, Grunwald JE, Sinclair SH, O'Keefe K. Fundus camera based retinal LDV. Applied Optics 1981;20:117-120.

86. Riva CE, Grunwald JE, Sinclair SH, Petrig BL. Blood velocity and volumetric flow rate in human retinal vessels. Invest Ophthalmol Vis Sci 1985;26:1124-1132.

87. Rajan V, Varghese B, van Leeuwen TG, Steenbergen W. Review of methodological developments in laser Doppler flowmetry. Lasers Med Sci 2009;24:269-283.

88. Boas DA, Dunn AK. Laser speckle contrast imaging in biomedical optics. J Biomed Optics 2010;15:011109.

89. Cheng H, Yan Y, Duong TQ. Temporal statistical analysis of laser speckle image and its application to retinal blood-flow imaging. Optics Express 2008;16:10214-10219.

90. Wang L, Fortune B, Cull G, McElwain KM, Cioffi GA. Microspheres method for ocular blood flow measurement in rats: Size and dose optimization. Exp Eye Res 2007;84:108-117.

91. Yu DY, Alder VA, Cringle SJ, Brown MJ. Choroidal blood flow measured in the dog eye in vivo and in vitro by local hydrogen clearance polarography-validation of a technique and response to raised intraocular pressure. Exp Eye Res 1988;46:289-303.

92. Stefansson E, Wagner HG, Seida M. Retinal blood flow and its autoregulation measured by intraocular hydrogen clearance. Exp Eye Res 1988;47:669-678.

93. Linsenmeier RA. Effects of light and darkness on oxygen distribution and consumption in the cat retina. J Gen Physiol 1986;88:521-542.

94. Yu D-I, Cringle SJ, Alder V, Su E-N. Intraretinal oxygen distribution in the rat with graded syetemic hyperoxia and hypercapnia. Invest Ophthalmol Vis Sci 1999;40:2082-2087.

95. Yu DY, Alder VA, Cringle SJ. Measurement of blood flow in rat eyes by hydrogen clearance. Am J Physiol 1991;261:H960-H968.

96. Shen Q, Cheng H, Chang TF, Nair G, Shonat RD, Pardue MT, Toi VV, Duong TQ. Magnetic resonance imaging of anatomical and vascular layers of the cat retina. J Magn Reson Imaging 2006;23:465-472.

97. Nair G, Cheng H, Kim M, Nagaoka T, Olson DE, Thule PM, Pardue MT, Duong TQ. Manganese-Enhanced MRI Reveals Multiple Cellular and Vascular Layers in Normal and Degenerated Retinas. 2007.

98. Duong TQ, Ngan S-C, Ugurbil K, Kim S-G. Functional magnetic resonance imaging of the retina. Invest Ophthalmol Vis Sci 2002;43:1176-1181.

99. De La Garza BH, Muir ER, Li G, Shih YY, Duong TQ. Blood oxygenation level-dependent (BOLD) functional MRI of visual stimulation in the rat retina at 11.7 T. NMR Biomed 2010;in press.

100. Li Y, Cheng H, Duong TQ. Blood-flow magnetic resonance imaging of the retina. Neuroimage 2008;39:1744-1751.

101. Alsop DC, Maldjian JA, Detre JA. In vivo MR perfusion imaging of the human retina. Proc Int Soc Magn Reson Med. Volume 1. Denver, Colorado, USA; 2000. p 162.

102. Lu K, Wu WC, Wong EC, Liu TT. Functional perfusion imaging of human retina with arterial spin labeling MRI. Proc Int Soc Magn Reson Med. Miami, FL, USA; 2005.

103. Williams DS, Detre JA, Leigh JS, Koresky AP. Magnetic resonance imaging of perfusion using spin inversion of arterial water. Proc Natl Acad Sci USA 1992;89:212-216.

104. Zappe AC, Reichold J, Burger C, Weber B, Buck A, Pfeuffer J, Logothetis NK. Quantification of cerebral blood flow in nonhuman primates using arterial spin labeling and a two-compartment model. Magn Reson Imaging 2007;25(6):775-783.

105. Niwa K, Younkin L, Ebeling C, Turner SK, Westaway D, Younkin S, Ashe KH, Carlson GA, Iadecola C. Abeta 1-40-related reduction in functional hyperemia in mouse neocortex during somatosensory activation. Proc Natl Acad Sci USA 2000;97:9735-9740.

106. Schocket LS, Brucker AJ, Niknam RM, Grunwald JE, DuPont J, Brucker AJ. Foveolar choroidal hemodynamics in proliferative diabetic retinopathy. Int Ophthalmol 2004;25:89-94.

107. van Dorsten FA, Hata R, Maeda K, Franke C, Eis M, Hossmann KA, Hoehn M. Diffusion- and perfusion-weighted MR imaging of transient focal cerebral ischaemia in mice. NMR Biomed 1999;12(8):525-534.

108. Foley LM, Hitchens TK, Kochanek PM, Melick JA, Jackson EK, Ho C. Murine orthostatic response during prolonged vertical studies: effect on cerebral blood flow measured by arterial spin-labeled MRI. Magn Reson Med 2005;54(4):798-806.

109. Hoyte LC, Papadakis M, Barber PA, Buchan AM. Improved regional cerebral blood flow is important for the protection seen in a mouse model of late phase ischemic preconditioning. Brain Research 2006;1121:231-237.

110. Zhang L, Schallert T, Zhang ZG, Jiang Q, Arniego P, Li Q, Lu M, Chopp M. A test for detecting long-term sensorimotor dysfunction in the mouse after focal cerebral ischemia. J Neurosci Methods 2002;117:207-214.

111. Sun Y, Schmidt NO, Schmidt K, Doshi S, Rubin JB, Mulkern RV, Carroll R, Ziu M, Erkmen K, Poussaint TY, Black P, Albert M, Burstein D, Kieran MW. Perfusion MRI of U87 brain tumors in a mouse model. Magn Reson Med 2004;51:893-899.

112. Koistinaho M, Kettunen MI, Goldsteins G, Keinanen R, Salminen A, Ort M, Bures J, Liu D, Kauppinen RA, Higgins LS, Koistinaho J. Beta-amyloid precursor protein transgenic mice that harbor diffuse A beta deposits but do not form plaques show increased ischemic vulnerability: role of inflammation. Proc Natl Acad Sci USA 2002;99(3):1610-1615.

113. Hooijmans CR, Rutters F, Dederen PJ, Gambarota G, Veltien A, van Groen T, Broersen LM, Lutjohann D, Heerschap A, Tanila H, Kiliaan AJ. Changes in cerebral blood volume and amyloid pathology in aged Alzheimer APP/PS1 mice on a docosahexaenoic acid (DHA) diet or cholesterol enriched Typical Western Diet (TWD). Neurobiol Disease 2007;28:16-29.

114. Muir ER, Shen Q, Duong TQ. Cerebral blood flow MRI in mice using the cardiac spin-labeling technique. Magn Reson Med 2008;60:744-748.

115. Wang J, Zhang Y, Wolf RL, Roc AC, Alsop DC, Detre JA. Amplitude-modulated continuous arterial spin-labeling 3.0-T perfusion MR imaging with a single coil: feasibility study. Radiology 2005;235:218-228.

116. Ye FQ, Frank JA, Weinberger DR, McLaughlin AC. Noise reduction in 3D perfusion imaging by attenuating the static signal in arterial spin tagging (ASSIST). Magn Reson Med 2000;44:1236-1249.

117. Shen Q, Meng X, Fisher M, Sotak CH, Duong TQ. Pixel-by-pixel spatiotemporal progression of focal ischemia derived using quantitative perfusion and diffusion imaging. J Cereb Blood Flow and Metab 2003;23:1479-1488.

118. Silva AC, Kim SG, Garwood M. Imaging blood flow in brain tumors using arterial spin labeling. Magn Reson Med 2000;44(2):169-173.

119. Golay X, Stuber M, Pruessmann KP, Meier D, Boesiger P. Transfer insensitive labeling technique (TILT): application to multislice functional perfusion imaging. J Magn Reson Imag 1999;9:454-461.

120. McLaughlin AC, Ye FQ, Pekar JJ, Santha AKS, Frank JA. Effect of magnetization transfer on the measurement of cerebral blood flow values measured by using arterial spin tagging approaches: a theorectical investigation. Magn Reson Med 1997;37:501-510.

121. Zhou J, van Zijl PC. Effect of transit times on quantification of cerebral blood flow by the FAIR T1-difference approach. Magn Reson Med 1999;42:890-894.

122. Yang Y, Engelien W, Xu S, Gu H, Silbersweig DA, Stern E. Transit time, trailing time, and cerebral blood flow during brain activation: measurement using multislice, pulsed spin-labeling perfusion imaging. Magn Reson Med 2000;44:680-685.

123. Zhou J, Wilson DA, Ulatowski JA, Traystman RJ, van Zijl PC. Two-compartment exchange model for perfusion quantification using arterial spin tagging. J Cereb Blood Flow Metab 2001;21(4):440-455.

124. Zhang W, Williams DS, Detre JA, Koretsky AP. Measurement of brain perfusion by volume-localized NMR spectroscopy using inversion of arterial water spins: Accounting for transit time and cross-relaxation. Magn Reson Med 1992;25:362-371.

125. Liu ZM, Schmidt KF, Sicard KM, Duong TQ. Imaging oxygen consumption in forepaw somatosensory stimulation in rats under isoflurane anesthesia. Magn Reson Med 2004;52:277-285.

126. Maeda K, Gunter M, Olah L, Konstantin-Alexander H. Quantitative measurement of local cerebral blood flow in the anesthetized mouse using intraperitoneal [14C]iodoantipyrine injection and final arterial heart blood sampling. J Cereb Blood Flow and Metab 2000;20:10-14.

127. de Vasconcelos AP, Bouilleret V, Riban V, Wasterlain C, Nehlig A. Role of nitric oxide in cerebral blood flow changes during kainate seizures in mice: genetic and pharmacological approaches. Neurobiology of Disease 2005;18(2):270-281.

128. Sicard K, Shen Q, Brevard ME, Sullivan R, Ferris CF, King JA, Duong TQ. Regional cerebral blood flow and BOLD responses in conscious and anesthetized rats under basal and hypercapnic conditions: implications for functional MRI studies. J Cereb Blood Flow Metab 2003;23(4):472-481.

129. Duong TQ, Silva AC, Lee S-P, Kim S-G. Comparison of Spatial Localization between Synaptic Activity and Hemodynamic Responses following Somatosensory Stimulation: an MRI study at 9.4 Tesla. 1999; Philadelphia, PA.

130. Duong TQ, Silva AC, Lee SP, Kim SG. Functional MRI of calcium-dependent synaptic activity: cross correlation with CBF and BOLD measurements. Magn Reson Med 2000;43(3):383-392.

131. Reinstrup P, Ryding E, Algotsson L, Messeter K, Asgeirsson B, Uski T. Distribution of cerebral blood flow during anesthesia with isoflurane or halothane in humans. Anesthesiology 1995;82(2):359-366.

132. Drummond JC, Scheller MS, Todd MM. The effect of nitrous oxide on cortical cerebral blood flow during anesthesia with halothane and isoflurane, with and without morphine, in the rabbit. Anesth Analg 1987;66(11):1083-1089.

133. Zheng B, Lee PTH, Golay X. High-sensitivity cerebral perfusion mapping in mice by kbGRASE_FAIR at 9.4 T. NMR Biomed 2010.

134. Ayata C, Dunn AK, Gursoy-Ozdemir Y, Huan Z, Boas DA, Moskowitz MA. Laser Speckle Flowmetry for the Study of Cerebrovascular Physiology in Normal and Ischemic Mouse Cortex. J Cereb Blood Flow Metab 2004;24:744-755.

135. Niwa K, Carlson GA, Iadecola C. Exogenous A beta1-40 reproduces cerebrovascular alterations resulting from amyloid precursor protein overexpression in mice. J Cereb Blood Flow and Metab 2000;20:1659-1668.

136. Matta BF, Heath KJ, Tipping K, Summors AC. Direct cerebral vasodilatory effects of sevoflurane and isoflurane. Anesthesiology 1999;91:677-680.

137. Sinclair MD. A review of the physiological effects of alpha2-agonists related to the clinical use of medetomidine in small animal practice. Can Vet J 2003;44:885-897.

138. Lei H, Grinberg O, Nwaigwe CI, Hou HG, Williams H, Swartz HM, Dunn JF. The effects of ketamine-xylazine anesthesia on cerebral blood flow and oxygenation observed using nuclear magnetic resonance perfusion imaging and electron paramagnetic resonance oximetry. Brain Research 2001;913:174-179.

139. Muir ER, Duong TQ. MRI of retinal and choroidal blood flow with laminar resolution. NMR Biomed 2010;in press.

140. Duong TQ, Muir ER. Magnetic Resonance Imaging of the Retina. Jpn J Ophthalmol 2009;53:352-367.

141. Schmucker C, Schaeffel F. A paraxial schematic eye model for growing C57BL/6 mouse. Vision Research 2004;44:1857-1867.

142. Gabhann FM, Demetriades AM, Deering T, Packer JD, Shah SM, Duh E, Campochiaro PA, Popel AS. Protein transport to choroid and retina following periocular injection: theoretical and experimental study. Annals Biomed Engr 2007;35:615-630.

143. Spaide RF, Koizumi H, Pozonni MC. Enhanced depth imaging spectral-domain optical coherence tomography. Am J Ophthalmol 2008;146:496-500.

144. Ramrattan RS, van der Schaft TL, Mooy CM, de Bruijn WC, Mulder PGH, de Jong PTVM. Morphometric analysis of Bruch's membrane, the choriocapillaries, and the choroid in aging. Invest Ophthalmol Vis Sci 1994;35:2857-2864.

145. Tilton RG, Chang KC, LeJeune WS, Stephan CC, Brock TA, Williamson JR. Role for nitric oxide in the hyperpermeability and hemodynamic changes induced by intravenous VEGF. Invest Ophthalmol Vis Sci 1999;40(3):689-696.

146. Keough EM, Wilcox LM, Connolly RJ, Hotte CE. The effect of complete tenotomy on blood flow to the anterior segment of the canine eye. Invest Ophthalmol Vis Sci 1980;19(11):1355-1359.

147. Small KW, Stefansson E, Hatchell DL. Retinal blood flow in normal and diabetic dogs. Invest Ophthalmol Vis Sci 1987;28(4):672-675.

148. Friedman E, Kopald HH, Smith TR. Retinal and choroidal blood flow determined with krypton 85 in anesthetized animals. Invest Ophthalmol 1964;3:539-547.

149. Bill A. Circulation in the eye. In: Renkin EM, Michel CC, editors. Handbook of Physiology: Cardiovascular. Bethesda, MD: American Physiological Society; 1984.

150. Johnson GL. Contributions to the comparative anatomy of vertebrates, chiefly based on ophthalmoscopic examination. Phil Trans R Soc Lond B 1901;194:1-82.

151. Li Y, Cheng H, Duong TQ. Blood-flow magnetic resonance imaging of the retina. Neuroimage 2008;39:1744-1751.

152. Chiou GCY, Chen YJ. Effects of D- and L-isomers of timolol on retinal and choroidal blood flow in ocular hypertensive rabbit eyes. J Ocular Pharm 1992;8:183-190.

153. Laties AM, Jacobowitz DA. A comparative study of the autonomic innervation of the eye in monkey, cat and rabbit. Anat Rec 1966;156:383-396.

154. Duong TQ. Cerebral blood flow and BOLD fMRI responses to hypoxia in awake and anesthetized rats. Brain Research 2007;1135:186-194.

155. Campen MJ, Tagaito Y, Jenkins TP, Balbir A, O'Donnell CP. Heart rate variability response to hypoxic and hypercapnic exposures in different mouse strains. J Appl Physiol 2005;99:807-813.

156. Kline DD, Yang T, Huang PL, Prabhakar NR. Altered respiratory responses to hypoxia in mutant mice deficient in neuronal nitric oxide synthase. J Physiol 1998;511:273-287.

157. Yu DY, Cringle SJ. Retinal degeneration and local oxygen metabolism. Exp Eye Res 2005;80:745-751.

158. Nair G, Tanaka Y, T. N, Pardue MT, Olson D, Thule PM, Duong TQ. Layer-specific blood-volume MRI of the retina. 2008.

159. Riva CE, FPournaras CJ, Tsacopoulos M. Regulation of local oxygen tension and blood flow in the inner retina during hyperoxia. J Appl Physiol 1986;61:592-598.

160. Ogawa S, Menon RS, Tank DW, Kim S-G, Merkle H, Ellermann JM, Ugurbil K. Functional brain mapping by blood oxygenation level-dependent contrast magnetic resonance imaging. Biophys J 1993;64:800-812.

161. Zhong K, Leupold J, Hennig J, Speck O. Systematic investigation of balanced steady-state free precession for functional MRI in the human visual cortex at 3 Tesla. Magn Reson Med 2007;57:67-73.

162. Miller KL, Smith SM, Jezzard P, Wiggins GC, Wiggins CJ. Signal and noise characteristics of SSFP FMRI: a comparison with GRE at multiple field strengths. NeuroImage 2007;37:1227-1236.

163. Scheffler K, Seifritz E, Bilecen D, Venkatesan R, Hennig J, Deimling M, Haacke EM. Detection of BOLD changes by means of a frequency-sensitive trueFISP technique: preliminary results. NMR Biomed 2001;14:490-496.

164. Miller KL, Hargreaves BA, Lee JH, Ress D, deCharms RC, Pauly JM. Functional brain imaging using a blood oxygenation sensitive steady state. Magn Reson Med 2003;50:675-683.

165. Bowen C, Menon R, Gati J. High field balanced-SSFP FMRI: a BOLD technique with excellent tissue sensitivity and superior large vessel suppression. Proc Int Soc Magn Reson Med. Miami, Florida, USA; 2005.

166. Lee JH, Dumoulin SO, Saritas EU, Glover GH, Wandell BA, Nishimura DG, Pauly JM. Full-brain coverage and high-resolution imaging capabilities of passband b-SSFP fMRI at 3T. Magn Reson Med 2008;59:1099-1110.

167. Miller KL, Jezzard P. Modeling SSFP functional MRI contrast in the brain. Magn Reson Med 2008;60:661-673.

168. Buxton RB, Uludag K, Dubowitz DJ, Liu TT. Modeling the hemodynamic response to brain activation. NeuroImage 2004;23:S220-S233.

169. Bill A, Sperber GO. Aspects of oxygen and glucose consumption in the retina: effects of high intraocular pressure and light. Exp Ophthalmol 1990;228:124-127.

170. Congdon NG, Friedman DS, Lietman T. Important causes of visual impairment in the world today. JAMA 2003;290:2057-2060.

171. Fong DS, Aiello LP, Ferris FL, Klein R. Diabetic retinopathy. Diabetes Care 2004;27:2540-2553.

172. Kempen JH, O'Colmain BJ, Leske MC, Haffner SM, Klein R, Moss SE, Taylor HR, Hamman RF, West SK, Wang JJ, Congdon NG, Friedman DS. The prevalence of diabetic retinopathy among adults in the United States. Arch Ophthalmol 2004;122:552-563.

173. Roy MS, Klein R, O'Colmain BJ, Klein BE, Moss SE, Kempen JH. The prevalance of diabetic retinopathy among adult type 1 diabetic persons in the United States. Arch Ophthalmol 2004;122:546-551.

174. Alder VA, Su E-N, Yu D-Y, Cringle SJ, Yu PK. Diabetic retinopathy: Early functional changes. Clin Exp Pharmacol Physiol 1997;24:785-788.

175. Group DCaCTR. Early worsening of diabetic retinopathy in the diabetes control and complications trial. Arch Ophthalmol 1998;116:874-886.

176. Frank RN. On the pathogenesis of diabetic retinopathy: A 1990 update. Ophthalmology 1991;98:586-593.

177. Lorenzi M, Feke GT, Cagliero E, Pitler L, Schaumberg DA, Berisha F, Nathan DM, McMeel JW. Retinal haemodynamics in individuals with well-controlled type 1 diabetes. Diabetologia 2008;51:361-364.

178. Grunwald JE, DuPont J, Riva CE. Retinal haemodynamics in patients with early diabetes mellitus. Br J Ophthalmol 1996;80:327-331.

179. Patel V, Rassam S, Newsom R, Wiek J, Kohner E. Retinal blood flow in diabetic retinopathy. BMJ 1992;305:678-683.

180. Cheung N, Mitchell P, Wong TY. Diabetic retinopathy. Lancet 2010;376:124-136.

181. Kollias AN, Ulbig MW. Diabetic retinopathy. Dtsch Arztebl Int 2010;107:75-84.

182. Antonetti DA, Barber AJ, Bronson SK, Freeman WM, Gardner TW, Jefferson LS, Kester M, Kimball SR, Krady JK, LaNoue KF, Norbury CC, Quinn PG, Sandirasegarane L, Simpson IA. Diabetic retinopathy: Seeing beyond glucose-induced microvascular disease. Diabetes 2006;55:2401-2411.

183. Reiter CE, Gardner TW. Functions of insulin and insulin receptor signaling in retina: possible implications for diabetic retinopathy. Prog Retina Eye Res 2003;22:545-562.

184. Feit-Leichman RA, Kinouchi R, Takeda M, Fan Z, Mohr S, Kern TS, Chen DF. Vascular damage in a mouse model of diabetic retinopathy: relation to neuronal and glial changes. Invest Ophthalmol Vis Sci 2005;46:4281-4287.

185. Rossini AA, Appel MC, Williams RM, Like AA. Genetic influence of the streptozotocin-induced insulitis and hyperglycemia. Diabetes 1977;26:916-920.

186. Wang J, Takeuchi T, Tanaka S, Kubo SK, Kayo T, Lu D, Takata K, Koizumi A, Izumi T. A mutation in the insulin 2 gene induces diabetes with severe pancreatic beta-cell dysfunction in the Mody mouse. J Clin Invest 1999;103:27-37.

187. Lee S, Harris NR. Losartan and ozagrel reverse retinal arteriolar constriction in non-obese diabetic mice. Microcircul 2008;15:379-387.

188. Tadayoni R, Paques M, Gaudric A, Vicaut E. Erythrocyte and leukocyte dynamics in the retinal capillaries of diabetic mice. Exp Eye Res 2003;77:497-504.

189. Wallis RH, Wang K, Marandi L, Hsieh E, Ning T, Chao GYC, Sarmiento J, Paterson AD, Poussier P. Type 1 diabetes in the BB rat: a polygenic disease. Diabetes 2009;58:1007-1017.

190. Finegood DT, McArthur MD, Kojwang D, Thomas MJ, Topp BG, Leonard T, Buckingham RE. Beta-cell mass dynamics in Zucker diabetic fatty rats. Diabetes 2001;50:1021-1029.

191. Lieth E, Gardner TW, Barber AJ, Antonetti DA. Retinal neurodegeneration: early pathology in diabetes. Clin Exp Ophthalmol 2000;28:3-8.

192. Della Sala S, Bertoni G, Somazzi L, Stubbe F, Wilkins AJ. Impaired contrast sensitivity in diabetic patients with and without retinopathy: a new technique for rapid assessment. Br J Ophthalmol 1985;69:136-142.

193. Tregear SJ, Knowles PJ, Ripley LG, Casswell AG. Chromatic-contrast threshold impairment in diabetes. Eye 1997;11:537-546.

194. Luu CD, Szental JA, Lee SY, Lavanya R, Wong TY. Correlation between retinal oscillatory potentials and retinal vascular caliber in type 2 diabetes. Invest Ophthalmol Vis Sci 2010;51:482-486.

195. Tzekov R, Arden GB. The electroretinogram in diabetic retinopathy. Surv Ophthalmol 1999;44:53-60.

196. Sakai H, Tani Y, Shirasawa E, Shirao Y, Kawasaki K. Development of electroretinographic alteration in streptozotocin-induced diabetes in rats. Ophthalmic Res 1995;27:57-63.

197. Kohzaki K, Vingrys AJ, Bui BV. Early inner retinal dysfunction in streptozotocin-induced diabetic rats. Invest Ophthalmol Vis Sci 2008;49:3595-3604.

198. Shirao Y, Kawasaki K. Electrical responses from diabetic retina. Prog Retinal Eye Res 1999;17:59-67.

199. Prusky GT, Alam NM, Beekman S, Douglas RM. Rapid quantification of adult and developing mouse spatial vision using a virtual optomotor system. Invest Ophthalmol Vis Sci 2004;45:4611-4616.

200. Douglas RM, Alam NM, Silver BD, McGill TJ, Tschetter WW, Prusky GT. Independent visual threshold measurements in the two eyes of freely moving rats and mice using a virtual-reality optokinetic system. Visual Neurosci 2005;22:677-684.

201. Umino Y, Everhart D, Solessio E, Cusato K, Pan JC, Nguyen TH, Brown ET, Hafler R, Frio BA, Knox BE, Engbretson GA, Haeri M, Cui L, Glenn AS, Charron MJ, Barlow RB. Hypoglycemia leads to age-related loss of vision. Proc Natl Acad Sci 2006;103:19541-19545.

202. Wright WS, Harris NR. Ozagrel attenuates early strptozotocin-induced constriction of arterioles in the mouse retina. Exp Eye Res 2008;86:528-536.

203. Lee S, Morgan GA, Harris NR. Ozagrel reverses streptozotocin-induced constriction of arterioles in rat retina. Microvasc Res 2008;76:217-223.

204. Braun RD, Wienczewski CA, Abbas A. Erythrocyte flow in choriocapillaris of normal and diabetic rats. Microvasc Res 2009;77:247-255.

205. Tilton RG, Chang K, Pugliese G, Eades DM, Province MA, Sherman WR, Kilo C, Williamson JR. Prevention of hemodynamic and vascular albumin filtration changes in diabetic rats by aldose reductase inhibitors. Diabetes 1989;38:1258-1270.

206. Cringle SJ, Yu DY, Adler VA, Su EN. Retinal blood flow by hydrogen clearance polarography in the streptozotocin-induced diabetic rat. Invest Ophthalmol Vis Sci 1993;34:1716-1721.

207. Barber AJ, Antonetti DA, Kern TS, Reiter CEN, Soans RS, Krady JK, Levison SW, Garner TW, Bronson SK. The Ins2akita mouse as a model of early retinal complications in diabetes. Invest Ophthalmol Vis Sci 2005;46:2210-2218.

208. Gastinger MJ, Kunselman AR, Conboy EE, Bronson SK, Barber AJ. Dendrite remodeling and other abnormalities in the retinal ganglion cells of Ins2Akita diabetic mice. Invest Ophthalmol Vis Sci 2008;49:2635-2642.

209. Chen Y, Hu Y, Zhou T, Zhou KK, Mott R, Wu M, Boulton M, Lyons TJ, Gao G, Ma J. Activation of the Wnt pathway plays a pathogenic role in diabetic retinopathy in humans and animal models. Am J Pathol 2009;175:2676-2685.

210. Izumi T, Yokota-Hashimoto H, Zhao S, Wang J, Halban PA, Takeuchi T. Dominant negative pathogenesis by mutant proinsulin in the Akita diabetic mouse. Diabetes 2003;52:409-416.

211. Aylward GW. The scotopic threshold response in diabetic retinopathy. Eye 1989;3:626-637.

212. Brian JE, Bogan L, Kennedy RH, Seifen E. The impact of streptozotocin-induced diabetes on the minimum alveolar anesthetic concentratio (MAC) of inhaled anesthetics in the rat. Anesth Analg 1993;77:342-345.

213. Kita T, Kagawa K, Mammoto T, Takada K, Hayashi Y, Mashimo T, Kishi Y. Diabetes attenuates the minimum anaesthetic concentration (MAC) and MAC-blocking adrenergic response reducing actions of clonidine in rats. Acta Anaesth Scand 2001;45:1230-1234.

214. Burgos LG, Ebert TJ, Asiddao C, Turner LA, Pattison CZ, Wang-Cheng R, Kampine JP. Increased intraoperative cardiovascular morbidity in diabetics with autonomic neuropathy. Anesth 1989;70:591-597.

215. Berson EL. Retinitis pigmentosa. The Friedenwald lecture. Invest Ophthalmol Vis Sci 1993;34:1659-1676.

216. Bessant DAR, Kaushal S, Bhattacharya SS. Genetics and Biology of the Inherited Retinal Dystrophies. In: Alm A, Ehinger BEJ, Kaufman PL, editors. Adler's Physiology of the Eye - 10th ed. St. Louis: Mosby; 2003. p 358-377.

217. Grunwald JE, Maguire AM, DuPont J. Retinal hemodynamics in retinitis pigmentosa. Am J Ophthalmol 1996;122:502-508.

218. Jones BW, Marc RE. Retinal remodeling during retinal degeneration. Exp Eye Res 2005;81:123-137.

219. McLaughlin ME, Sandberg MA, Berson EL, Dryja TP. Recessive mutations in the gene encoding the beta-subunit of rod phosphodiesterase in patients with retinitis pigmentosa. Nature Genetics 1993;4:130-134.

220. Pennesi ME, Nishikawa S, Matthes MT, Yasumura D, LaVail MM. The relationship of photoreceptor degeneration to retinal vascular development and loss in mutant rhodopsin transgenic and RCS rats. Exp Eye Res 2008;87:561-570.

221. Penn JS, Li S, Naash MI. Ambient hypoxia reverses retinal vascular attenuation in a transgenic mouse model of autosomal dominant retinitis pigmentosa. Invest Ophthalmol Vis Sci 2000;41:4007-4013.

222. Yu D-Y, Cringle SJ, Su E-N, Yu PK. Intraretinal oxygen levels before and after photoreceptor loss in the RCS rat. Invest Ophthalmol Vis Sci 2000;41:3999-4006.

223. Chrysostomou V, Stone J, Stowe S, Barnett NL, Valter K. The status of cones in the rhodopsin mutant P23H-3 retina: light-regulated damage and repair in parallel with rods. Invest Ophthalmol Vis Sci 2008;49:1116-1125.

224. Walsh N, Van Driel D, Lee D, Stone J. Multiple vulnerability of photoreceptors to mesopic ambient light in the P23H transgenic rat. Brain Research 2004;1016:197-203.

225. Vingolo EM, Rocco M, Grenga PL, Salvatore S, Pelaia P. Slowing the degenerative process, long lasting effect of hyperbaric oxygen therapy in retinitis pigmentosa. Graefes Arch Clin Exp Ophthalmol 2008;246:93-98.

226. Schmidt K-G, Pillunat LE, Kohler K, Flammer J. Ocular pulse amplitude is reduced in patients with advanced retinitis pigmentosa. Br J Ophthalmol 2001;85:678-682.

227. Falsini B, Anselmi GM, Marangoni D, D'Esposito F, Fadda A, Renzo AD, Campos EC, Riva CE. Subfoveal choroidal blood flow and central retinal function in retinitis pigmentosa. Invest Ophthalmol Vis Sci 2010 in press.

228. Chang B, Hawes NL, Hurd RE, Davisson MT, Nusinowitz S, Heckenlively JR. Retinal degeneration mutants in the mouse. Vision Research 2002;42:517-525.

229. Chang B, Hawes NL, Pardue MT, German AM, Hurd RE, Davisson MT, Nusinowitz S, Rengarajan K, Boyd AP, Sidney SS, Phillips MJ, Stewart RE, Chaudhury R, Nickerson JM, Heckenlively JR, Boatright JH. Two Mouse Retinal Degenerations Daused by Missense Mutations in the beta-subunit of Rod cGMP Phosphodiesterase Gene. Vision Research 2007;47:624-633.

230. Gargini C, Terzibasi E, Mazzoni F, Strettoi E. Retinal Organization in the Retinal Degeneration 10 (rd10) Mutant Mouse: A Morphological and ERG Study. J Comp Neurol 2007;500:222-238.

231. McLaughlin ME, Ehrhart TL, Berson EL, Dryja TP. Mutation spectrum of the gene encoding the beta subunit of rod phosphodiesterase among patients with autosomal recessive retinitis pigmentosa. Proc Natl Acad Sci 1995;92:3249-3253.

232. Li G, De La Garza B, Muir ER, Duong TQ. Layer-specific blood-flow MRI of retina degeneration at 11.7T. Proc Int Soc Magn Reson Med. Stockholm, Sweden; 2010.

233. Padnick-Silver L, Kang Derwent JJ, Giuliano E, Narfstrom K, Linsenmeier RA. Retinal oxygenation and oxygen metabolism in Abyssinian cats with a hereditary retinal degeneration. Invest Ophthalmol Vis Sci 2006;47:3683-3689.

234. Yu DY, Cringle S, Valter K, Walsh N, Lee D, Stone J. Photoreceptor death, trophic factor expression, retinal oxygen status, and photoreceptor function in the P23H rat. Invest Ophthalmol Vis Sci 2004;2004(45):2013-2019.

235. Martirosian P, Klose U, Mader I, Schick F. FAIR true-FISP perfusion imaging of the kidneys. Magn Reson Med 2004;51:353-361.

236. Gunther M, Oshio K, Feinberg DA. Single-shot 3D imaging techniques improve arterial spin labeling perfusion measurements. Magn Reson Med 2005;54:491-498.

237. Polak K, Dorner G, Kiss B, Polska E, Findl O, Rainer G, Eichler H-G, Schmetterer L. Evaluation of the Zeiss retinal vessel analyser. Br J Ophthalmol 2000;84:1285-1290.